

Optical Nanotweezers for Characterising Unmodified Proteins at the Single-Molecule Level

Arman Yousefi

A thesis submitted in partial fulfilment of the
requirements of Nottingham Trent University for the
degree of Doctor of Philosophy

September 2024

The copyright in this work is held by the author. You may copy up to 5% of this work for private study, or personal, non-commercial research. Any re-use of the information contained within this document should be fully referenced, quoting the author, title, university, degree level and pagination. Queries or requests for any other use, or if a more substantial copy is required, should be directed to the author.

Abstract

Proteins, essential macromolecules found in all living organisms, are responsible for various biological functions, including enzymatic activity, structural support, and regulation of cellular processes. Understanding their mechanisms such as protein folding, and protein-protein interaction is crucial for revealing cellular functions and disease pathways. Single-molecule characterisation techniques offer detailed insights into protein behaviour, such as conformational changes and dynamic interactions, which were previously difficult to study using bulk methods. However, conventional single-molecule techniques, such as single-molecule Förster resonance energy transfer (smFRET) and cryogenic electron microscopy (cryo-EM), have notable limitations. smFRET necessitates chemical modifications, which hinder the ability to monitor rapid protein dynamics in their native state. On the other hand, cryo-EM is inherently non-continuous, capturing only static snapshots of protein movements. As a result, these methods mainly lack utility for studying the single-molecule kinetic reactions of proteins.

This thesis employs optical nanotweezers using plasmonic double-nanohole (DNH) structures to trap individual, unlabelled proteins, through driving the oscillation of free-electrons, known as surface plasmons, excited by light. The light passing through the DNHs focuses the electric field into nanometre-scale regions known as hotspots, which are sensitive to refractive index changes in these areas. Since protein structural changes are linked to variations in the refractive index, this approach enables us to observe conformational changes in trapped proteins with high sensitivity. We applied this approach to study ferritin, a ubiquitous protein present in nearly all living organisms. Ferritin plays a critical role in iron storage and regulation, which is essential for maintaining iron homeostasis and supporting overall physiological function.

This thesis will describe trapping and monitoring the structural dynamics of apo-ferritin (protein without iron core) and holo-ferritin (protein with iron core) in real-time. Notably, we monitored the iron-loading process in a single apo-ferritin as it converted to a holo-ferritin *in situ*. Furthermore, the linear relationship between light transmission through the DNH and the size of the trapped particles enabled us to track the disassembly of single ferritin molecules in acidic environments. Our results indicated that the protein disassembly occurs in a stepwise manner, with subunits

disassembling cooperatively, emphasising the important role of intermediate subunits in the process.

This thesis demonstrates the benefits of, optical nanotweezers, as a label-free approach, to study individual proteins in their native environment without modification and in real time. Our results enhance the understanding of ferritin, particularly its disassembly process and the kinetics of iron release, which could aid in the design of drug delivery carriers and the development of medical treatments and pharmaceuticals. Moreover, the versatile nature of optical nanotweezers allows for the extension of this approach to investigate a wide range of other proteins, providing a valuable understanding of their structure, dynamics, and interactions, and further broadening the potential applications in biomedical research.

Declaration

I declare that the thesis has been composed by myself and that the work has not been submitted for any other degree or professional qualification. I confirm that the work submitted is my own, except where work which has formed part of jointly-authored publications has been included

Acknowledgements

I am deeply thankful to my supervisory team for their genuine support throughout my PhD journey. First and foremost, I extend my heartfelt thanks to my director of studies, Professor Mohsen Rahmani, for his constant support, for providing me with the best opportunities to learn and for teaching me the details of the nanofabrication process. His guidance extended beyond scientific knowledge, imparting invaluable life lessons. I also wish to thank my supervisor, Dr Cuifeng Ying, for her continuous support, particularly in teaching me about single-molecule knowledge and data analysis. Her belief in me from the very beginning and her precision in science have been always inspirational for me. My gratitude also goes to my advisor Associate Professor Lei Xu for his consistent support and scientific advice, which have been crucial to reaching this stage.

I am grateful to the Advanced Optics and Photonics (AOP) group and the broader academic community who have supported me. Special thanks to Ze Zheng for helping in the optical simulation part, and Mahya Assadipapari, Saaman Zargarbashi, and Gabriel Sanderson for their assistance with my project. A special acknowledgement to Dr Graham Hickman from the Imaging Suite at Nottingham Trent University who always supported me with technical support, Dr Demosthenes Koutsogeorgis from MTIF, and Professor Carole Perry from the Department of Chemistry and Forensics. I also acknowledge the support from colleagues at the University of Nottingham, particularly Professor Chris Mellor from the Department of Physics and Astronomy, Dr Chris Parmenter, and Dr Richard Cousins from the Nanoscale and Microscale Research Centre. Also, I acknowledge the help of Dr Carlos J. Bueno-Alejo.

I extend my appreciation to the Department of Engineering at NTU, and the technicians' team who consistently supported our technical issues. Special thanks to Dr Wendy Balestri, Nicolette Sizer, Mohammadreza Lalegani, Dr Jessica Stanley, Ruhani Khana, Dr Hannah Manley, Amin Zamani, Dr Sara Moujdi for fostering a friendly and supportive environment.

I am grateful to my friends, Noushin and Yasna, who supported me from a distance, and I offer special thanks to Soheila Nejati for always being there for me and my family. I also want to thank my local friends in the UK for their support and friendship.

Lastly, I want to express my deepest gratitude to my family. To my mother, Farideh Yousefi, for always believing in me, and to my father, Dr Kamran Yousefi, for his support and insightful questions that deepened my engagement with my PhD. Special thanks to my sister, Anoosheh Yousefi, who continually encourages me to grow personally and professionally, and to her wonderful family—Mehdi, Aroosha, and Ayla. My heartfelt thanks also go to my brother, Arash Yousefi, and his wife, Sara, for their persistent support throughout my PhD journey.

Contents

1	Chapter 1: Introduction	17
1.1	Why single-molecule studies?.....	18
1.2	Proteins are three-dimensional dynamic molecules	19
1.3	Labelling and tethering for single-protein studies.....	22
1.4	Label-free single-protein studies	23
1.5	History and background of optical trapping.....	24
1.5.1	Principals of optical trapping	24
1.5.2	Limitations of conventional optical tweezer traps	26
1.6	Plasmonic optical tweezers.....	27
1.7	Ferritin's structure and application.....	30
1.8	Thesis Outline.....	31
2	Chapter 2: Optical Characterisation of Proteins at Single-Molecule Level.....	33
2.1	Introduction	33
2.2	Single-molecule Föster resonance energy transfer (smFRET).....	34
2.2.1	Studying IDPs with smFRET.....	38
2.2.2	Studying membrane proteins with smFRET	39
2.3	Single-protein Raman spectroscopy	41
2.4	iSCAT and mass photometry	44
2.5	Optical tweezers	47
2.6	Whispering-gallery mode for single molecule sensing	49
2.7	Plasmonic optical tweezer approach	52
2.7.1	Fundamental theories of plasmonic forces.....	52
2.7.2	Self-induced back action (SIBA) trapping fundamental.....	54
2.7.3	Aperture-based optical trapping of a single protein using plasmonic optical tweezers.....	55
2.7.4	Integrating plasmonic effects into other single-molecule techniques ..	59
2.8	Conclusions and future of light-based single-molecule approaches	61
3	Chapter 3: Methodology	64
3.1	Introduction	64
3.2	Nanofabrication	64
3.2.1	Electron beam lithography	65
3.2.2	Focused ion beam (FIB).....	72
3.3	Simulations and modelling.....	75

3.4	Characterisation.....	77
3.4.1	Optical nanotweezers setup for characterising single proteins	77
3.4.2	Size exclusion chromatography analysis	84
3.4.3	Single-molecule mass photometry (MP) analysis.....	85
3.5	Data analysis.....	86
4	Chapter 4: Monitoring the Dynamic of Single Ferritin Molecules upon Iron Loading	87
4.1	Introduction	87
4.2	Optical nanotweezers distinguish between apo and holo-ferritin.....	89
4.3	<i>In situ</i> iron loading on single apo-ferritin molecules	96
4.4	Temperature at the trapping site	101
4.5	Control test of iron loading on single ferritin molecules.....	101
4.6	Conclusion.....	103
5	Chapter 5: Structural Dynamics and Disassembly of Single Ferritin Molecules	105
5.1	Introduction	105
5.2	DNH structures used in this study	107
5.3	Effect of ascorbic acid (AA) on the dynamic of single ferritin molecules	108
5.3.1	Impact of high AA concentration on the single ferritin transmission signal	113
5.4	Effect of acidic pH on the dynamic of single ferritin molecules.....	115
5.5	Tracking disassembly kinetic and fragmentation of single ferritin molecules	117
5.6	Conclusion.....	129
6	Chapter 6: Thesis summary and future work	130
6.1	Thesis summary.....	130
6.2	Future work	132
	References	135

I. List of Figures

Figure 1.1: Growing interests of researchers in the single molecule approaches from 1990 to 2025	17
Figure 1.2: The evolution of measurement techniques from analysing whole bodies to examining single cells and individual molecules.....	19
Figure 1.3: Time scale involved in protein dynamics and energy landscape	21
Figure 1.4: The model of radiation forces impacting a particle with a high refractive index within an optical trap	26
Figure 1.5: Schematic of SPPs and LSPs.....	28
Figure 1.6: Scanning electron microscopy (SEM) images of the plasmonic nanostructures....	29
Figure 1.7: Three-dimensional structure of horse spleen ferritin.....	31
Figure 2.1: Fluorescence and FRET processes are illustrated using Jablonski diagrams.	35
Figure 2.2: Schematic of smFRET with two approaches.....	37
Figure 2.3: Studying IDPs using smFRET.....	39
Figure 2.4: Illustrations of Raman scattering, SERS and TERS	42
Figure 2.5: Illustrations of the principles behind mass photometry	47
Figure 2.6: Schematic of immobilising a monomeric protein using optical tweezers setup.	49
Figure 2.7: Illustration of WGM sensors for single protein detection	51
Figure 2.8: Self-Induced Back Action (SIBA) effect on the trapping potential energy	55
Figure 2.9: Double nanohole (DNH) structure used in the optical tweezer setup and its field enhancements models	56
Figure 2.10: Using DNH Structures for single protein characterisation	58
Figure 2.11: Integrating plasmonic approaches with other single molecule techniques	61
Figure 3.1: Schematic of PECVD reactor for depositing thin films.	67
Figure 3.2: Electron scattering and dose distribution in electron resist.	69
Figure 3.3: Schematic representation of the EBL nanofabrication process.	71
Figure 3.4: Fabrication of DNH samples using FIB.	74
Figure 3.5: Simulated optical properties and field enhancement distribution of DNH structures.....	76
Figure 3.6: Diagram of the optical nanotweezer configuration.....	79
Figure 3.7: Trapping events in distinct DNH structures.....	81
Figure 3.8: Potential DNH geometry change after trapping experiments	82
Figure 3.9: Histogram showing the waiting time to trap a ferritin protein after the laser is activated.	83
Figure 3.10: Artifacts in single ferritin trapping using optical nanotweezers.	84
Figure 4.1: Single-molecule dynamics of apo- and holo-ferritin revealed by DNH.	90
Figure 4.2: Characterisation of single-molecule trapping dynamics for apo- and holo-ferritin.	93
Figure 4.3: Two trapping events of apo-ferritin within the same DNH structure.	94
Figure 4.4: Noise comparison across different frequency domains for the same DNH (#3) under various conditions.	95
Figure 4.5: In-situ iron loading into a trapped apo-ferritin	97
Figure 4.6: Level detection using standard deviation changes.....	98

List of Figures

Figure 4.7: Two repeat experiments of iron (Fe^{2+}) loading on a single apo-ferritin molecule.	99
Figure 4.8: Transmission signal RMS before and after biomineralization.....	100
Figure 4.9: Simulation estimates of laser heating.	101
Figure 4.10: Introducing iron (Fe^{3+}) to the trapped single ferritin molecule.....	102
Figure 4.11: RMS of the transmission signal after 20 min exposure to Fe^{+3}	103
Figure 5.1: Scanning electron microscopy (SEM) images of the five DNH structures utilised throughout this chapter	108
Figure 5.2: Impact of ascorbic acid on the dynamics and iron release of ferritin	110
Figure 5.3: Repeating test on the effect of AA on the dynamics of a single ferritin molecule.	111
Figure 5.4: Effect of AA on single apo-ferritin	113
Figure 5.5: Disassembly of a single ferritin exposed to 1.5 M AA.....	114
Figure 5.6: Conformational dynamics of a trapped ferritin under varying pH conditions..	116
Figure 5.7: Disassembly kinetics of single ferritin molecules	120
Figure 5.8: Disassembly stages of single ferritin at pH 2.0 (expanded view).....	120
Figure 5.9: A trace of single ferritin disassembly when exposed to pH 2, exhibiting non-stepwise behaviour.	122
Figure 5.10: Complete trace of stepwise disassembly for test 2.	122
Figure 5.11: Disassembly trace of test 3.	123
Figure 5.12: Exposure of Single apo-ferritin to pH 2.....	124
Figure 5.13: Kinetic analysis of single ferritin molecule disassembly. Error! Bookmark not defined.	
Figure 5.14: Mass photometry analysis of ferritin at buffer pH 7.4 and FPLC profiles of protein markers.	128

II. List of tables

Table 4-1: Change in the transmission signal of six different DNHS upon trapping apo and holo-ferritin proteins	92
Table 5-1: Disassembly of single ferritin molecules when exposed to pH 2.0	120

III. Publications and conference records

Publications:

- 1- **Yousefi, A.**, Zheng, Z., Zargarbashi, S., Assadipapari, M., Hickman, G.J., Parmenter, C.D., Sanderson, G., Craske, D., Xu, L., Perry, C.C., Rahmani, M. and Ying, C., 2024. Structural Flexibility and Disassembly Kinetics of Single Ferritins using Optical Nanotweezers. *ACS Nano*, 18 (24), 15617–15626.
- 2- **Yousefi, A.**, Ying, C., Parmenter, C.D., Assadipapari, M., Sanderson, G., Zheng, Z., Xu, L., Zargarbashi, S., Hickman, G.J., Cousins, R.B. and Mellor, C.J., Mayer, M., Rahmani, M., 2023. Optical Monitoring of In Situ Iron Loading into Single, Native Ferritin Proteins. *Nano Letters*, 23(8), pp.3251-3258.
- 3- Zheng, Z., Xu, L., Huang, L.J., Smirnova, D., Kamali, K.Z., **Yousefi, A.**, Deng, F., Camacho-Morales, R., Ying, C., Miroshnichenko, A.E. and Neshev, D.N., Rahmani, M., 2023. Third-harmonic generation and imaging with resonant Si membrane metasurface. *Opto-Electron. Adv*, 6(8), pp.220174-1.

Conference attendance:

Oral presentations:

- 1- **Yousefi, A.**, Zargarbashi, S., Hickman, G.J., Assadipapari, M., Zheng, Z., Sanderson, G., Parmenter, C.D., Xu, L., Rahmani, M. and Ying, C., Single-molecule analysis of ferritin conformational dynamics and kinetics using optical nanotweezers, Single-Molecule Sensors and NanoSystems International Conference – S3IC – Barcelona, Spain, Oral presentation, Nov 2023.
 - 2- **Yousefi, A.**, Zargarbashi, S., Hickman, G.J., Assadipapari, M., Zheng, Z., Sanderson, G., Parmenter, C.D., Xu, L., Rahmani, M. and Ying, C., Exploring the Impact of Iron Buffer and Acidic Environment on Single-Molecule Ferritin Dynamics Using Optical Nanotweezers, CCP4 - Northern Structural Biology Meeting, Nottingham, United Kingdom, Oral presentation, Oct 2023.
-

- 3- **Yousefi, A.**, Ying, C., Parmenter, C.D., Assadipapari, M., Sanderson, G., Zheng, Z., Xu, L., Zargarbashi, S., Hickman, G.J., Cousins, R.B. and Mellor, C.J., Mayer, M., Rahmani, M., “Single-molecule interrogation of Ferritin by plasmonic optical trapping” Photons 2022, IOP Conference, Nottingham, UK, Oral presentation, Aug-Sept 2022.

Poster presentation:

- 1- **Yousefi, A.**, Zargarbashi, S., Hickman, G.J., Assadipapari, M., Zheng, Z., Sanderson, G., Parmenter, C.D., Xu, L., Rahmani, M. and Ying, C, Single-molecule analysis of ferritin conformational dynamics and kinetics using optical nanotweezers, London plasmonic forum, London, UK, poster presentation, Jun 2024.
- 2- **Yousefi, A.**, Zargarbashi, S., Hickman, G.J., Assadipapari, M., Zheng, Z., Sanderson, G., Parmenter, C.D., Xu, L., Rahmani, M. and Ying, C., 2024. Single-molecule analysis of ferritin conformational dynamics and kinetics. Biophysical Journal, 123(3), p.287a. 68th Biophysical meeting- BPS- Philadelphia, US - Poster presentation, Feb 2024.
- 3- **Yousefi, A.**, Ying, C., Parmenter, C.D., Assadipapari, M., Sanderson, G., Zheng, Z., Xu, L., Zargarbashi, S., Hickman, G.J., Rahmani, M., Optical Monitoring of In Situ Iron Loading into Single, Native Ferritin Proteins, London plasmonic forum, London, UK, poster presentation, Jun 2023.

Summer school:

Plasmonica International School on Plasmonics and Nano-optics, Como, Italy, Jun 2024.

Yousefi, A., Zargarbashi, S., Hickman, G.J., Assadipapari, M., Zheng, Z., Sanderson, G., Parmenter, C.D., Xu, L., Rahmani, M. and Ying, C, Single-molecule analysis of ferritin conformational dynamics and kinetics using optical nanotweezers, Como, Italy, poster presentation- **(Best poster prize awarded)**, Jun 2024.

IV. Abbreviations

AA - Ascorbic Acid

AFM - Atomic Force Microscopy

APD - Avalanche Photodiode

ASC - Ascorbyl

CARS - Coherent Anti-Stokes Raman Scattering

CVD - Chemical Vapor Deposition

DLS - Dynamic Light Scattering

DNH - Double-Nanohole

EM - Electron Microscopy

FCS - Fluorescence Correlation Spectroscopy

FIB - Focused Ion Beam

FPLC - Fast Protein Liquid Chromatography

FTIR - Fourier-Transform Infrared

GPCR - G Protein-Coupled Receptors

ICP - Inductively Coupled Plasma

iSCAT - Interferometric Scattering

LSP - Localised Surface Plasmons

LSPR - Localized Surface Plasmon Resonance

MP - Mass Photometry

NA - Numerical Aperture

PB - Phosphate Buffer

PDF - Probability Density Function

PECVD - Plasma-Enhanced Chemical Vapor Deposition

POT - Plasmonic Optical Tweezer

RIE - Reactive Ion Etching

RMS - Root Mean Square

SEC - Size Exclusion Chromatography

SEM - Scanning Electron Microscopy

SERS - Surface-Enhanced Raman Scattering

SPP - Surface Plasmon Polaritons

STD - Standard Deviation

TIRF - Total Internal Reflection Fluorescence

1 Chapter 1: Introduction

Single-molecule techniques have revolutionised biology by enabling precise, real-time analysis of individual molecules. These capabilities have transitioned from scientific labs to commercial applications, as evidenced by companies like Oxford Nanopore Technologies (Oxford, UK), Illumina Inc. (San Diego, USA), and Refeyn Ltd (Oxford, UK), which now offer these technologies as commercial products. The growing importance of single-molecule techniques is highlighted by the increasing number of research publications in this field, reflecting their expanding relevance and impact in scientific research. Our statistical data extracted from the WEB of Science (**Figure 1.1**) shows a significant growth in the scientific literature on single molecules from 1990 to June 2025. This trend reflects the high level of interest among scientists in single-molecule techniques and approaches. In this chapter, we will explain the importance of single-molecule techniques and highlight various approaches. We will introduce the concept of optical tweezers as a single molecule technique, discuss its limitations, and explore how plasmonic optical tweezers address these limitations. The chapter will conclude with an outline of this thesis.

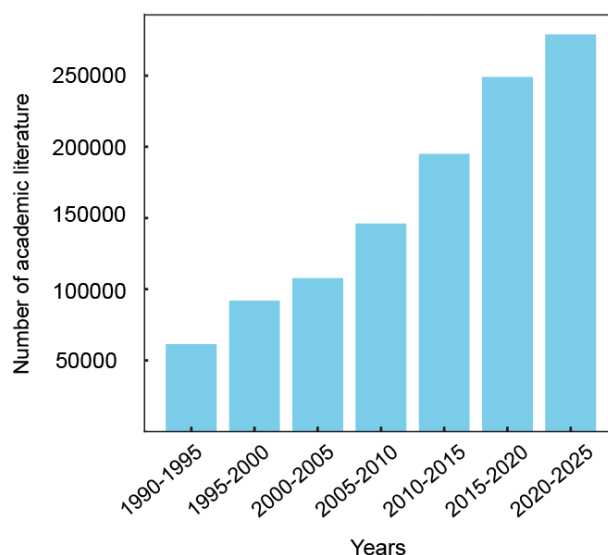


Figure 1.1. Growing interests of researchers in the single molecule approaches from 1990 to 2025 this data is retrieved from a search of WEB of Science (<http://apps.webofknowledge.com>) and using the single-molecule term: “(single-molecule OR single protein OR single enzyme OR single cell).”

1.1 Why single-molecule studies?

The scientific study of chemical reactions using quantitative methods has been established for over a century. Physical chemistry uses the mole as a unit of measurement, with 1 mole equating to approximately 6.022×10^{23} molecules (1). Standard experiments often utilise analyte concentrations ranging from nanomolar (nM) to millimolar (mM), involving 6.022×10^{14} - 6.022×10^{20} molecules (1). Ensemble approaches are effectively being used to study the interaction and physics of these molecules. However, for macromolecules (DNA, RNA, proteins, and enzymes) and surface reactions (e.g., on catalytic metal layers or cell membranes) which are essential in modern science, ensemble studies are insufficient to provide the underlying physical picture (2). These methods average out molecular heterogeneity, making detailed physical insights inaccessible in the sample (2).

Single-molecule and single-cell measurements provide far more detailed information than ensemble measurements (3,4). They can highlight biological systems' heterogeneities and stochastic processes. Single-molecule techniques can illustrate the heterogeneity of a biological system in two distinct ways. Dynamic heterogeneity refers to fluctuations in the state or behaviours of an individual molecule over time due to conformational changes, transient binding events, or shifts in enzymatic activity. Techniques such as FRET and optical tweezers fall into this category, as they enable the detection of real-time conformational changes and molecular interactions. Static heterogeneity, on the other hand, describes persistent differences between molecules in a population, where each molecule retains its unique properties over time due to variations in sequence, post-translational modifications, or structural differences, leading to distinct functional behaviours. Techniques such as nanopore sensing and AFM are particularly effective in detecting this form of heterogeneity (2-4). This detailed analytical information is crucial for detecting and quantifying rare, abnormal species that would be obscured in the noise of ensemble measurements (3,4). **Figure 1.2a** illustrates how measurement techniques have evolved from analysing whole bodies to individual cells and single molecules. This progression has advanced our understanding of biological functions, enabling us to study processes at the single-molecule level. Currently, analysis of biological samples stands at the cusp of **Figure 1.2a** where the study of individual molecules is evolving into a quantitative field, opening the door to the study of greater numbers of molecules (5). Some strategies are

shown in **Figure 1.2**: first, near-field measurements of single molecules are limited to single wells; second, wide-field capturing involves capturing molecules in bulk samples prior to near-field measurements; and third, future wide-field measurements are pursued in which multiple single-molecule measurements are tracked concurrently (5).

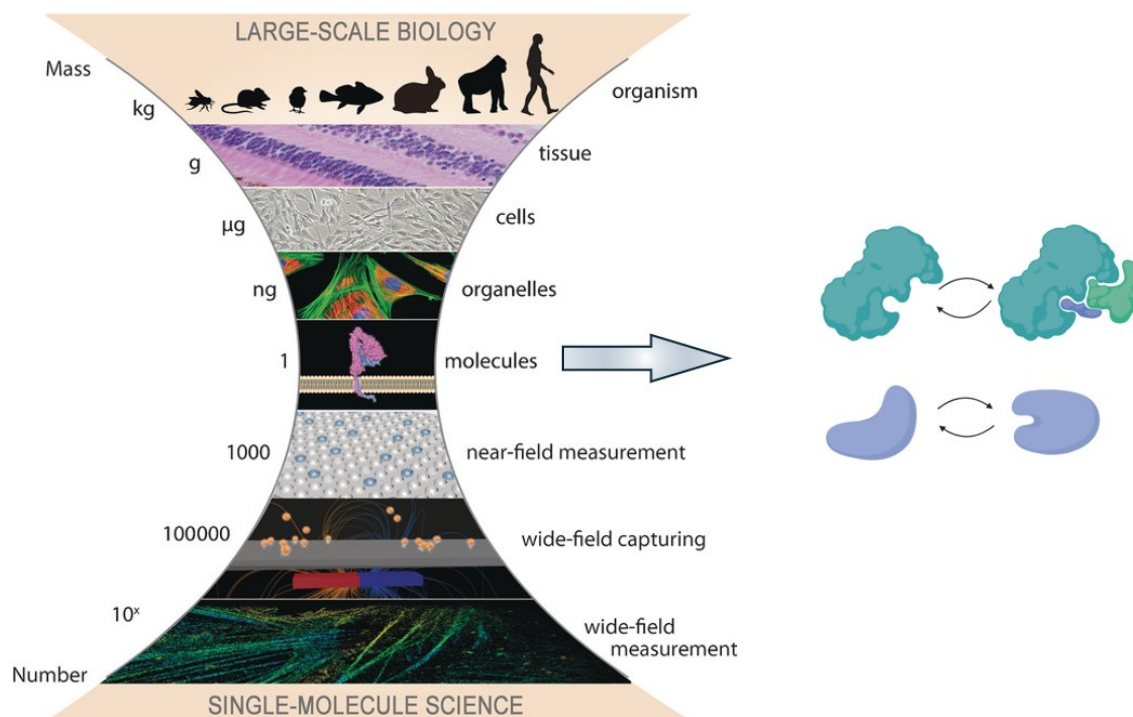


Figure 1.2: The evolution of measurement techniques from analysing whole bodies to examining single cells and individual molecules (5). The right inset is schematic illustrating conformational molecular shape and structure changes due to molecular interactions, impacting biomolecule dynamics (inset designed using biorender- www.biorender.com). Reprinted with permission from (5). Copyright 2016 John Wiley & Sons, Inc.

1.2 Proteins are three-dimensional dynamic molecules

The previous section highlighted key features of single-molecule study and its importance. This section focuses specifically on the significance of studying the dynamics of single molecules, particularly proteins. As the building blocks of biological systems, proteins are necessary for many vital cellular processes such as transcription, DNA replication, and DNA repair (6–8). Their dynamic behaviour, which includes interactions with biomolecules, conformational changes, and involvement in signalling cascades, is closely related to their functionalities (9,10).

Protein dynamics research is essential because abnormalities in protein dynamics might lead to some neurodegenerative diseases like Alzheimer's and Parkinson's (11).

The specific sequence of amino acids in a protein influence not only its three-dimensional shape but also its overall function. Proteins exhibit dynamic behaviour, fluctuating among different conformations over time, influenced by environmental factors like pH, salt concentration, and interactions with ligands (12–14). At the atomic level, proteins undergo rapid structural fluctuations within femtoseconds to nanoseconds. These include vibrational motions of chemical bonds and rotations of side chain groups (**Figure 1.3a**) (10). More substantial conformational changes, such as those involving loops or helices, can take place within nanoseconds to microseconds. However, larger-scale movements, such as those between subunits or domains, may require several seconds or even longer (15,16).

The constant thermal fluctuations within a protein's environment provide the energy necessary for its dynamic motion. This constant agitation allows the protein to explore a vast array of conformational states surrounding its equilibrium structure. The ability to change these conformations over various timescales is essential to their activity. A multidimensional energy map illustrates the potential energy of various molecular conformations and the energy barriers that must be overcome to transition between them (**Figure 1.3b**). This energy landscape, which is dependent on specific solvent, pressure, and temperature conditions, provides a comprehensive description of protein dynamics (16,17). The complex nature of these dynamics involves a wide range of timeframes, amplitudes, and directions of fluctuations (17). Single-molecule studies are crucial for understanding rare molecular events by assessing molecular mechanics and pathway likelihoods, highlighting the impact of local protein structure dynamics on function (18).

Some of the important approaches that have identified many proteins' three-dimensional structures with Angstrom-level resolution are X-ray crystallography (19), NMR spectroscopy (20), and Cryo-Electron Microscopy (21). The information from these approaches can be found in the Protein Data Bank (PDB), an essential resource for scientists, offering a comprehensive collection of static protein structures (22). Over the past 50 years, the PDB has expanded substantially and now includes more than 193,000 protein structures from 223,532 overall structures (August 2024).

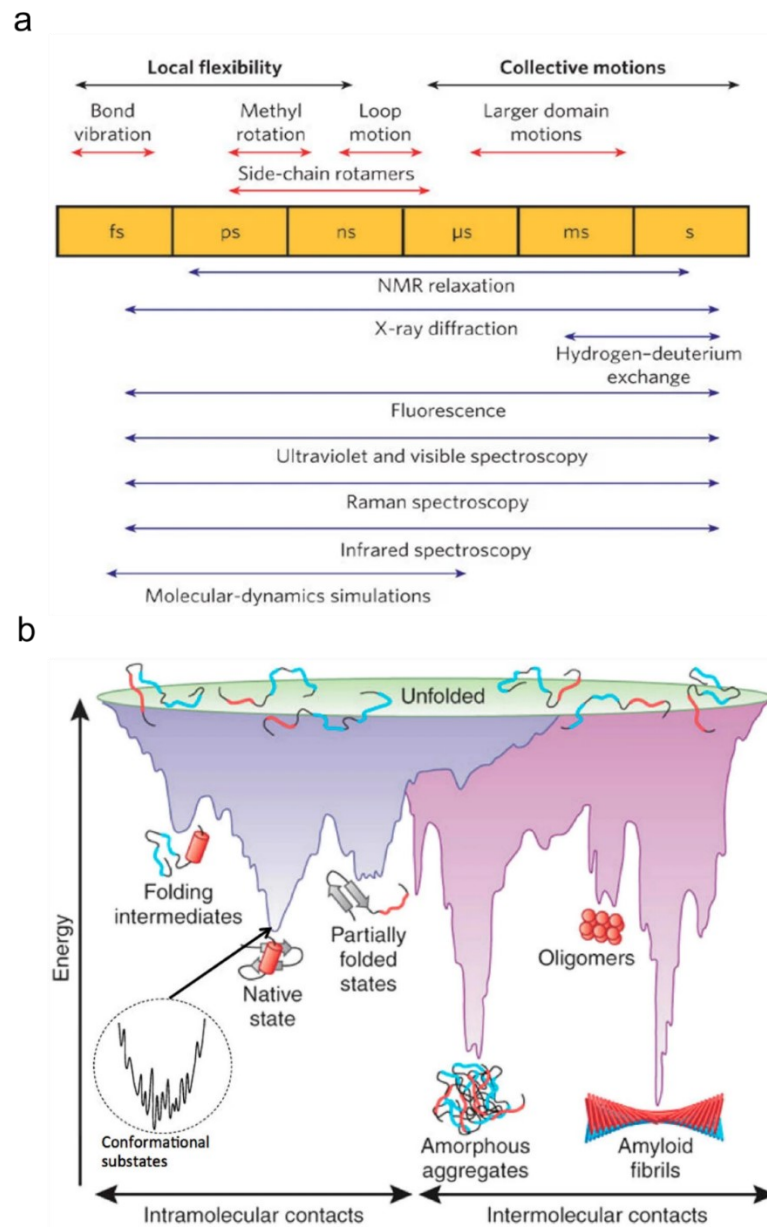


Figure 1.3: Time scale involved in protein dynamics and energy landscape. (a) The duration of dynamic processes in proteins and the experimental techniques capable of identifying variations within each timeframe. Reprinted from (16). Copyright 2007 Springer Nature. (b) A schematic energy landscape for protein folding and aggregation shows a funnel-like surface where proteins transition from high-energy, high-entropy unfolded states towards lower-energy states. This funnel represents the protein's free energy as it folds into its native state through intramolecular contacts or misfolds into amyloid fibrils via intermolecular contacts. Entropy is depicted as the width of the funnel, with the native state at the bottom, representing minimal energy and entropy, yet still allowing for dynamic fluctuations. Reprinted from (23). Copyright 2017 Springer Nature.

In the last few decades, a variety of experimental and computational methods have been developed to characterise the dynamics and structure of proteins. The majority of the data about the dynamics of proteins has been provided by X-ray crystallography (19), small-angle X-ray scattering (SAXS) (24), nuclear magnetic resonance (NMR) spectroscopy (20), and mass spectroscopy (25). Nevertheless, the experimental methods discussed above are ensemble measurement methods that call for millions of molecules to be synchronised (2). In the following, however, we will primarily concentrate on the single-molecule strategies that are currently being utilised to address issues that these ensemble approaches were unable to address in the past.

Techniques like atomic force microscopy (AFM) (26), combined with optical or magnetic tweezers (27,28), which fall under the category of force microscopy, that examines a molecule's extension under mechanical tension when it is linked to a force probe (29) have enabled precise measurement of bond energies (30), complete energy landscapes (31), and detailed data on the elasticity of nucleic acids (32). However, the attachment techniques and external forces used in force spectroscopy can interfere with the natural movements of proteins. Consequently, researchers are continually seeking alternative methods to study proteins in their natural state. Approaches focusing on light and optical-based methods have been applied to the study of individual proteins. Optical single-molecule techniques offer advantages over force spectroscopy, including the ability to study proteins without tethering and greater versatility in experimental applications (33). This versatility is demonstrated by diverse approaches like fluorescence-based methodologies (34), and plasmonic optical tweezer (35) each providing a distinct perspective for investigating single proteins. A range of studies have explored single proteins in different contexts, often requiring specific methods for their study like labelling and tethering, or in favourable cases, label-free approaches.

1.3 Labelling and tethering for single-protein studies

Labelling certain biomolecules is necessary for precise measurements and the elimination of protein interference (36). A visible marker or fluorophore is attached to the target protein of interest during the crucial labelling process (37). In addition to aiding the localisation and tracking of individual molecules, this labelling procedure facilitates the observation of dynamic structural changes and allows for the

measurement of interactions between proteins and their environment (38). There are many other labelling methods available, such as genetic tagging (34) techniques that fuse a fluorescent protein to the genetic sequence of the target protein or immunofluorescence (39,40), which uses antibodies conjugated with fluorescent dyes to attach to the protein of interest.

Alternatively, tethering is another useful technique for studying single biomolecules like proteins (41). Tethering, the immobilization of proteins for single-molecule studies, is a crucial technique that simplifies experimental systems and enables precise manipulation of external forces. This approach allows researchers to accurately investigate a protein's mechanical properties, folding dynamics, and interactions with other molecules (41). This method has been further developed, with the HaloTag system enabling covalent immobilisation of proteins for force spectroscopy (42). Recent advancements in tethering techniques for single-molecule studies include methods for autocatalytic covalent tethering of proteins with optical tweezers (43), isolating transmembrane proteins using membrane tethers (44), and measuring microbead motion with single DNA molecules (45), showing the diverse range of available tools and methods.

1.4 Label-free single-protein studies

Optical-based single-protein approaches mostly comprise wide-field fluorescence-based methods and conventional optical tweezers, which rely on labelling and tethering (46). Researchers have consistently sought approaches to study native single proteins and biomolecules without the need for labelling and tethering (47,48). This motivation stems from the desire to explore proteins in their native states to preserve their natural conformation and dynamics (49). Single-molecule techniques that do not require labelling, like whispering-gallery microcavities with ultrahigh Q (50), and plasmonic optical tweezers (51), have been shown to be superior to labelled techniques. By using these methods, labelling-induced changes in protein behaviour and possible artefacts are avoided.

Mass photometry and interferometric scattering microscopy (iSCAT) (52) are label-free optical-based techniques, but they cannot study the conformational dynamics of the protein of interest in real time. This limitation arises because these methods primarily measure the mass and refractive index of molecules, offering information on

size and aggregation but lacking the sensitivity to detect subtle, rapid changes in protein structure over time (53). Plasmonic optical tweezers (51,54–56), also referred to as optical nanotweezers in this thesis, enable the study of unmodified proteins over extended periods under physiological conditions. Here, we will first provide background and cover the basics of optical tweezers, followed by introducing optical nanotweezers based on plasmonic nanoapertures.

1.5 History and background of optical trapping

The first single-beam gradient force optical tweezers system was created as a result of Arthur Ashkin's groundbreaking work in the 1970s and 1980s, enabling the manipulation and characterisation of individual atoms and molecules (57,58) Ashkin's groundbreaking invention earned him the Nobel Prize in Physics in 2018 for its applications in biological systems. His initial experiments demonstrated the acceleration of latex microspheres by radiation pressure (57), followed by the levitation of transparent glass spheres (59), setting the groundwork for optical tweezers. Soon after, dielectric particles and neutral sodium atoms were trapped using these tweezers (60–62). Within a year, biologists applied them to manipulate viruses and bacteria (63). By the end of this decade, the biomedical applications of optical tweezers revealed their potential, leading to the demonstration of intracellular manipulation and surgery (64).

1.5.1 Principals of optical trapping

When a tightly focused electromagnetic beam with a Gaussian intensity distribution illuminates a particle, it creates two key forces: the scattering force and the gradient force. These forces are crucial for the stable trapping and manipulating particles in traditional optical tweezer setups. In the analysis, a perturbative framework is used, which assumes that the particle has a minimal effect on the surrounding electromagnetic field (65). Each photon in the incident beam carries momentum, p , inversely proportional to its wavelength:

$$\|p\| = \frac{h}{\lambda} \tag{1-1}$$

where h denotes Planck's constant and λ represents the wavelength of the incident radiation (65,66).

The scattering force is the result of photons applying radiation pressure to the particle (66). On the other hand, the gradient force arises from the incoming beam's axial intensity gradient. This force opposes radial particle displacement, ensuring a stable trap and forming the core mechanism in single-beam optical tweezers systems (65,66).

In the Mie regime, where particles are similar or larger than the incident wavelength, ray optics explain the forces involved (67). **Figure 1.4** illustrates a high refractive index particle positioned at the focus of a tightly focused Gaussian beam, where nearly all rays refract through the particle's centre without reflection (68). Rays of differing intensities, such as a and b , exert forces \vec{F}_a and \vec{F}_b on the particle upon scattering, respecting momentum conservation. The force \vec{F}_a from the higher intensity ray exceeds \vec{F}_b in magnitude (i.e., $|\vec{F}_a| > |\vec{F}_b|$) (68). These forces combine into two main components: the scattering force, \vec{F}_{scat} , aligned with the incident beam, and the gradient force, \vec{F}_{grad} arising from the beam's intensity gradient and directed towards its centre of highest intensity (68).

Particles in the Rayleigh regime, characterised by dimensions significantly smaller than the incident wavelength, experience forces comparable to those observed in the Mie regime. The scattering force originates from the particle's dipole moment and acts along the direction of the incident radiation, scaling proportionally to the sixth power of the particle's radius relative to the fourth power of the wavelength (58), expressed as:

$$|\vec{F}_{\text{scat}}| \propto \frac{1}{\lambda^4} \left(\frac{r}{\lambda}\right)^6 \quad 1-2$$

where r represents the radius of the particle and λ is the wavelength of the incident electromagnetic radiation.

Particles in the Rayleigh regime experience a gradient force that scales with the third power of particle size and is dependent on both the particle's polarisability and the gradient of the intensity of the electromagnetic field:

$$|\vec{F}_{\text{grad}}| \propto \left(\frac{r}{\lambda}\right)^3$$

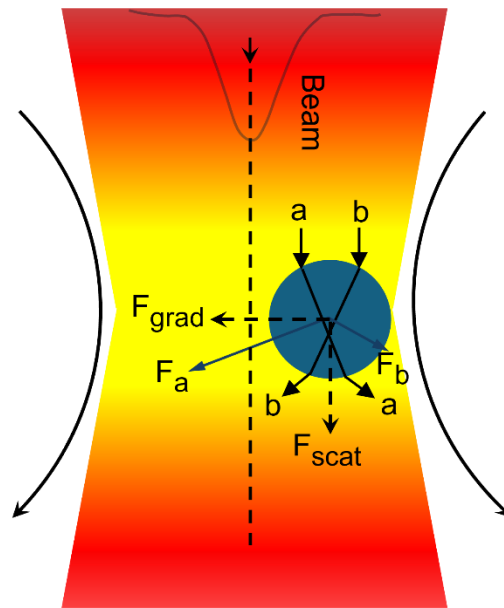


Figure 1.4: The model of radiation forces acting on a particle with a high refractive index within an optical trap (68).

1.5.2 Limitations of conventional optical tweezer traps

Single-beam gradient force optical tweezers have significantly impacted various scientific fields. However, they have inherent limitations, particularly with smaller particles in the Rayleigh regime and biomolecules (69).

In order to successfully trap a particle using single-beam optical tweezers in a homogeneous fluid environment, it is required to overcome both Stokes' drag and thermally induced Brownian motion. Stokes' drag refers to the resistive force a spherical particle experiences as it moves through a viscous fluid. The required optical power to counter Brownian motion correlates inversely with the fourth power of the particle's size (58), while the viscous drag scales linearly with the size (70). As particle size decreases, the gradient force becomes more prominent than the scattering force; however, its magnitude is limited to the third power of the particle's size (66).

For biomolecules, which are nearly two orders of magnitude smaller than the diffraction limit, the required optical power for trapping is significantly higher and heating leads to damage of molecules (71). To effectively trap such small biomolecules, it is necessary to move beyond the traditional perturbative framework, enabling particles to induce significant changes in the electromagnetic field at low optical intensities.

1.6 Plasmonic optical tweezers

Efforts to trap objects with reduced sizes to the nanoscale through advancements in near-field optical techniques have opened new possibilities in various fields, including biology, nanoelectronics, and photonics (72). Among these technical advancements, surface plasmon engineering stands out for its potential in nanoscale manipulation (73,74). Surface plasmons (SPs) are electromagnetic waves that propagate along the surface of a conductor. These waves can take the form of surface plasmon polaritons (SPPs) at planar metal-dielectric interfaces or localized surface plasmons (LSPs) at confined geometries like nanoparticles (**Figure 1.5**) (51). SPs exhibit an evanescent nature, decaying exponentially away from the interface. This property concentrates the electromagnetic field near the surface, therefore compared to normal incident radiation a high intensity field is experienced in this area (51). The shorter wavelength of SPs allows for nanoscale focusing, generating a strong electromagnetic force ideal for nanoscale trapping, thus driving research into plasmonic trapping and manipulation techniques (51,75).

Using conductive metals such as silver and gold to create nanostructures can effectively manipulate light in small areas (76). Additionally, advancements in nanofabrication have led to more sophisticated nanostructures such as nanoantennas and nanoapertures, improving trapping capabilities (77). Nanoantennas, such as cubes (78), bowtie (79), and cylindrical (80) (**Figure 1.6 a-c**) produce extremely concentrated field gradients that will allow for the optical trapping of particles in the sub-100 nm range (75)

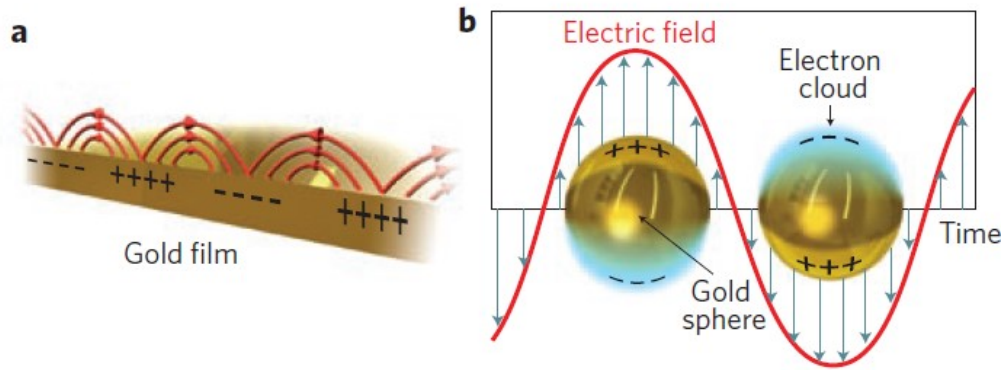


Figure 1.5: Schematic of SPPs and LSPs. (a) surface plasmon polaritons (SPPs) propagating along a gold film. SPPs are coherent electron oscillations coupled to electromagnetic waves, confined to the interface between the gold film and the surrounding dielectric. (b) Illustration of localised surface plasmons (LSPs) in a gold sphere. LSPs occur when the electron cloud in a nanoparticle oscillates in resonance with the incident electromagnetic field, creating strong electric fields at the nanoparticle surface. Reprinted with permission from (51) Copyright 2011, Springer Nature Limited.

Nanoaperture structures (**Figure 1.6 d-f**), including double nanoholes (DNH) (**Figure 1.6 f**), have recently been used for single biomolecule detection (56,75,81) These apertures are created mostly by milling cavities in a thick film or bulk sample. A sub-wavelength aperture in a metal film is illuminated by electromagnetic radiation, which produces LSPs. This confines the high-intensity field gradient inside the aperture (81). This significant field gradient, existing in a region smaller than the diffraction limit, is ideal for trapping very small particles such as proteins without needing increased optical power (56,81,82).

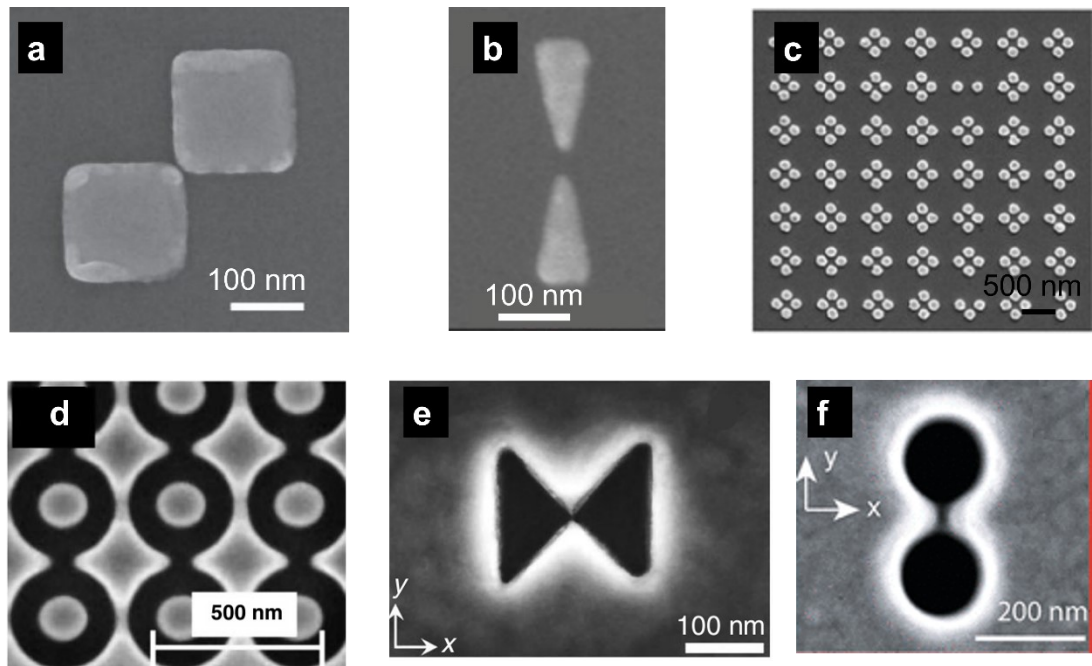


Figure 1.6: Scanning electron microscopy (SEM) images of the plasmonic nanostructures (a-c embossed nanostructures, d-f nanoapertures). (a) Gold nanoblock (nanocubes). Reprinted with permission from (78). Copyright 2013 American Chemical Society. (b) Bowtie nanostructures. Reprinted with permission from (79). Copyright 2013 American Chemical Society. (c) Cylindrical nanostructures. Reprinted with permission from (80). Copyright 2013 American Chemical Society. (d) Nanoring apertures. Reprinted from (83). Copyright IOP Publishing Ltd. (e) inverted bowtie nanoaperture. Reprinted from ref (84). Copyright, the Authors 2018. (f) Double nanohole (DNH) aperture. Reprinted with permission from (56) Copyright 2012 American Chemical Society.

In this thesis, we use optical nanotweezers with nanophotonic structures, primarily DNH structures (56,82), to study the behaviour of single proteins, mainly ferritin. We chose the optical nanotweezer approach because it allows us to study single ferritin without modification and label-free over extended periods. Additionally, by integrating a fluidic system, we can monitor the effects of different media and solutions on the dynamics of proteins such as ferritin.

In the field of plasmonic nanostructures, a major drawback is heating generation due to ohmic loss (85), which can affect the dynamics and behaviour of the protein being studied. To address this, dielectric nanostructures such as silicon structures are promising as they have low absorption in the near-infrared and visible ranges (86). However, the fabrication of these structures that match initial designs is complicated, and their field enhancement is lower compared to plasmonic ones. This challenge can

be addressed through the efficient design of nanostructures. During my PhD, I also worked on fabricating dielectric structures, though they still need optimisation for efficient trapping. This can be a future direction for further research and development.

1.7 Ferritin's structure and application

Iron is essential for numerous cellular processes, and ferritin serves as the primary intracellular protein responsible for iron storage and release. Consequently, ferritin expression has been observed in all cell types investigated thus far (87). Ferritin is crucial in keeping cellular iron balance by serving as an accessible iron reservoir for crucial biomolecules involved in various physiological processes. Iron is required for diverse functions, including DNA synthesis, oxygen transport, electron transfer, nitrogen fixation, and the production of haemoproteins such as myoglobin and haemoglobin (88,89).

Ferritin contributes to both short-term iron buffering, as observed in hepatocytes, and long-term iron storage, such as in macrophages, where it plays a role in iron recycling (89). Ferritin also plays a crucial role in protecting cells from iron's potential toxicity, alongside its storage and release functions (90). Under physiological pH and oxygen tension, iron readily cycles between its ferrous (Fe^{2+}) and ferric (Fe^{3+}) states. Fe^{2+} can be oxidised to Fe^{3+} , which subsequently undergoes hydrolysis to form insoluble ferric hydroxide and oxyhydroxide polymers (91).

Ferritin is a large, spherical protein complex, approximately 10-12 nm in diameter, with a protein mass of around 450,000 Da (**Figure 1.7**) (92). Its 1 nm thick protein shell encloses a ferric oxide (Fe^{3+}) core capable of sequestering up to 4,500 iron atoms, along with varying amounts of phosphate. This shell comprises 24 subunits, each around 20 kDa, which interact with the iron core at specific points, forming iron-protein interfaces. The ferritin shell contains channels, primarily threefold and fourfold, that facilitate ion transport (**Figure 1.7 a,b**) (92,93). While animal ferritins predominantly use threefold channels for iron uptake, plant and bacterial ferritins employ both threefold and fourfold channels (87,94). In plants, both channel types are crucial for iron uptake and oxidation, as disruptions to either reduce this activity. Research on the prokaryotic ferritin SynFtn has demonstrated that iron enters via threefold channels, with the amino acids Asp137 and Glu62 playing key roles in iron uptake and the subsequent release of oxidised iron products, respectively (93,95).

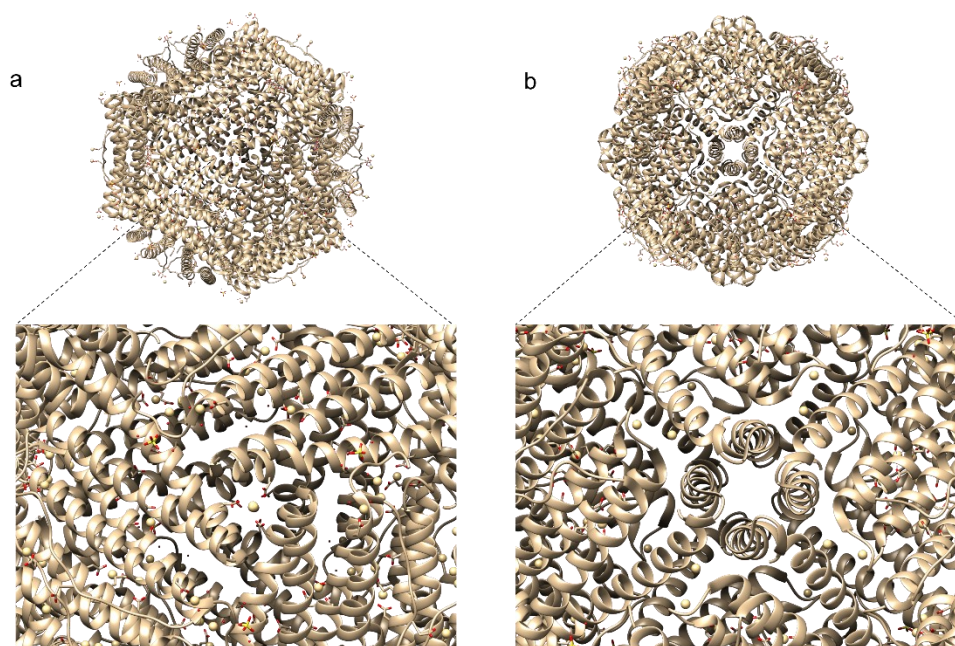


Figure 1.7: Three-dimensional structure of horse spleen ferritin (PDB:2W00) and close up view of channels. (a) Structure of three-fold channels, which consist of three symmetry-related subunits forming a narrow pore, (b) Structure of four-fold channels, composed of four subunits.

Ferritin's potential for a delivery vehicle for drugs stems from its native targeting function and diversity in cargo loading (96). Binding specifically to transferrin receptor 1 (TfR1), a molecule overexpressed in most types of tumours cells, enables selective delivery of drugs to cancerous tissues (96). The inner cavity of ferritin can encapsulate a variety of drugs, including chemotherapeutic and imaging drugs, and its therapeutic value can, therefore, be enhanced. Targeting groups such as peptides or antibodies can even re-engineer ferritin's outer surface for enhanced specificity. Targeted delivery can then be triggered with stimuli such as pH, redox environment, enzymes, or external stimuli, with minimum off-target toxicity (96–99).

1.8 Thesis Outline

In this thesis, we studied the behaviour and dynamics of single ferritin molecules using an optical nanotweezer setup. We explored various scenarios, including the effects of iron loading on the dynamics of single ferritin molecules, as well as their disassembly dynamics and kinetics.

In Chapter 2, we provide a comprehensive review of light-based single-molecule techniques used to study protein dynamics. These techniques include smFRET, iSCAT and mass photometry, optical tweezers, and single-molecule plasmonic approaches.

Chapter 3 contains the methodology and experimental design of this thesis. It details the various techniques used for fabricating nanophotonics (DNH samples and dielectric samples), predicting optical resonances, and integrating the devices into our optical tweezer setup. This chapter also covers the microfluidic setup, buffer and protein sample preparation, and the additional methods used for characterising proteins, such as chromatography techniques and mass photometry. This chapter also explains our data analysis methods.

Chapter 4 explores the differences in the dynamics of apo-ferritin and holo-ferritin in the DNH trap. After distinguishing between these two forms of ferritin, we studied the effect of iron loading on single ferritin molecules in situ. This chapter reveals the kinetics and dynamics of the ferritin channels during iron loading, investigated at the single-molecule level for the first time.

Chapter 5 examines the behaviour of ferritin during iron unloading using ascorbic acid (AA) at different concentrations. It also analyses the disassembly kinetics and dynamics of ferritin at the single-molecule level at pH 2, showing that ferritin undergoes stepwise disassembly through its subunits. Additionally, we assessed the dwelling time of the subunits during the disassembly process in the trap. This chapter also employs mass photometry as an orthogonal approach to study the disassembly pathway of ferritin to give a comprehensive insight into ferritin disassembly at the single-molecule level.

Chapter 6 concludes the thesis, summarising key results and providing an outlook for future work.

Chapter 2: Optical Characterisation of Proteins at Single-Molecule Level

2.1 Introduction

In Chapter 1, we introduce the dynamic nature of proteins, emphasising the significance of studying individual protein molecules. Understanding single proteins is crucial because it allows us to unravel their specific functions, mechanisms, and interactions at a fundamental level, which is often obscured in bulk studies (48). In this chapter, we will review single-molecule techniques for studying proteins, with a particular focus on optical approaches. Optical methods, smFRET (single-molecule Förster Resonance Energy Transfer), or optical nanotweezers offer several advantages over force spectroscopy techniques. These advantages include higher temporal resolution, the ability to observe real-time dynamics in living cells, and the capability to investigate interactions and conformational changes without applying external forces that might alter the protein's natural behaviour (33). Optical approaches also enable the study of proteins in their native environments, offering a valuable understanding of their physiological roles and contributing to our knowledge of complex biological processes. In this chapter, we will discuss various optical techniques employed in single-protein characterisation. These include single-molecule smFRET, single-molecule Raman spectroscopy (SERS), Interferometric Scattering Microscopy (iSCAT) and its derivative, mass photometry. Additionally, we will cover optical tweezers, the whispering gallery mode single-molecule approach, and single-molecule plasmonic optical tweezers (optical nanotweezers). Each of these methods offers unique advantages for probing the structure, dynamics, and interactions of individual protein molecules. We will conclude with an integrated perspective on how these optical approaches contribute to our comprehensive understanding of protein function and their potential applications in biomedical research.

2.2 Single-molecule Förster resonance energy transfer (smFRET)

Since fluorescence spectroscopy was first used to identify a single molecule in 1990 (100), it has become widely used in a variety of research fields, such as materials science (101), soft-matter studies (102), nanophotonics (103), and molecular cell biology (104). This method is based on identifying the fluorescent signals that the target emits (18,105). The process entails the absorption of a photon, which excites the fluorophore from S_0 which is an electronic ground state to S_1 an excited state (105). The molecule then relaxes to the lowest vibrational level of S_1 , which enables it to release a photon and return to the ground state (**Figure 2.1**) (2,105). Notably, there is a red-shifted emission because the energy of the photon that is released is less than the energy of the photon that is absorbed. The technique based on the fluorescence emission, including smFRET is the well-known method in single-molecule studies that is mostly used for biomolecular structure and dynamics (2,100).

smFRET is an advanced technique building upon FRET principles, a non-radiative energy transfer between a donor and an acceptor through dipole-dipole interactions in their electronic states (2). Although FRET doesn't precisely measure absolute distances, it serves as a valuable "spectroscopic ruler" because it measures the efficiency of energy transfer between two fluorophores, which correlates with the distance between them (2). smFRET experiments have three essential requirements. First, biomolecules need site-specific labelling with donor and acceptor fluorophores within Förster distance which is approximately less than 10 nm and shows the molecular separation at which energy transfer is 50 percent effective (106). Second, low molar concentrations (usually less than nanomolar) to ensure the presence of only one molecule in the observation volume (106). Third, a small observation volume (ranging from 0.1 to 1 femtoliter) is preferred as it enhances the signal-to-noise ratio (S/N) (106). The molecules of interest are tagged with distinct donor and acceptor fluorophores in smFRET investigations that focus on conformational changes or intermolecular interactions. Stable fluorophores under high photon intensity are ideal for smFRET, and those possess high molar absorptivity and fluorescence quantum yield and exhibit minimal "blinking." These characteristics ensure reliable and detailed investigations of dynamic molecular events at the single-molecule level (106,107).

For smFRET, fluorophores are generally small organic molecules such as Cyanine dyes (< 1 nm), with common options including Cy3 (greenish yellow, ~ 550 nm excitation, ~ 570 nm emission) and Cy5 (far-red region, ~ 650 nm excitation, ~ 670 nm emission) (106,108) as well as substitutes such as ATTO dyes and Alexa Fluor (109). Although fluorescent proteins and quantum dots can be employed, they present additional implementation challenges due to their larger size (106,110).

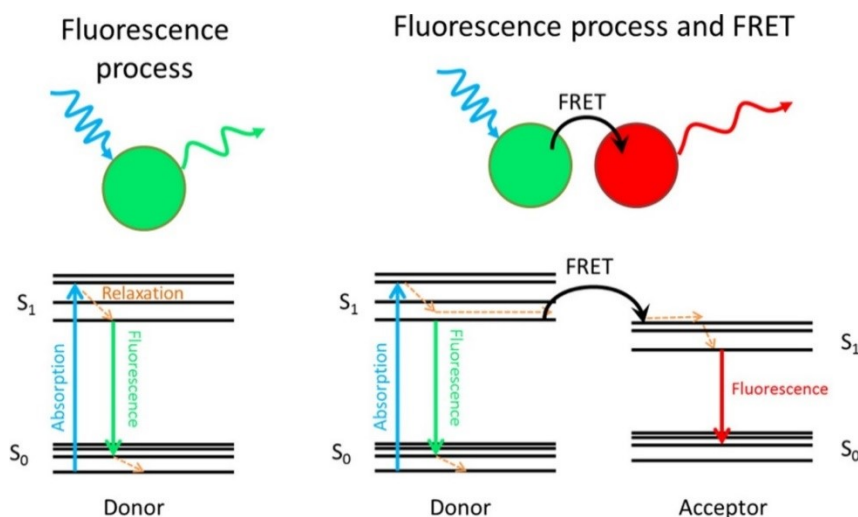


Figure 2.1: Fluorescence and FRET processes are illustrated using Jablonski diagrams. On the left, the diagram shows a fluorophore's excitation state and the fluorescence relaxation process. On the right, it depicts the FRET process, where the donor molecule is excited due to its proximity to the acceptor molecule. This proximity allows the FRET process to excite the acceptor, causing it to relax and emit light at a different wavelength than the donor in a typical fluorescence process. Reprinted from (105). Copyright 2016 the authors.

There are two common approaches to studying smFRET: confocal and Total Internal Reflection Fluorescence (TIRF) imaging (46,111). Confocal microscopy is useful for studying molecules that are freely diffusing (**Figure 2.2a**), whereas TIRF microscopy is used for molecules that are immobilised on surfaces (46) and a quartz prism or a high numerical aperture objective can be used to perform TIRF (**Figure 2.2b**) (112).

Molecules freely diffuse into the observation volume in the confocal technique, making it possible to acquire many single-molecule events over long times at rates of a few events per second (46,113). Even with sub-microsecond temporal resolution, individual molecules are only detected after they diffuse through the confocal excitation volume, a process that typically takes a few milliseconds (113,114). This makes it possible to take hourly pictures of thousands of different molecules (114).

TIRF enables the simultaneous visualisation of hundreds to thousands of fluorescently labelled molecules within a single field of observation. (112). This technique enables the observation of dynamic "motion pictures" of individual molecules, capturing events like photobleaching over time intervals of seconds. While the temporal resolution of TIRF is often limited to a few tens of milliseconds, this is improving with technical advancements such as faster cameras, improved illumination systems, enhanced data acquisition methods, and advanced computational algorithms for real-time analysis (115).

Analysing smFRET experiments typically includes two steps (116). In the confocal setup, individual molecules are detected as "bursts" of fluorescence that significantly rise above the background signal (**Figure 2.2a-right panel**). Transfer efficiencies are then calculated for each burst and compiled into a histogram, which helps identify subpopulations, determine mean transfer efficiencies, and analyse the distribution patterns (116). TIRF has the advantage of reduced background fluorescence due to the selective excitation of molecules near the surface (**Figure 2.2b**).

Numerous proteins are anticipated to exhibit rapid conformational changes (ms-ns), making them suitable for FRET measurements due to their spatial amplitude (114). With a focused laser beam in a confocal microscope, these proteins can be studied under freely-diffusing conditions in a solution (117). By defocusing the laser beam or attaching the protein to a bigger freely diffusing object like a lipid vesicle, the molecule's typical diffusing period in the focal volume can be extended to about 1 ms (18,114,118). By using single-photon avalanche photodiodes, one can precisely monitor acceptor and donor photon arrival times down to the picosecond level by capturing the photons released by each molecule moving through the beam (119).

smFRET finds versatile application in probing protein folding (120), conformational dynamics (116), ion channel dynamics (121), T cell receptors, antigen interactions (122), dynamics of Epidermal Growth Factor Receptor (EGFR), and ligands binding (123), as well as the structure of DNA and RNA (124). In this section of this chapter, we concentrate on the dynamic behaviour of two protein categories that are crucial in

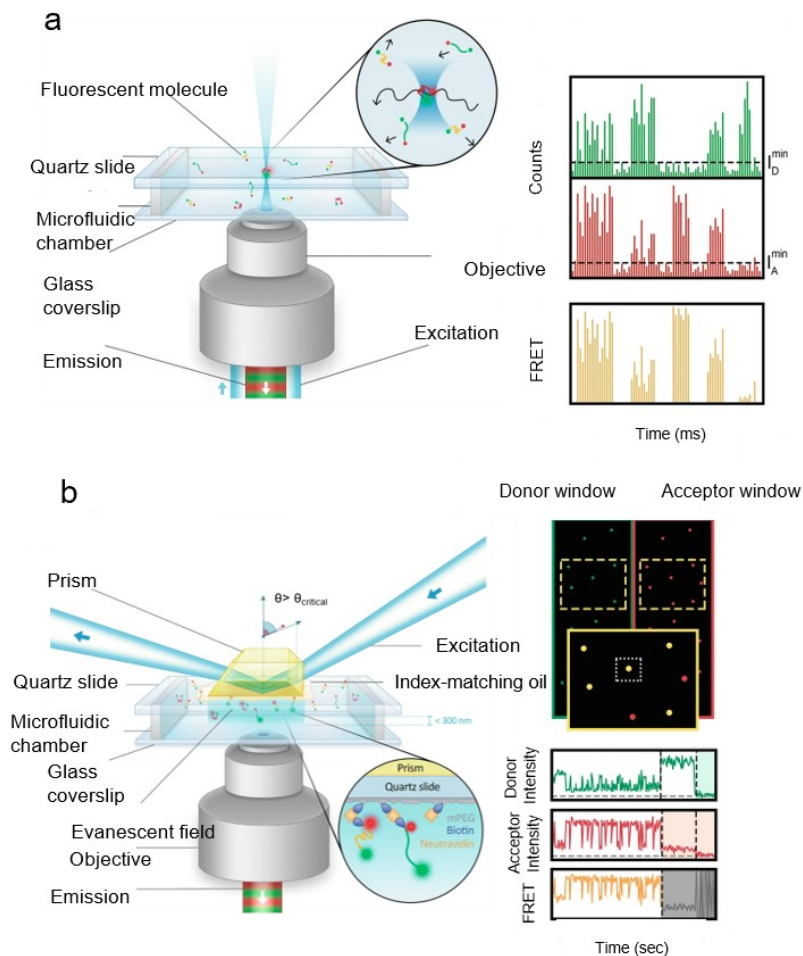


Figure 2.2: Schematic of smFRET with two approaches. (a) Confocal microscope illustration: Laser focuses on freely diffusing molecules within the sample, and fluorescence is collected through the same objective. Right panel: Confocal FRET data: Bursts of photons detected by donor (green) and acceptor (red) detectors. Events such as donor-only, acceptor-only, intermediate FRET, and high/low FRET signals, while above the predetermined intensity levels (dashed lines) are regarded as real. FRET values in the final analysis, when low-intensity donor-only and acceptor-only subpopulations were eliminated, are shown by yellow lines. (b) TIRF microscope: Incident laser light passes through a prism into the interface with a sample at a super-critical angle and excites molecules within a very thin region near the surface. The fluorescence signal is collected by a camera. Right inset: TIRF FRET data: image of immobilised donor and acceptor molecules, showing FRET efficiency through dual-channel signal observation. Donor and acceptor photobleaching are showed in single-molecule trajectories. Reprinted with permission from (125). Copyright 2022 The Author(s), under exclusive license to Springer Nature Switzerland AG.

disease and drug design: Intrinsically Disordered Proteins (IDPs) and membrane proteins (119,126,127). The versatility of smFRET makes it an invaluable tool for unravelling the structural complexities and dynamic behaviour of these biomolecules.

2.2.1 Studying IDPs with smFRET

The high resolution of smFRET has recently facilitated the investigation of intrinsically IDPs, characterised by a lack of stable secondary structures (128,129). IDPs play crucial roles in biological functions and are associated with degenerative diseases like Alzheimer's (119,126). Compared to traditional methods like X-ray crystallography and NMR, smFRET offers unique advantages for studying IDPs because it can capture their diverse and constantly changing structures (119).

For example, Wen. et al. (130) used smFRET to show that full-length Tau protein alters structurally, adopting more stretched conformations in the presence of molecular crowding and under circumstances of liquid-liquid phase separation (LLPS) (**Figure 2.3a**). smFRET has also been used to study the aggregation-prone IDPs. Wickramasinghe et al. (131) employed smFRET spectroscopy to study tau protein aggregation with cytoplasmic polyphosphates. The research identified processes initiating tau aggregation and polyphosphates' role in altering tau conformation, showing their impact on noncovalent cross-linking among tau monomers.

Interactions involving IDPs exhibit diverse structural outcomes. Binding events may lead to the IDPs adopting a defined / partially defined structure, or the retention of complete disorder (132). Therefore, to understand these protein-protein interactions, applying complementary techniques to single-molecule methods, such as molecular dynamic (MD) simulations, can be useful (133). Heesink et al. (134) combined smFRET and MD simulations. to study specific amino acid interactions that cause structural deviations in the α -synuclein. They showed that within α -synuclein, these amino acid interactions give rise to both compact regions, demonstrated by the NAC (non-amyloid- β component) region, and expanded regions, such as the C-terminal domain.

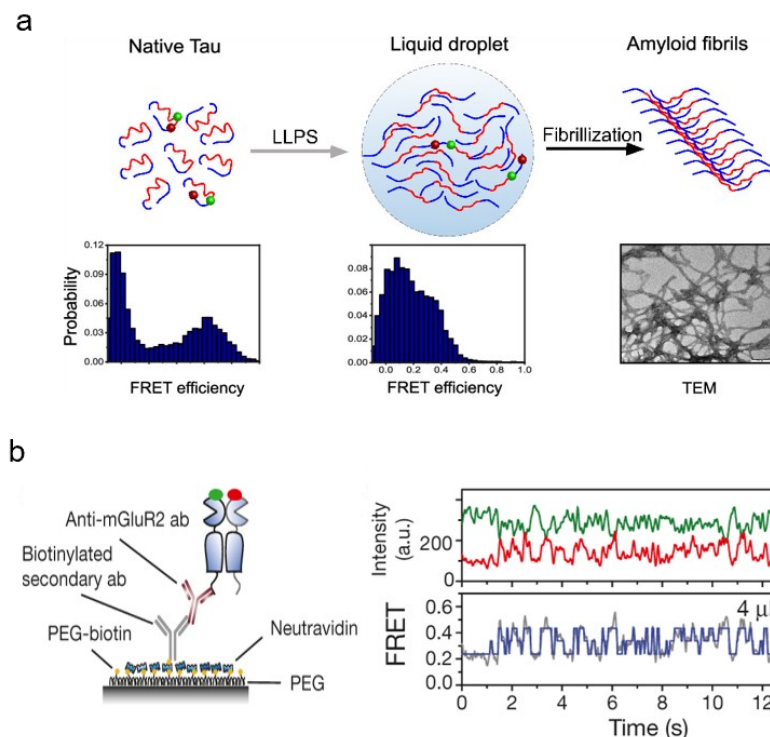


Figure 2.3: Studying IDPs using smFRET (a) Using smFRET techniques to study intermolecular and intramolecular changes in the Tau protein resulting from liquid-liquid phase separation (LLPS). Reprinted from (130) (CC-BY-NC-ND 4.0). (b) Surface-immobilised mGluR2 proteins were tagged with donor (green) and acceptor (red) fluorophores to monitor conformational changes via smFRET in the presence of 4 μM glutamate. The intensity traces (top) and corresponding FRET efficiency (bottom) show dynamic fluctuations, indicating real-time changes in the protein's conformational states. Reprinted with permission from (135) Copyright 2015, Springer Nature Limited.

2.2.2 Studying membrane proteins with smFRET

About one-third of cellular proteins are membrane proteins, of which about 60% are targets for pharmaceuticals (127,136). They are necessary to produce energy, ion balance, signal transduction, and catalysis (127,137). Their activities depend on proper folding, and any failure to fold, frequently resulting from single-point mutations, can cause severe genetic illnesses like cystic fibrosis (127,137). Therefore, understanding the variables affecting membrane protein dynamics and structures is essential for both biology and medicine, providing information on possible therapies for diseases involving membrane protein folding (127). Using smFRET in studying membrane

proteins is essential due to their lipid bilayer environment which the protein's structural change happens inside this complex layer (127). smFRET provides real-time, single-molecule resolution of dynamic processes, enabling the direct observation of conformational changes and interactions that occur within individual membrane proteins. For example, receptor proteins, particularly GPCRs (G protein-coupled receptors), play a vital role in cellular responses and are targeted by a significant portion of drugs (138). The diverse conformations of GPCRs, revealed through structure determination, have inspired interest in drug design, cell biology, and structural biology (138). By using smFRET, Vafabakhsh et al. (135), revealed the activation mechanism of full-length mammalian group II mGluRs. They discovered that the ligand-binding domains (LBDs) transitioned between three states: resting, activated, and transient intermediate. The filtered raw data and a three-state fit from hidden Markov analysis showcased rapid dynamics at 4 μ M glutamate (**Figure 2.3b**).

Transporters, a significant class of membrane proteins, play a vital role in facilitating the movement of molecules within cell membranes, crucial for processes such as nutrient uptake, waste removal, and signal transduction (139). smFRET proves helpful in studying diverse transport proteins, including ion channels, transporters, and ATP-binding cassette (ABC) transporters (139,140). For instance, using smFRET, Ling Wang et al. (140), demonstrated that ATP-binding induces nucleotide-binding domains (NBD) dimerisation, shifting the transporter to a stable outward-open conformation, which persisted for over 20 seconds under saturating ATP conditions.

smFRET approaches, despite being innovative, have drawbacks. The need for specific fluorophores for labelling can alter the dynamics of biomolecules (141,142). Ambient conditions, background noise, and photophysical characteristics introduce variability in the test results (142,143). Current developments such as non-covalent labelling strategies that minimise perturbations to biomolecular dynamics, advanced fluorophores with improved photostability and reduced background noise, and enhanced data analysis algorithms that account for photophysical variability, all of which aim to refine the accuracy and reliability of smFRET measurements in diverse biological contexts (106).

2.3 Single-protein Raman spectroscopy

Raman spectroscopy is an analytical technique based on the principle of inelastic light scattering, first predicted by A. Smekal in 1923 (144,145). The principle of inelastic light scattering, also referred to as Raman scattering, can occur in two possible ways. The most common is Stokes Raman scattering where upon interaction of a photon from the incident light, a molecule becomes excited and rises from the ground state to an unstable virtual vibrational energy state (146,147). This state is transient and results in the molecule typically falling back to the ground state and releasing a photon of the same wavelength as the incident light, referred to as Rayleigh or elastic scattering, however very rarely an electron in the virtual state can fall to an excited state and result in the release of a photon of lower energy, hence a different wavelength, to the incident light (146–148). The other, less common occurrence is that of Anti-Stokes Raman where the molecule is already present in an excited state before absorbing an incident photon and subsequently falling to the ground state (147). This results in the emission of a photon of greater energy than the incident light, although most Raman techniques focus on Stokes Raman scattering (146–148). Both scattering types are illustrated in **Figure 2.4a**.

Inelastic scattering is key to Raman spectroscopy, enabling applications like material characterisation (149) and sample detection (150). Each molecule has unique vibrational energy states matching its chemical composition, creating distinct fingerprints in the scattering patterns (151,152). There are now many different types of Raman spectroscopic techniques with there being over 25 different types (153) including hyper-Raman (154), coherent anti-Stokes Raman scattering (CARS) (155) and Fourier transform Raman scattering (156). The types covered in this section will be those with potential use in the context of single molecule studies, with a focus on proteins, which would allow for both the detection and chemical analysis of the protein.

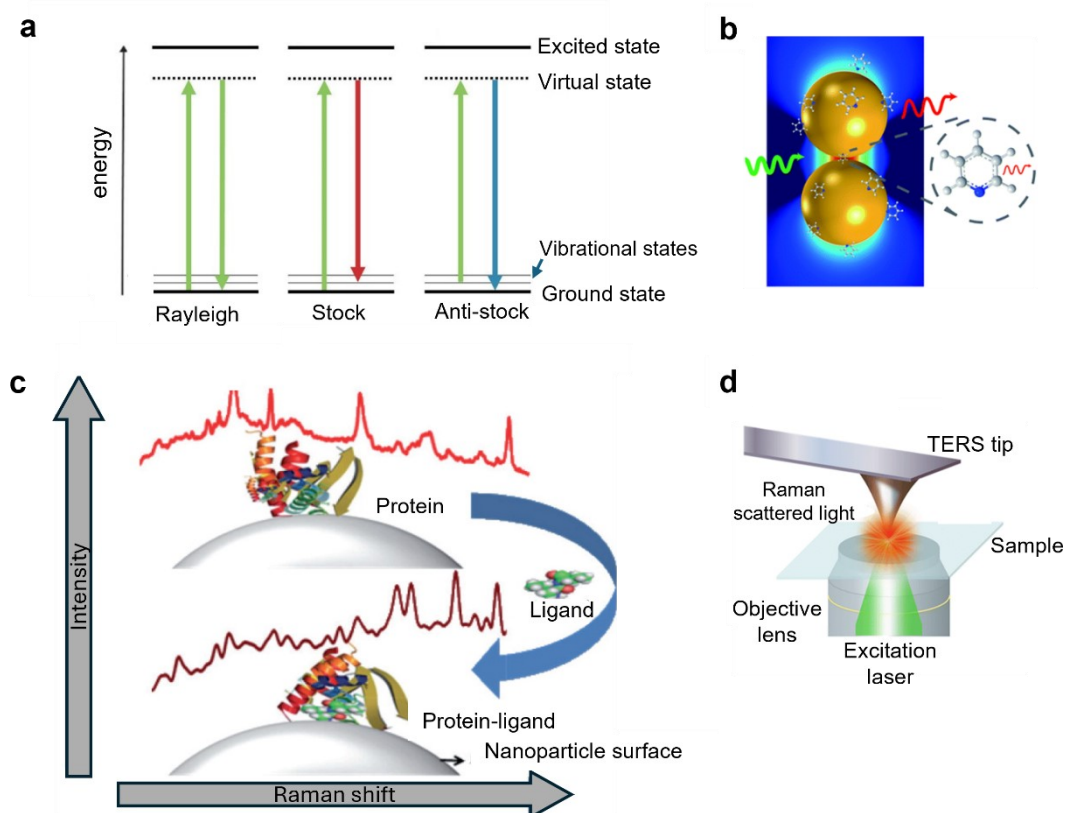


Figure 2.4: Illustrations of Raman scattering, SERS and TERS (a) Jablonski diagram depicting Rayleigh, Stokes Raman and anti-Stokes Raman scattering. Reprinted with permission from (157). Copyright 2016 Authors. Royal Society (b) Schematic demonstrating SERS principle as incident light (green) induces surface plasmon resonance and the resulting Raman signal (red). Reproduced from (158) (CC BY 3.0). (c) A cartoon representation of protein-ligand detection by SERS shows that changes in the SERS spectrum indicate ligand binding to a protein, forming a protein-ligand complex. This binding causes structural changes in the protein, altering amino acid orientations and disrupting hydrogen bonds, resulting in spectral changes that signify the complex formation. Reprinted from (159) (CC BY 2.0). (d) Illustration of an AFM-TERS setup displaying surface plasmon resonance (red) at the tip apex which enhances the electromagnetic field resulting in Raman signal enhancement. Reprinted from (160) (CC BY 4.0).

Due to the inherently weak nature of inelastic scattering, its use in single molecule or protein studies was impractical until the advent of surface-enhanced Raman spectroscopy (SERS), which utilises surface plasmon resonance (161) (**Figure 2.4b**). SERS can enhance the Raman signal by a factor of 10^{10} - 10^{11} , enabling it to be used for single molecule/protein studies which has been shown using silver colloidal nanoparticles (162). Additionally, SERS can be used to monitor ligand binding to

proteins, as illustrated in **Figure 2.4c**. When a ligand binds to a protein, the Raman signal shifts, indicating this interaction (159).

Since the introduction of SERS, several studies have been conducted on single molecules with good Raman signals such as dyes or bulk proteins (163). However, few focus on single protein information despite single protein detection having been achieved since 1999, with single haemoglobin molecules being detected between silver particles (164). It is only within the past 5-10 years that single protein studies have been conducted using SERS, including the oxygenation state and orientations of the porphyrin ring being shown (162). Silver nanoparticles modified with aluminium and iodide ions have been used as substrates in SERS to detect catalase, α and β casein, insulin, acidic BSA, myoglobin and lysozyme (162). Gold SERS substrates have been used to detect BSA at the single-molecule level by linking it with Traut's Reagent, which binds to BSA and facilitates its attachment to the gold surface (165). Using gold nanostructures to amplify the SERS signal through plasmonic effects, a DNA origami scaffold was incorporated to capture streptavidin and thrombin at specific anchoring sites (166).

Despite the potential of SERS for single protein studies, various limitations prevent its widespread use for such experiments. One significant limitation is the lack of reproducibility in experiments, primarily due to constraints in nanofabrication (167). Even a slight variation of just a few nanometres in the size of nanostructures can significantly alter the signal enhancement (167). Additionally, differences in sample preparation and even instrument conditions can result in variations in the output data (158). Furthermore, substrate fragility, cost, and reusability also limit the practical implementation of SERS for single molecule studies (168). Moreover, the enhancement factor is insufficient to study various proteins as it has been implied that the enhancement limit has already been reached and so many proteins may be unable to be observed properly using SERS (169,170). Finally, single molecule SERS typically relies on random adsorption to detect single molecules, which is both inefficient and potentially very time-consuming (171).

As SERS arose as a new type of Raman spectroscopy, a subfield of SERS has also arisen, termed TERS for tip-enhanced Raman spectroscopy which combines atomic force microscopy (AFM) with SERS (**Figure 2.4d**). The Zenobi group first reported it

in 2000 when a silverside AFM tip was used to observe the Raman spectrum of the dye brilliant cresyl blue (172). Advances in this technique allowed the same group to observe the signal of brilliant cresyl blue at the single-molecule level (173). Similarly, to SERS, despite having been shown to detect single molecules over a decade ago, TERS has been used to study only a few proteins in this manner. These are the haem proteins cytochrome c and haemoglobin (174), as well as the interaction of single haemoglobin and human serum albumin to form hybrid protein nanofibers (175,176).

TERS has several advantages over SERS such as higher spatial resolution due to the AFM tip and greater sensitivity. However, the limitations of nanofabrication discussed previously still hold true as well as the increased complexity of the technique further limits reproducibility for single molecule studies (158). The relatively low number of single protein studies in the field with Raman may be attributed to the mentioned limitations and, in the case of proteins, due to sample homogeneity as proteins are complex molecules with constantly changing conformations, orientations and adsorption interactions that will affect Raman signals. Until these limitations are addressed, the use of SERS and TERS for single protein studies will likely remain scarce.

2.4 iSCAT and mass photometry

Interferometric scattering microscopy (iSCAT) involves imaging the interference caused between a reference light field and the light scattering caused by the sample (177,178).

The first interference-based method was demonstrated in 1991, as the basis for iSCAT to study microtubule dynamics (179). Following this work, the term iSCAT was officially coined in 2009 in a study on the dynamics of virus diffusion on lipid bilayers, which introduced novel concepts that progressed the field significantly (180). These lead to improving the signal-to-noise ratio by detecting more photons through increased exposure time or laser power. Additionally, an image subtraction scheme was used could eliminate residual scattering caused by uneven substrates and false reflections within the optical setup (180).

The main applications for iSCAT are defined in its super-resolution and label-free nature to image biological processes such as microtubules (179,181), lipid

nanodomains and exciton migration in conditions closer to their native states *in vivo* (182,183). Also, it has been shown that iSCAT can precisely detect and track single molecules, and viruses (180,184). Adding to these studies, iSCAT has also been used in single protein sensing and tracking, with recent examples including sensing single fibrinogen (185), carcinoembryonic antigen (185), immunoglobulin gamma-1, bovine serum albumin (185), small heat shock protein 16.5 from *Methanocaldococcus janaschii* (186) and myosin-5a (187). The detection limits of iSCAT have also been pushed using machine learning, with single low molecular weight proteins such as protein G (21kDa), Skp protein from *E. coli* and human interleukin-8 (9 kDa) being detected (188).

Although iSCAT has proven effective as a label-free single protein sensing technique, its widespread use is still limited by its sensitivity. Detecting and measuring particles only a few nanometres in size requires careful filtering methods to distinguish between signals from the sample and background noise. Indeed, it is the signal-to-noise ratio that limits this approach to investigating single proteins and as such, improvements in the factors that affect this ratio will be pivotal such as the intensity of the illumination, and the scattering cross-section of the sample (178).

A notable offset of iSCAT is mass photometry (originally termed interferometric scattering mass spectrometry), which is a technique that provides a quantitative means of measuring the molecular mass of individual molecules (**Figure 2.5a**) (189). When molecules in solution settle on a microscope coverslip, mass photometry measures the local contrast shift resulting from this. The signal in mass photometry scales linearly with particle volume (190). This allows for the accurate measurement of protein molecular weight as proteins have been found to have normal distributions in both specific volume and refractive index (191). Mass photometry has also been used to determine the dissociation constants of various protein-protein interactions at the single molecule level, such as between human α -thrombin and anti-human thrombin antibody (192), as well as the type III Fc γ receptor CD16a and protein A to immunoglobulin gamma (193). The tracking and mass measurement of the multi-domain GTPase dynamin-1 on a lipid bilayer has also been shown using a variation of mass photometry termed dynamic mass photometry (194). This was done by using a

different background removal approach to images of dynamin-1 diffusing on the lipid bilayer (194).

Mass photometry has also been used to understand various other areas of protein dynamics including polymerisation (195), oligomerisation and aggregation (195). For example, the polymerisation of dynamin, a protein involved in clathrin-mediated endocytosis was studied using mass photometry and dynamic mass photometry to understand the dynamics and regulatory mechanisms behind this process (195). Mass photometry can also determine biomolecular abundance. It was applied to analyse monomers and domain-exchanged dimers of the HIV-1 neutralising antibody 2G12, yielding mass distributions with major bands at 147 kDa and 291 kDa across varying monomer/dimer ratios (**Figure 2.5b**) (196). It also examined interactions between protein A and human/bovine immunoglobulin gamma (193), the HIV inhibitor BanLec with the HIV envelope protein (197), and human and plant 2-cysteine peroxiredoxins (198). The oligomerisation and aggregation of the protein tau have also been quantified using mass photometry (199) Also, we recently demonstrated the disassembly of single ferritin molecules and their intermediate oligomers at acidic pH 2 using optical nanotweezers and mass photometry as complementary single molecule approaches which we will discuss in detail in Chapter 5 (55).

Mass photometry is not without its problems, as the technique has the detection limit ranging from 30 kDa to 5 MDa (200) Additionally, although the resolution of mass photometry has been noted to be up to 20kDa at full-width half maximum and 2% mass accuracy, the resolution is impacted by several factors (189). These include photon shot noise, sample purity, relative concentrations of species in the sample, and the mass range of the particles of interest (189). Due to these factors, resolution will be adversely affected by samples that have high heterogeneity or contamination within a small mass window of interest (190,201). Another limitation is sample concentration as mass photometry works best when the sample molecules are well separated on the measurement surface. Experiments can be performed with sample concentrations within 100 pM to 100 nM, with an optimal concentration range of 5 – 20 nM for biomolecules (193). These concentration limits make mass photometry a less suitable technique for studying weak biomolecular interactions where higher sample concentrations are required. Despite these limitations, mass photometry has shown

itself to be a versatile single-molecule technique that can provide quantitative information on various proteins.

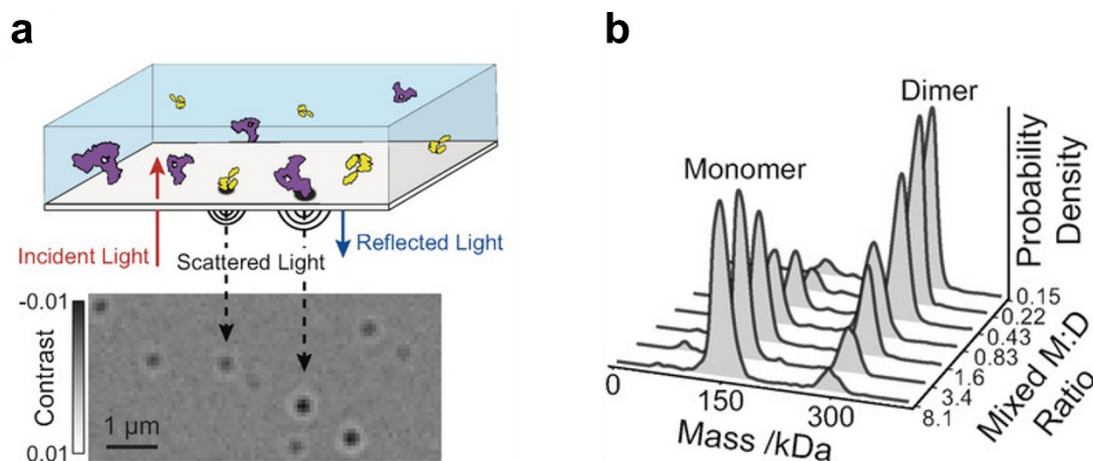


Figure 2.5: Illustrations of the principles behind mass photometry (a) Principle of mass photometry. Single-molecule identification without labels through tracking the interference of reflected and scattered light resulting from individual protein landing events at a glass-water interface over time. (b) Mass distribution of 2G12 proteins in their monomeric and dimeric states using mass photometry. Reprinted from (196). Copyright 2020 The Authors. Published by Wiley-VCH Verlag GmbH & Co.

2.5 Optical tweezers

Optical tweezers are versatile tools used to probe various biophysical phenomena by applying force or torque to individual particles. While detection relies on force, the optical components are crucial for trapping and manipulating the particles. I included this technique in this chapter to highlight its importance in assisting researchers in better understanding protein structures and dynamics.

In Chapter 1, we introduced this technique and its fundamentals, pioneered by Ashkin et al. (202,203). Here, we will discuss its applications in biological science and single molecule analysis. The versatility of this method in life science and biology has been demonstrated through the optical trapping, manipulation, and characterisation of

atoms (204,205), micron and sub-micron particles (206,207), as well as DNA (208,209), viruses (210,211), bacteria (212), cells (213,214), and proteins (215). In this approach, the particle of interest must first be attached to two supports, such as polystyrene or silica beads by molecular handles, such as DNA handles (**Figure 2.6**).

So far, several molecular handles have been used to immobilise particle of interest in optical tweezer setups. Stangner et al. (216), used antibody-antigen interactions to study receptor-ligand interactions at a single-molecule level. Specifically, they analysed the binding specificity and unbinding characteristics of the monoclonal antibody HPT-101 to synthetic tau-peptides with phosphorylation at Thr231 and Ser235, including both double-phosphorylated and monophosphorylated forms. Bechtluft et al. (217) used engineered biotin-streptavidin (STV) links to study the role of chaperones in the protein folding pathway of maltose-binding protein (MBP). Using this technique, they revealed that SecB binds to the molten globule-like state of MBP, preventing stable core formation while allowing external α helices to fold. Cecconi et al. (218) utilised a chemical crosslinking technique to join DNA handles using covalent disulfide bonds involving cysteine residues. It is noteworthy that each tethering method offers advantages and disadvantages. For example, antibody-antigen interactions, such as Myc-AntiMyc and Dig-AntiDig, are sensitive to pH, temperature, and buffer conditions, limiting the kind of research that may be explored (218).

The initial comprehensive study of protein folding using optical tweezers focused on ribonuclease H (RNase H) (219). Native RNase H unfolds at around 19 pN, but it also has a weaker state unfolding at about 5.5 pN. Optical tweezers allowed direct observation of an intermediate folding state, revealing crucial insights into the protein folding pathway that are difficult to obtain with other ensemble techniques (219). Optical tweezers were also used to determine the equilibrium state of proteins, relating to their folded and unfolded states. Shank et al. (220) determined the unfolding free energy of T4 lysozyme, which consists of two subdomains. Selectively unfolding the smaller subdomain revealed a free energy of 12.3 kcal/mol, similar to the 14.1 kcal/mol obtained by chemically denaturing the entire protein, indicating highly cooperative unfolding.

Optical tweezers are generally effective in trapping objects ranging from 100 nm to 10 μ m in size. However, they face limitations with transparent dielectric particles

smaller than 100 nm due to Brownian motion, and larger objects due to difficulties in generating strong enough forces to overcome inertia and gravity. Additionally, the need for tethering in optical tweezers experiments can impact the dynamics of the protein and molecule being studied (221).

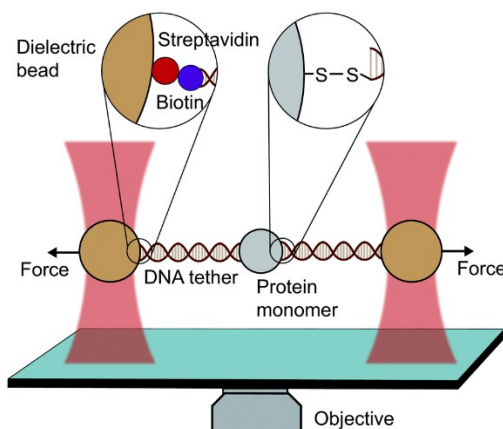


Figure 2.6: Schematic of immobilising a monomeric protein using optical tweezers setup where a protein monomer is attached to dielectric beads via DNA tethers and biotin-streptavidin interactions, allowing forces to be applied to the beads for studying protein folding and interactions. Reprinted from (222) (CC BY 3.0).

2.6 Whispering-gallery mode for single molecule sensing

Whispering gallery mode sensors is an optical single-molecule detection approach that uses resonance frequency measurements to detect biomolecules such as DNAs and proteins with high sensitivity and precision in identifying and quantifying molecular interactions. When light is directed into a dielectric microstructure like a glass microsphere, resonant wavelength become trapped and circulates internally (223). This creates optical resonance, known as whispering gallery modes (WGMs), due to constructive interference between the microcavity and its surroundings. The light waves extend through an evanescent field, slightly beyond the microbead or cavity (224). Dielectric WGM sensors, like glass micro-beads (**Figure 2.7a**), offer real-time detection of multiple proteins even in complex environments (225). The Q factor in WGMs reflects the resonance's sharpness, indicating strong light interaction with specific frequencies (**Figure 2.7b-right inset**). In terms of WGM geometries, there are several classes including two- and three-dimensional shapes. Microrings (226) and microdisks (227) are two common 2D shapes, and microspheres (228), microfibers

(229), microbottles (230), microbubbles (231) and microtoroids (232) are the popular 3D geometries which have been successfully used for WGM microresonators. As illustrated in **Figure 2.7b** (right inset), the properties of microcavities lead to the concentration of the light on the surface with a high Q factor (223).

These sensors enable the determination of analyte concentrations in biosensing applications through ensemble measurements. Achieving single-molecule detection with WGM sensors requires significantly enhancing detection scheme sensitivity. (233) When WGM is paired with plasmonic metal nanoparticles, there is potential method for detecting single proteins (233–237).

Exciting WGMs trigger plasmon resonance in plasmonic nanostructures like nanorods, enhancing detection sensitivity for single molecules and atomic ions. When a molecule enters the plasmonic hotspot, it leads to agitation in the light path and subsequently shifts in WGM's optical resonance in the order of femtometres (238). This facilitates a label-free single molecule sensing to study biomolecules in physiological solutions with microsecond time resolution (**Figure 2.7c**) (239). This includes detectable phenomena like the open and closed states of enzymes (240,241) as shown in **Figure 2.7b**. For instance, Kim et al. (242) detected polymerase/DNA interactions linked to enzymatic activity at the single-molecule level using plasmonic nanorods resonantly coupled to whispering gallery modes in microcavities. They showed that, at various temperatures, a direct relationship exists between the sensor signal and the enzymatic activity of three different polymerase types.

WGM sensors typically operate with temporal resolutions ranging from milliseconds to seconds, constrained by factors like laser frequency modulation bandwidth (225). However, frequency-locking techniques aligning the probing frequency with the WGM's resonant frequency can enhance this resolution, allowing for a time resolution of up to 1.2 milliseconds (243). In terms of the advantages of this technique, it is noteworthy that the resonator not only functions throughout a wide optical spectrum and is robust in various kinds of environmental conditions, but it also has a high-quality factor and small-volume modes (244).

While the sensitivity and integration potential of this label-free approach have attracted interest in the sensing field, several significant challenges need to be

resolved. These challenges include enhancing surface modification processes to optimize sensor performance, reducing background interference to improve the signal-to-noise ratio, and extending the lifespan of sensing components like optical cavities and photodetectors. Additionally, efforts focus on broadening the range of detectable substances for simultaneous analysis of multiple analytes and improving the detection capability of WGM sensors to the single-molecule level (223). To fully utilise the potential of label-free sensing techniques in a variety of applications, these obstacles must be overcome.

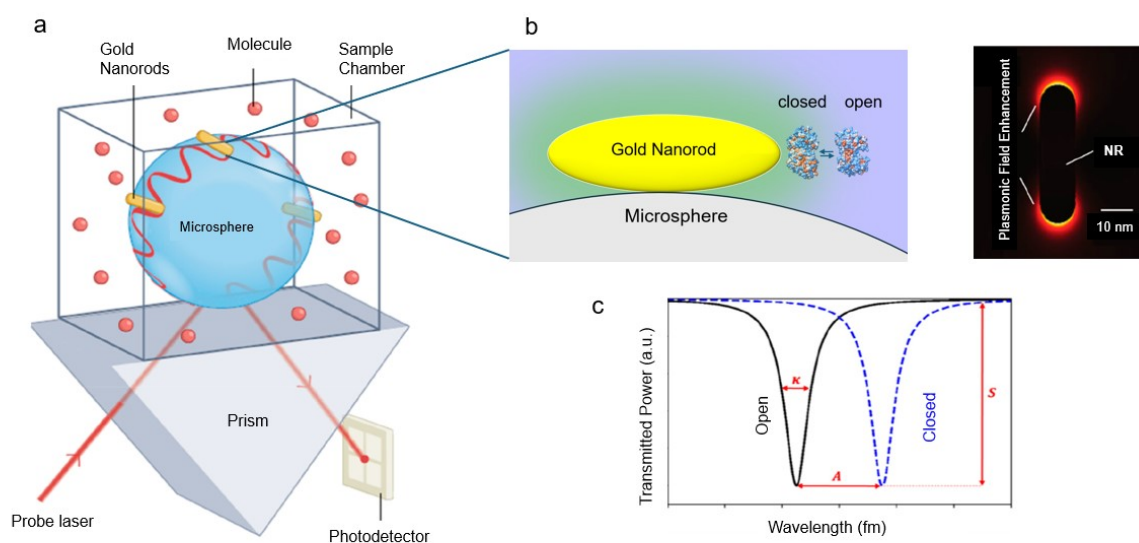


Figure 2.7: Illustration of WGM sensors for single protein detection (a) A WGM sensor featuring a glass microsphere with plasmonic enhancement from gold nanorods. Reprinted with permission from (50). Copyright 2021 Springer Nature (CC-BY-NC-ND) (b) Enzymatic activity at the gold nanorod tip, shown with 3-phosphoglycerate kinase (3PGK) in both open (PDB: 2xe6) and closed (PDB: 2ybe) conformations, indicating substrate binding and activation. Right panel: Electric field distribution highlighting enhancements at the gold nanorod tips. Reprinted from (240). Copyright 2024 The Authors (CC-BY 4.0). (c) Transmission spectrum wavelength shifts reveal changes in molecular polarisability near the nanorod tip, illustrated by the enzyme's conformational change. Signal amplitude (A), related to wavelength shift ($\Delta\lambda$), can be determined. Additional parameters like full-width-at-half-maximum (κ) and coupling percentage (S) are crucial for understanding WGM intensities. Reprinted from (240). Copyright 2024 The Authors (CC-BY 4.0).

2.7 Plasmonic optical tweezer approach

The interaction between light and nanostructures has enabled label-free single-molecule optical detection (187). The application of metallic nanostructures specifically noble metals excels in significantly amplifying optical field intensity (245). This is explained by the plasmon polariton resonance that arises when external electromagnetic fields are coupled to the collective oscillations of conduction (246–248). Researchers proposed in 1997 that a laser beam shining on a sharp metal edge could produce enough optical potential to trap nanoparticles (249). This pioneering work demonstrated that nanoparticles could be effectively trapped near the metal tip's surface. Under conditions such as specific shapes, sizes, or arrangements, the geometric features of the metal structure led to charge concentrations that create highly localised evanescent fields (249,250). These fields, which decay exponentially away from the surface, produce strong gradient forces that enhance the precision of optical trapping. The localised surface plasmons contribute to increased confinement and trapping potential depth, stabilising the trapping process at the nanometre scale (249,250).

Okamoto et al. (251), two years later, introduced a plasmonic optical tweezer (POT). They used an opaque metallic film with a sub-wavelength aperture, allowing confined light to transmit through the aperture. A decade later, the field of POT made great progress by effectively trapping tiny particles using low-incident laser energies, building upon these foundational experiments (250,252,253) This progress paved the way for precise nanoparticle trapping and manipulation at the nanometre scale.

To understand how POT holds an object, we must first explain some fundamental principles behind this technology, such as plasmonic forces and the self-induced back action (SIBA) effect.

2.7.1 Fundamental theories of plasmonic forces

There are two primary types of optical forces in plasmonic trapping: gradient forces and scattering forces (254). As discussed in Chapter 1, the scattering force results from momentum exchange between light and objects due to changes in the light's propagation path. In contrast, the gradient force, which arises from the field energy

intensity gradient, is crucial for forming optical traps by overcoming the scattering force (249,254).

The Lorentz force, which is dependent on the electric field E , and magnetic field B , is the first force we use to characterise the forces generated by plasmonic fields on an object (254)

$$\vec{f} = \rho\vec{E} + \vec{J} \times \vec{B} \quad 2-1$$

Where J is the total current density and ρ is the total charge per unit volume.

Using the inhomogeneous Maxwell's equations, the force can be expressed as: (254)

$$\vec{f} = \varepsilon[(\nabla \cdot \vec{E})\vec{E} - \vec{E} \times (\nabla \times \vec{E})] + 1/\mu[(\nabla \cdot \vec{B})\vec{B} - \vec{B} \times (\nabla \times \vec{B})] - \varepsilon\partial(\vec{E} \times \vec{B})/\partial t \quad 2-2$$

In a static electromagnetic field, the time-averaged force is given by: (254)

$$\langle \vec{F} \rangle = \int ST \cdot n dS \quad 2-3$$

where T is Maxwell's stress tensor, n is the unit normal to the integral area ds , and ε and μ are the relative permittivity and permeability of the surrounding medium. In both LSP and SPP fields, plasmonic structures of any size or form can be analysed using the Maxwell stress tensor (MST) approach, which provides the total electromagnetic force acting on the particle (250).

To make computations simpler for objects much smaller than the wavelength of light, a dipolar approximation might be utilised: (254)

$$\langle F \rangle = \frac{1}{2} \sum_i \text{Re} (p_i * \nabla E_i) \quad 2-4$$

Where $p = \alpha_0 E$ is the induced dipole moment, and α_0 is the polarisability. The local electric field E is considered through the mutual interactions between the particle and the surrounding media, resulting in an effective polarisability tensor.

The plasmonic trapping potential energy U exerted on a particle located at r_0 can be calculated by integrating the force: (254)

$$U_{(r_0)} = - \int_{r_0}^{\infty} \vec{F} \cdot dt \quad 2-5$$

The potential well must be deep enough to contain the particle for stable trapping, usually around $10 k_B T$ (where k_B is the Boltzmann constant and T is the absolute temperature). This requires higher light field intensity to counteract Brownian motion, which is influenced by particle size and temperature.

2.7.2 Self-induced back action (SIBA) trapping fundamental

The crucial aspect of SIBA trapping is the fact that the particle itself actively participates in the trapping event by altering the optical transmission signal through a sub-wavelength hole (255). The SIBA effect typically results from the resonance's sensitivity to variations in the local refractive index (72,255). In particular, Bethe's initial research focused on the diffraction of light passing through a tiny circular aperture in an indefinitely thin and pure metallic layer (256). According to Bethe, there is extremely little light transmission via a hole in a metal film that is smaller than the wavelength of light (256). However, the high optical transmission effect, which shows that a specific design of the nanoaperture structures can boost light transmission through a sub-wavelength hole, raised doubt on his predictions. When light passes through a hole in a real metallic film, it couples into SPP modes that penetrate the hole walls, effectively enlarging the hole. As a result, stronger coupling between SPP modes on opposing sides of the hole results in a higher effective refractive index and an increased optical transmission signal (72). Similarly, introducing a particle into a nanohole increases the effective refractive index, and redshifts the transmission signal (51). The SIBA force, which points in the direction of the equilibrium position, slows the photon momentum whenever it drops as it leaves the trap. This makes it possible to lower the incident laser intensity to levels that correspond to a potential depth of the order of $k_B T$ (51,72). As seen in **Figure 2.8a–c**, during high-energy events, the SIBA system adjusts the trapping potential depth to maintain the object inside the trap (73).

This results in an increased transmission signal proportional to the particle's refractive index (51,257). Consequently, the nanohole structure enables effective optical trapping by employing the strong fourth power scaling of Bethe's theory, which describes light transmission through subwavelength apertures and predicts that the transmitted power scales with the fourth power of the hole's diameter. This surpasses the third power polarisability dependence of Rayleigh scattering, leading to enhanced

trapping efficiency. The advantage of the SIBA configuration over other plasmonic optical trapping (POT) approaches is that it does not require plasmon resonance (51,257).

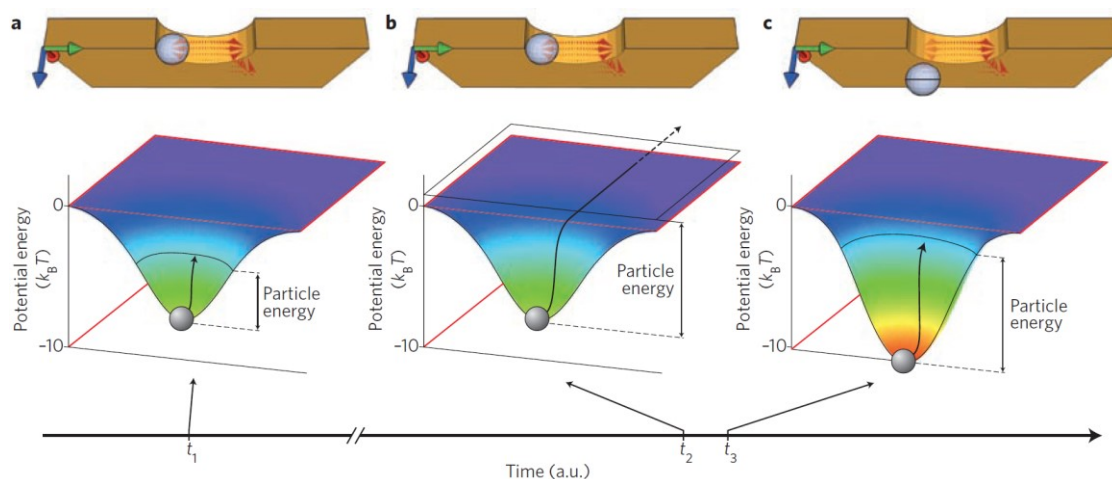


Figure 2.8: Self-Induced Back Action (SIBA) effect on the trapping potential energy of a dielectric particle in a nanoaperture-based plasmonic trap. (a) At time t_1 , the particle is positioned within the aperture with moderate kinetic energy. (b) The particle may exit the aperture in the high-energy event at time t_2 . (c) When the particle begins to leave the hole at time t_3 , the potential depth enhances because of the SIBA force to keep the particle trapped. Reprinted with permission from (51) Copyright 2011, Springer Nature Limited.

2.7.3 Aperture-based optical trapping of a single protein using plasmonic optical tweezers

Aperture-based nanostructures have emerged as powerful tools for plasmonic optical tweezers, enabling precise manipulation of small dielectric objects (81,186,258). Nanoaperture structures for single-molecule detection have demonstrated effectiveness by naturally limiting background radiation (81). Also, the aperture, surrounded by a continuous metal film, facilitates the thermal conductivity of the structure. The inherent simplicity of an aperture makes it easy to use in a nanofluidic channel without introducing additional complexities (81). A broad range of nanostructures have been employed by plasmonic nanotweezers. Particularly circular

apertures (257,258), coaxial apertures (259,260), bow-tie apertures (261), split-ring resonators (262), and rectangular apertures (263), have been used in this category. Still, most applications in the field of single protein reported to use plasmonic nano apertures like DNH structures (**Figure 2.9**) (54,55,82,264–267).

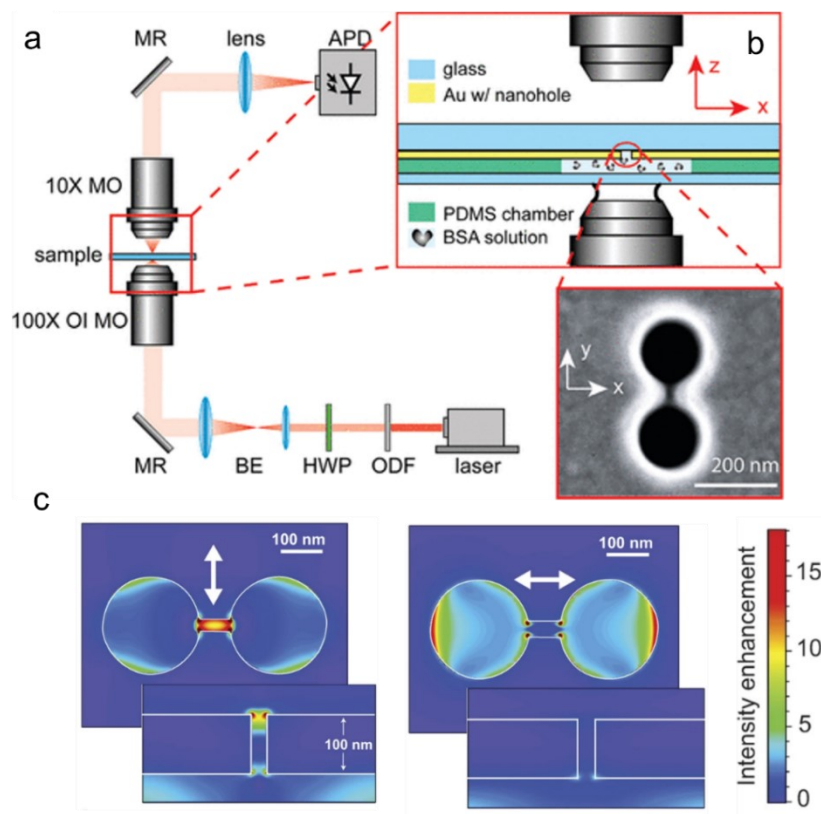


Figure 2.9: Double nanohole (DNH) structure used in the optical tweezer setup and its field enhancements models (a) Illustration of a trapping experiment using DNH structures. Laser passes through an optical density filter (ODF), half-wave plate (HWP), and beam expander (BE) and are guided by mirrors (MR). The expanded beam then enters the objective (100X-oil immersion), illuminating the sample. The light is collected by a condenser lens (10 X) and detected by an avalanche photodiode (APD). Reprinted from (56). Copyright 2012, American Chemical Society (b) An enlargement of the red rectangle in (a), details the sample in the microfluidic chamber, the setup of the oil immersion microscope objective, and the condenser microscope objective. An SEM image of the DNH sample placed in the flow system is shown on the bottom. (c) Local intensity enhancement (linear scale) for a DNH with a 25 nm gap when the polarisation of the 633 nm beam is perpendicular to the line connecting the centres of the holes (left) and when it is parallel to the line connecting the centres of the holes (right). Reprinted from (267). Copyright 2015, The Author(s) (CC BY 4.0).

Plasmonic nanoapertures exhibit highly sensitive optical responses influenced by geometric design, irradiation field parameters such as polarisation, wavelength of excitation, dielectric properties of the cavity content, and morphological fluctuations (51,76). Therefore, nanostructure design and the gap size of the cavity are critical in modifying near- and far-field characteristics (81). When two metallic nanostructures are brought closer together in dimmer nanocavities, the near-field of system is enhanced due to the coupling of the electric fields. Surface plasmons, such as SPPs and LSPs, play key roles in particle manipulation (75). LSPs, widely employed for optical manipulation and other applications, excel in enhancing local electromagnetic fields due to their nanostructure performance (51,75,76). In other words, the nanostructure, when exposed to light, acts like a nano lens. This lens can focus light much more intensely than a high-quality microscope objective lens (51) **Figure 2.9 a-b** shows the implementation of plasmonic optical tweezers using DNH structure. Generally, in the plasmonic optical trapping technique, the sample is illuminated with a laser via a 100x or 60x microscope objective. Transmitted light is collected by an objective and measured using a silicon-based avalanche photodiode (APD) (54,56,268). The field enhancement is geometry and polarisation dependant as mentioned earlier. LSP hotspots will be excited when the SPR matches the illuminated light to these nanocavities. **Figure 2.9c** demonstrates that the field enhancement around DNH structures is shaped with hotspots in the edges. These hotspots provide high gradient force for trapping the dielectric objects like proteins (56,267).

When a biomolecule, like a protein, with a higher refractive index (~ 1.8) than its surroundings (water ~ 1.3), is introduced between the tips of the double-nanohole, it exerts an electrical influence on the region with enhanced local field strength. This process significantly boosts light transmission, a phenomenon known as dielectric loading (**Figure 2.10a**) (82). Using this plasmonic nanotweezer setup with DNH, Pang and Gordon (56) trapped Bovine serum albumin (BSA) with a hydrodynamic size of 3.4 nm. The change in the transmission signal (the steps shown in **Figure 2.10a**) relates to the unfolding of the BSA and confirms the unfolding of BSA by changing the pH and incident laser power. In a subsequent study within the same research group, Al Balushi et al. (269). examined the interaction between streptavidin and a 20 nm biotin-coated polystyrene particle at a single molecule level (**Figure 2.10b**). Furthermore, Ying et al. (268). conducted a thorough investigation into substrate and temperature

effects on protein conformation (**Figure 2.10c**). They correlated transmission levels with the protein shape, which is related to its refractive index. This correlation facilitates precise monitoring of thermal unfolding, refolding, and enzymatic cycles with exceptional time resolution. For example, they trapped a single calmodulin, a calcium-binding protein which has a molecular weight of 16.7 kDa and interrogated the thermal unfolding and refolding trajectory (**Figure 2.10c**).

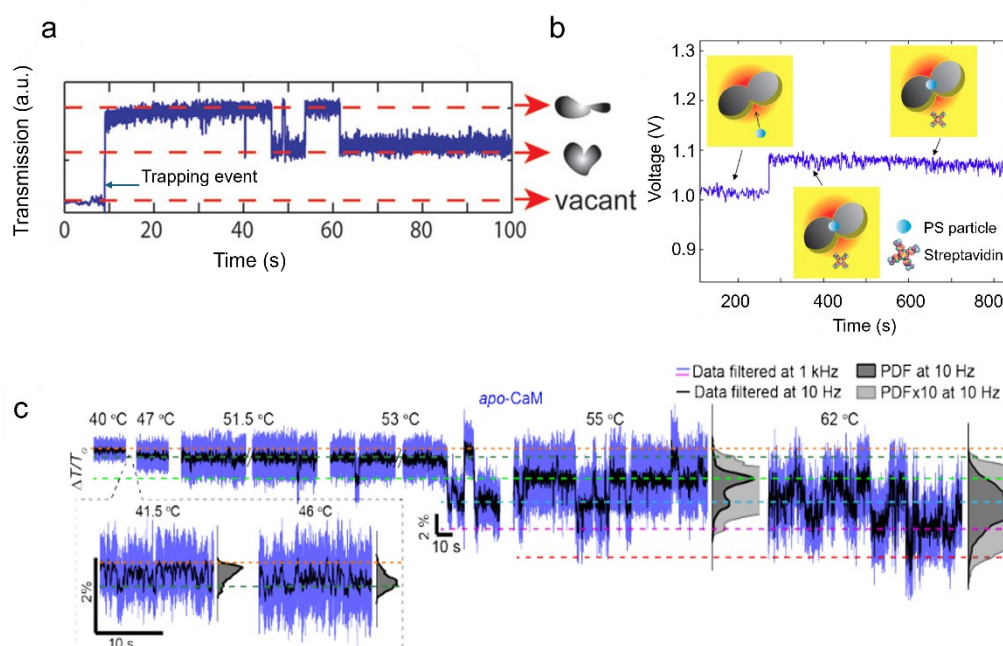


Figure 2.10: Using DNH Structures for single protein characterisation (a) Trapping single BSA molecule and monitoring its conformational changes. Reprinted from (56). Copyright 2012, American Chemical Society (b) Tracking binding between streptavidin and a 20 nm biotin-coated polystyrene particle at the single-molecule level. Reprinted with permission from (269). Copyright 2019 Optical Society of America (c) Investigating the effect of temperature on calmodulin unfolding at the single-molecule level. Adopted from Ying et al. (268).

One important factor influencing the quality and duration of trapping small particles, such as proteins, is the trapping stiffness. The research group led by Reuven Gordon reported on the modelling of trapping stiffness for nanospheres in a double nanohole (DNH) trap. Given that thermal fluctuations and drag forces can influence the motion

of a particle in an optical trap, this behaviour can be effectively modelled using an overdamped Langevin equation: (259)

$$\frac{dx(t)}{dt} = -\frac{\kappa}{\gamma}x(t) + \left(\frac{2K_B T}{\gamma}\right)^{1/2} \kappa \zeta(t) \quad 2-6$$

Where $x(t)$ represents the particle transposition from the equilibrium situation, κ denotes the stiffness of the optical trap, γ is the Stokes drag coefficient, and $\zeta(t)$ is the white noise. By using this equation, the time constant τ (s), which is derived from the exponential decay fit of the autocorrelation curve, is related to the trap stiffness κ as follows:

$$\tau = \gamma/\kappa \quad 2-7$$

Additionally, in nanohole structures wall effects happen that can cause drag forces for nanospheres trapped at the DNH aperture. Taking these boundary effects into account, the Stokes drag coefficient is estimated using Faxén's law:

$$\gamma = \frac{6\pi\eta r_0}{\left[1 - \frac{9}{12}\left(\frac{r_0}{h}\right) + \frac{1}{8}\left(\frac{r_0}{h}\right)^3 - \frac{45}{256}\left(\frac{r_0}{h}\right)^4 - \frac{1}{16}\left(\frac{r_0}{h}\right)^5\right]} \quad 2-8$$

The important factors to consider in this regard include the numerical aperture of the objective lens, molecule size, laser power, and trapping efficiency (75). Ying et al. (268) demonstrated a key correlation between trapping stiffness and protein size. High molecular weight proteins such as Glycogen Phosphorylase (GPb, 180 kDa), exhibit notably greater trapping stiffness when compared to smaller proteins like Calmodulin (CaM - 17 kDa).

2.7.4 Integrating plasmonic effects into other single-molecule techniques

Combining the plasmonic method with additional single-molecule methods allows for more flexibility than just depending on the plasmonic effect alone. Researchers make use of the surface-enhanced fluorescent effect, in which fluorescence characteristics are improved by plasmonic nanostructures altering the surrounding environment of fluorophores, resulting in more effective light emission (270). The use of plasmonic

nanostructures to increase fluorescence brightness has been studied extensively through the last two decades (271–276). One limitation of surface-enhanced fluorescence is the potential for background signals and the binding of fluorophores to metallic surfaces. In response, Punj et al. (277) addressed this challenge by introducing an innovative solution — an antenna-in-box plasmonic nanostructure (**Figure 2.11a**). This design enhances fluorescence signals by concentrating the electromagnetic field around the fluorescent molecules, while minimising unspecific binding and background noise by confining the active sensing area to a localised region near the nanostructure. This precise targeting ensures that only biomolecules near the plasmonic hotspot contribute to the signal, reducing interference from non-target molecules. The study examined diverse biomolecules, including the notable analysis of cellular protein Annexin 5b and protein A.

Plasmonic technology can be integrated into solid-state nanopore structures (278). Plasmonic "hotspots" concentrate and boost optical excitation at the nanoscale, enabling the detection of surface-analyte interactions (278). Belkin et al. (278), showed that plasmonic effects were utilised to study DNA by employing plasmonic nanopores, which controlled the translocation of DNA molecules through a solid-state nanopore, allowing for precise manipulation and detection. They integrated this method with SERS to obtain vibrational spectra, providing information about nucleotide composition and enabling potential DNA sequencing (**Figure 2.11b**).

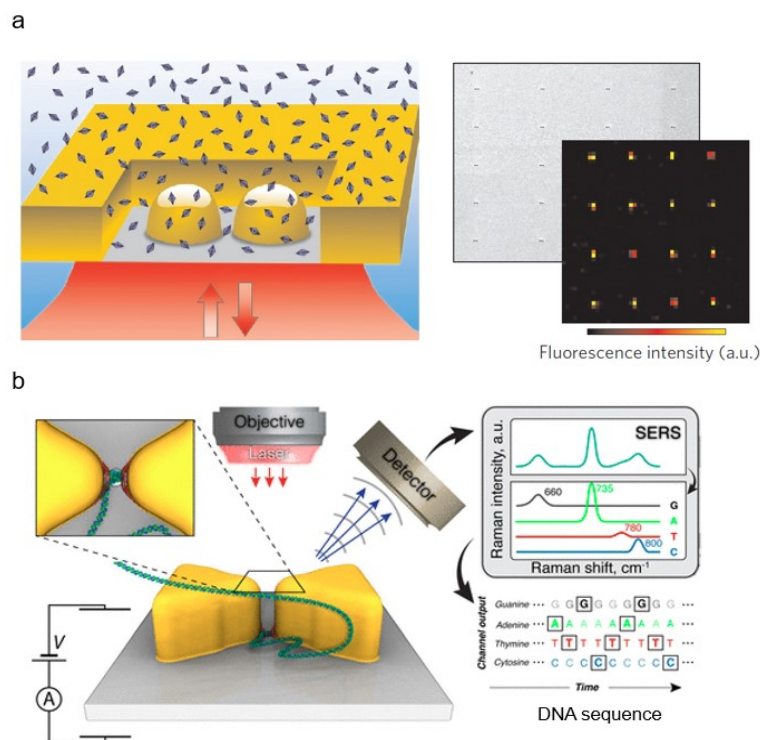


Figure 2.11: Integrating plasmonic approaches with other single molecule techniques (a) The schematic shows a dimer gap antenna within a rectangular aperture. The device is milled in a gold film (yellow) on a glass substrate (grey) and covered by a micromolar fluorescent molecule solution (light blue). SEM and confocal images display an array of nanoantennas with a 5 mm pitch. Reprinted with permission from (277). Copyright 2013, Springer Nature Limited (b) Using a plasmonic nanopore device for DNA trapping and sequencing. A bowtie gold structure on a membrane with a nanopore, submerged in an electrolyte solution, focuses a laser beam onto hot spots near the nanopore. DNA moves through the nanopore driven by a transmembrane potential, with the laser's optical field applying a restraining force. Switching the laser on and off moves DNA stepwise, while surface-enhanced Raman scattering (SERS) identifies the nucleotide sequence. Reprinted from (278). Copyright 2015 American Chemical Society (CC BY-NC 4.0).

2.8 Conclusions and future of light-based single-molecule approaches

Existing single-molecule research methods will be used to provide quicker, easier, and less invasive tests to comprehend the dynamics, structure, and behaviour of biological systems (5). In this chapter, we emphasised some of the most current research in the field of single-molecule methods and their significance to applications ranging from

diagnostics to basic biology. Most single protein studies rely on labelled approaches like smFRET, which provide important data on protein dynamics, conformational changes, and intermolecular interactions at the single-molecule level. However, photobleaching or blinking of fluorescent tags can affect the dynamics of the protein being studied (46). In recent decades, label-free single-molecule approaches have emerged as powerful techniques for studying small proteins (187). Single-molecule assays based on nanoplasmonics, nanophotonics, scattering-based detection techniques, iSCAT, and mass photometry are now possible thanks to developments in optical imaging and nanofabrication (52). Despite iSCAT being a label-free approach, it requires a relatively long integration time, which averages out dynamic information. Mass photometry which is based on iSCAT offers high precision in mass measurement but also has limitations in capturing rapid kinetic processes. There is still room for improvement in these approaches. For example, in the case of the nanoplasmonic approach, a major drawback is heating generation due to ohmic loss, which can affect the dynamics and behaviour of the protein being studied (79). To address this, dielectric nanostructures are promising as they have low absorption in the near-infrared and visible ranges, like silicon structures (279). However, the fabrication of these structures is complicated, and their field enhancement is lower compared to plasmonic ones. This challenge can be addressed through the efficient design of nanostructures, which involves optimising their geometry and material properties to maximise performance.

Additionally, employing complementary single-molecule techniques provides a comprehensive understanding of various aspects of the subject under study, ensuring reliability. For instance, in a recent investigation of single proteins, Zhou et al. (280) used SERS with a sub-10 nm aperture at the tip of a quartz nanopipette. This technique distinguished between the oxygenated and deoxygenated states of haemoglobin, revealing the compact (T) and elongated (R) states. Furthermore, plasmonic nanotweezers were effective in studying the oxygenation states of haemoglobin, capturing the transition from the T state to the slightly flattened R state. This technique offered more precise insights into the transition kinetics between these two states by using DNH optical nanotweezers, which provided enhanced sensitivity (268). Notably, smFRET experiments were not feasible due to fluorescence quenching by haemoglobin's heme groups (281). Also, in Chapter 5 of this thesis, we used two

single-molecule approaches to characterise the fragmentation of protein and its subunits during disassembly at pH 2, which will be explained in detail.

Chapter 3: Methodology

3.1 Introduction

In this chapter, I will outline the methodology used to monitor protein samples with plasmonic optical tweezers. This includes the fabrication of nanostructures, the simulation of field enhancements, the characterisation of proteins, and the instruments used in these processes. Additionally, I will discuss the data analysis methods employed in this thesis. Some parts of the approach presented here have been published in references (54) and (55).

3.2 Nanofabrication

Nanofabrication is the engineering of structures on the nanometre scale (0.1-100 nm). These structures underpin the development of complex, multi-functional systems across diverse fields such as life sciences, electronics, materials science, energy technology, and nanomedicine. Nanofabrication includes a range of techniques, which are primarily divided into "top-down" and "bottom-up" approaches (282). Top-down methods involve the patterning and etching of materials to achieve the desired nanostructures, while bottom-up techniques such as co-precipitation aim to build structures from smaller units, often through chemical synthesis or self-assembly processes that replicate natural phenomena (283).

Among different top-down nanofabrication techniques, notable methods include electron beam lithography (EBL) (284), focused ion beam (FIB) (285), photolithography (286), and nanoimprint lithography (287). Electron beam lithography is well-established for applications in silicon-based technologies due to its high resolution and precision. Focused ion beam (FIB) offers the advantage of versatile processing capabilities, including milling, implantation, ion-induced deposition, and ion-assisted etching.

In this thesis, I will outline the nanofabrication techniques, that I used during my PhD, including EBL and FIB.

3.2.1 Electron beam lithography

During my PhD, I first learned and used EBL for fabricating nanostructures. To start, I used silicon nanostructures which have induced the interest of many scientific researchers for a wide range of future applications in electronics, photonics, sensing devices, and biological applications (288,289). Silicon is an interesting material for nanostructures because it is abundant, it has well-developed fabrication techniques, and it is compatible with modern semiconductor technologies (290).

Silicon nanostructures can be made through various processes, including chemical vapour deposition (CVD) (291), molecular beam epitaxy (MBE) (291), and etching methods—of which reactive ion etching (RIE) is commonly used (292). These methods allow one to control the size, shape, and composition of the nanostructures with high precision, which is very important to tailor their properties for specific applications (289,290,292). Among these approaches, electron beam lithography is a highly versatile and precise technique to fabricate silicon nanostructures (284,293). It involves a focused beam of electrons, which are made to inscribe patterns onto a substrate of silicon coated with resist. The uncovered parts of the resist are then developed to reveal underlying silicon, which may be etched or otherwise treated further to develop the desired nanostructures (293).

Of more importance, EBL is highly valued for its capability of producing features with resolutions down to a few nanometres, which makes it the leading research and development technique in the field of nanoscale devices (284). In the following sections, we will discuss EBL techniques employed during my PhD research to fabricate silicon dielectric samples. The EBL process consists of multiple stages (284), each of which will be elaborated upon in the subsequent sections.

It is worth noting that some of this work was conducted in the clean rooms at the University of Nottingham using the NanoBeam nB5 EBL system. For the first time at Nottingham Trent University, we performed nanofabrication using the Nability NPGS, a system installed on a scanning electron microscope that enables precise pattern generation for nanolithography. Additionally, for the deposition of thin films and hard masks, we used the Edwards E306 thermal evaporation machine in the clean room of the Department of Physics at the University of Nottingham, as well as a homemade thermal evaporation machine at MTIF at Nottingham Trent University.

3.2.1.1 Plasma-enhanced chemical vapour deposition (PECVD) for silicon films

Among the various thin-film deposition techniques, plasma-enhanced chemical vapor deposition (PECVD) is one of the most widely used, particularly in the semiconductor industry (294). The PECVD process involves activating chemical reactions with plasma for depositing a film and thereby permits a lower temperature than other CVD processes. It is therefore most useful for depositing films over substrates that cannot tolerate high temperatures (295). The process involves introducing precursor gases into the applied electric field of a reactor, thus ionising them and yielding a plasma. Subsequently, the reactive species present in the plasma react on the surface of the substrate, leading to film growth on the substrate surface (295). PECVD provides controlled film composition and thickness, hence it is used for a variety of applications, such as photoluminescence applications (294). In this thesis, the equipment used for the PECVD process to deposit a-Si (amorphous Si) is the Corial D250 PECVD machine.

The first step is to thoroughly clean the cover glass substrate to ensure proper adhesion and high film quality. This is achieved through sequential rinsing: first with deionised water to remove particulate contaminants, then with ethanol to eliminate organic residues. After cleaning, nitrogen gas is used to rinse and further dry the substrates, preventing water spots or residues that could cause defects during deposition. A contaminant-free surface is essential for producing high-quality a-Si films with uniform thickness and fewer defects. The substrates are then placed in the reaction chamber of the Corial PECVD machine, followed by evacuating the chamber to the base pressure to remove any residual gases that could disrupt the deposition process.

The deposition process commences by introducing the silane (SiH_4) as precursor gas into the chamber, together with a carrier gas like argon or hydrogen, which helps to maintain plasma stability (**Figure 3.1**) (294). The plasma is generated from a silane dissociation by the radio frequency (RF) power source. Reactions follow in a complex way that leads to silicon depositing on the substrate, forming an amorphous silicon layer. Very high control of both the gas flow rates and the chamber pressure conditions, as well as the RF power and substrate temperature, must be ensured to achieve the

desired film properties. The resulting a-Si layer is then ready for further processing and characterisation as part of the silicon dielectric samples.

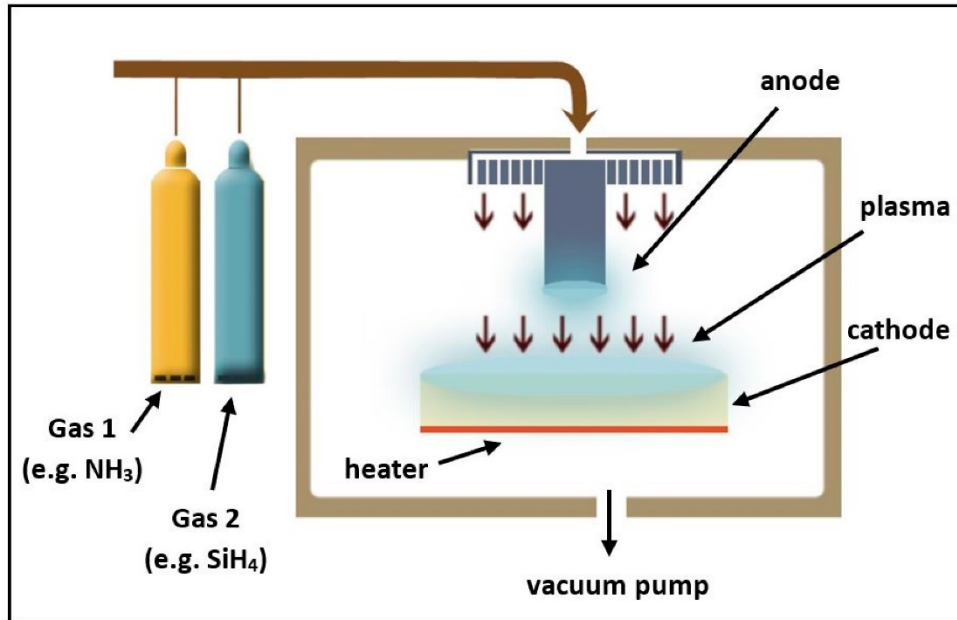


Figure 3.1: Schematic of PECVD reactor for depositing thin films. Reprinted from (294). Copyright 2021(CC BY 4.0.). Licensee MDPI, Basel, Switzerland.

In this thesis, the deposition of amorphous silicon (a-Si) on glass using PECVD with a Corial D250 reactor is described as follows: First, the glass substrate was thoroughly cleaned. The substrate was then loaded into the PECVD chamber, which was evacuated to the desired base pressure. A 10% SiH₄/He mixture was introduced at a flow rate of 500 sccm. The substrate temperature was set to 275°C, and the chamber pressure was adjusted to 1,000 mTorr. RF power of 250 W was applied to generate the plasma. Under these conditions, the deposition rate was approximately 90 nm/min. This method ensured a uniform a-Si layer; however, the specifics could vary based on factors such as precursor gas purity, reactor configuration, substrate cleanliness, and system calibration. For assessing the thickness of the sample, ellipsometry (Accurion EP4) was used, a technique that measures the change in polarisation as light reflects or transmits through the sample to determine the thickness of the deposited film (296).

3.2.1.2 Electron resist coating

Before exposure to the electron beam using EBL, an important step in nanofabrication is electron-resist coating. There are two types of electron resist: positive and negative. Positive electron resist becomes soluble in the developer solution where it is exposed to the electron beam, allowing those areas to be removed. Negative electron-resist becomes insoluble in the developer solution where it is exposed, protecting those areas. We used PMMA A4 950K, which is a positive electron resist. The PMMA was spin-coated onto the silicon surface and then baked on a hot plate at 180°C for 2 minutes. As we intended to use it as an electron beam resist, a conductive layer of AR-PC 5090 was spin-coated and then baked at 100°C for 1 minute.

3.2.1.3 Writing the patterns via Electron beam

This work uses EBL for maskless patterning of devices within electron resist layers. EBL functions as a direct-write nanofabrication technique, primarily using electron beams based on the scanning electron microscope (SEM) system (297). It overcomes the diffraction limits of optical lithography by using the shorter wavelength of high-energy electrons (284).

The system employs a 30 kV or 80 kV (depending on the EBL machine) electron source to generate electrons that are subsequently focused onto the sample (electron resist) using an electrostatic column (284,298). This column offers precise control over the beam's position, enabling direct writing of the desired pattern onto the sample. Beam current regulation is achieved via an aperture, which concurrently controls the beam's spot size (297).

Resolution in EBL is not just limited by the spot size of the focused beam. Instead, the dominant factor is the interaction between the electrons and the resist layer (297).

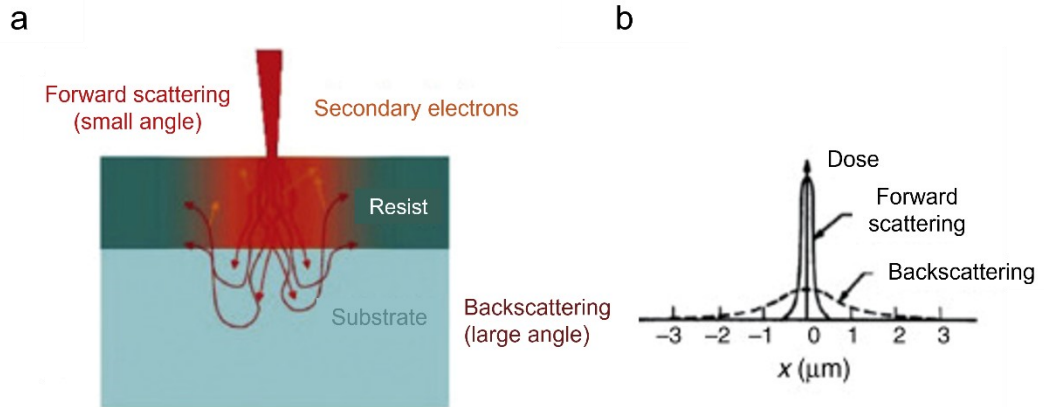


Figure 3.2: Electron scattering and dose distribution in electron resist. (a) Forward and backscattering of the electron beam within both the resist and substrate layers. (b) Spatial distribution of the electron beam dose within the resist, influenced by the forward and backscattering phenomena. Reprinted with permission from (299). Copyright 2020 Elsevier Inc.

Exposure of the resist primarily arises from incident electrons and the secondary electrons produced upon electron incident on the sample. While forward scattering from incident electrons is minimal at the high energies used in EBL, the scattering of secondary electrons is significantly more pronounced, leading to a broadening of the exposed regions (**Figure 3.2a, b**) (298).

Another factor influencing resolution is the writing step size, which denotes the distance the beam travels before exposing the next point (298). Larger step sizes translate to fewer exposed spots, thereby compromising resolution but expediting the writing process (298). The proximity effect is another noteworthy phenomenon, where electron scattering results in a higher dose being delivered to the pattern's centre compared to its edges. However, this effect is mitigated by advances in the EBL software (298).

The beam dose, quantified in $\mu\text{C}/\text{cm}^2$, represents the quantity of electrons per unit area to which the sample is exposed (284) Users define the dose by tailoring the beam current and exposure time to achieve the desired outcome (284). Material properties of the sample also influence the dose (294). Insufficient dose yields underexposed features, preventing complete removal of the resist layer during development. Conversely, an excessive dose can destroy delicate features as the surrounding resist becomes accidentally exposed alongside the intended area. Optimisation of the dose

is essential for each new sample, considering the specific material and feature size (284,294).

Figure 3.3 illustrates the steps involved in the nanofabrication of silicon using the EBL technique. The process begins with the deposition of a thin film of silicon by PECVD, followed by spin coating of PMMA on the sample. After beam exposure, the samples are developed in IPA. The next step involves applying a hard mask, such as chromium or aluminium. In our case, we used a thermal evaporation system to deposit a chromium mask. Following this, the samples are placed in acetone for the lift-off process. After the lift-off step, the samples proceed to the etching stage.

3.2.1.4 Dry etching of samples

Dry etching techniques, such as Reactive Ion Etching (RIE) and Inductively Coupled Plasma (ICP) RIE, are essential for making semiconductor and optical nanostructures (300). RIE is known for its ability to etch vertical profiles with high precision, which is crucial for creating the detailed features needed in very-large-scale integration (VLSI) circuits (54,300). This method uses plasma to generate reactive ions that selectively etch the target materials, giving us a lot of control over the etching process. This precision makes RIE particularly suitable for applications where accurate pattern transfer and control over the etch profile are critical (301).

ICP-RIE, an advanced form of RIE, provides additional benefits by allowing independent control of ion density and ion energy (302). This is done by using an inductively coupled plasma source along with the traditional RF power. For applications requiring high-throughput processing and superior surface morphology, ICP-RIE is particularly helpful because of its independent control, which leads to greater etch rates and smoother etched surfaces. For instance, ICP-RIE is more appropriate for producing complicated nanostructures that require exact control over surface smoothness and etching depth, whereas RIE is ideal for obtaining detailed pattern transfer (303).

In this work, we employed RIE to etch our silicon nanostructures using the Corial 200IL Dry Etcher. The process involves placing the sample in a vacuum chamber, introducing etching gases (typically a mixture of SF₆ and O₂), and applying an RF power source to generate plasma. This plasma creates reactive ions and radicals which are accelerated towards the silicon substrate, facilitating anisotropic etching. For our

etching parameters, we maintained a chamber pressure of 5 mTorr, an SF₆ flow rate of 25 sccm, and an RF power of 100 W. The resulting etch rate was approximately 1.6 nm/sec, although it was initially slower due to the presence of an oxide layer, which etches at a slower rate.

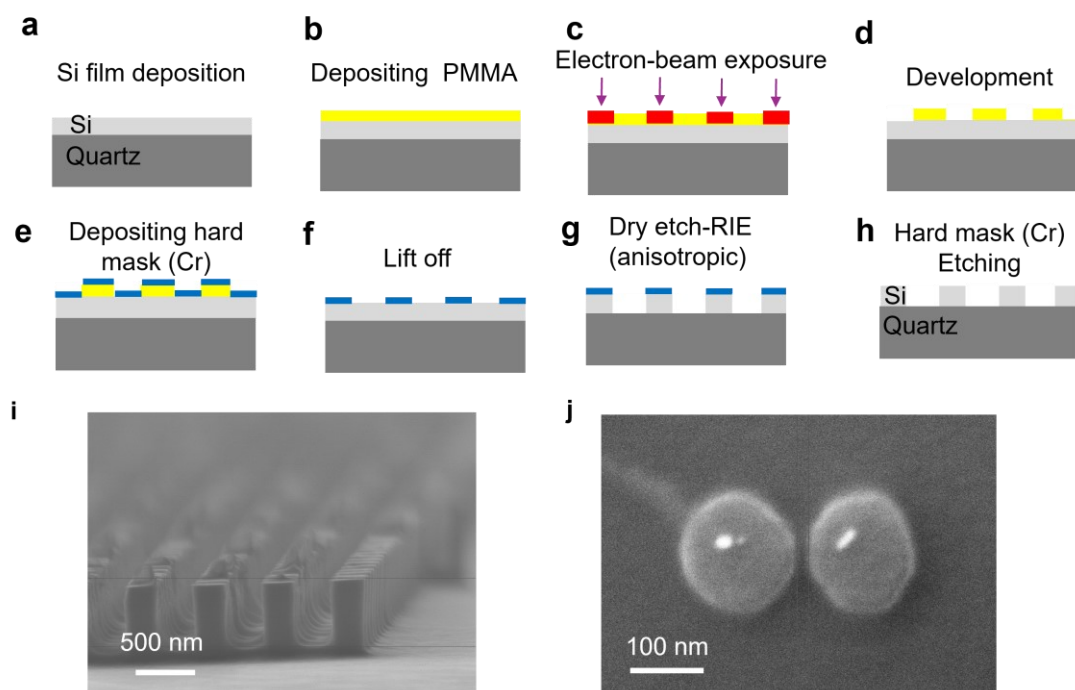


Figure 3.3: Schematic representation of the EBL nanofabrication process. (a) First, the substrate is deposited by a silicon thin film (b) A resist layer (PMMA) is spin-coated onto the silicon surface. (c) Electron beam lithography is used to pattern the resist. Red areas show the exposed parts (d) Development of the resist reveals the patterned areas. (e) A hard mask layer of chromium is deposited using thermal evaporation. (f) The lift-off process removes the resist, leaving the chromium mask. (g) The sample undergoes dry etching to transfer the pattern into the silicon layer. (h) The final pattern after hard mask removal. (i) SEM image cross-view of the silicon structure patterns (cross-view to make assess the etching quality). (j) SEM image of silicon dimer sample with a gap size of 25 nm which can be useful for single-molecule trapping purposes.

3.2.2 Focused ion beam (FIB)

FIB technology is an exceptionally versatile tool for nanoscale fabrication, modification, and characterisation of materials (285). FIB system consists of three primary components: an ion source, an ion optical system for precise beam focusing, and a scanning unit that enables controlled movement of the ion beam (285). The most used ion source is gallium, known for its high ion current and ability to produce a fine beam. However, other ion sources are also employed, each offering unique characteristics for specialised applications (304). These include gallium (Ga): the most prevalent choice due to its efficiency in producing a narrow and intense ion beam suitable for high-resolution imaging and milling. argon (Ar): used for its lower mass, which can reduce damage to sensitive materials and is effective for certain types of sputtering and etching processes. germanium (Ge) which provides high resolution and is particularly useful in applications requiring precision and minimal damage to the sample. neon (Ne) which is often employed for ultra-low energy applications, where high spatial resolution and minimal surface damage are crucial (304).

The interaction between the FIB and target materials involves several key processes such as ion implantation, which introduces ions into the material to alter its properties; milling, which removes material to shape or modify surfaces; etching, which cleans or patterns surfaces; and deposition, which adds material to build up structures (304). These capabilities make FIB a valuable technique across diverse fields, including materials science, biology, and archaeology (285). In materials science, FIB is employed for tasks such as precision nanomachining, imaging of microstructures, and advanced spectroscopy. In biology, it aids in the detailed study of cellular structures and the development of nanostructures for biomedical applications (285,304,305).

The first significant use of FIB technology dates to the early 1980s when it was initially developed for semiconductor industry applications, particularly for the analysis and modification of microelectronic circuits (304). Its utility quickly expanded to other fields due to its high precision and versatility. The introduction of FIB into biophysics and materials science has allowed researchers to explore and manipulate materials at unprecedented resolutions down to a few nanometres, leading to numerous advancements in nanotechnology and related disciplines (305).

FIB technology continues to evolve, with new ion sources and enhanced system capabilities being developed to improve performance and extend applications. Modern FIB systems can now provide three-dimensional imaging and analysis, making them indispensable tools in cutting-edge research and industrial applications.

3.2.2.1 FIB for fabrication of DNH samples

The fabrication of the DNH structure in this work was based on the FIB techniques (268). This process includes the following steps:

Chemical vapour deposition (LPCVD): First, a 30 nm silicon nitride (SiN_x) layer was deposited onto 550 μm thick fused silica wafers using low-pressure chemical vapour deposition (LPCVD) at 800°C. In this process, silane (SiH₄) and ammonia (NH₃) gases were introduced into the reaction chamber under a low-pressure environment, typically ranging from 100 to 300 mTorr. The high temperature facilitated the decomposition of these gases, allowing silicon from the silane to bond with nitrogen from the ammonia, forming a uniform SiN_x layer on the wafer surface (**Figure 3.4 a**).

Electron beam evaporation: After depositing the SiN_x layer, a 5 nm titanium (Ti) adhesion layer was applied to the surface, followed by a 100 nm gold (Au) film. This process was carried out using electron beam evaporation with the Leybold Optics LAB 600H system at a substrate temperature of 190°C. The Ti layer ensures strong adhesion between the gold film and the underlying SiN_x layer, as titanium forms a good bond with both silicon nitride and gold. During the electron beam evaporation, high-energy electrons were directed at the titanium and gold targets, causing the materials to vaporise and condense as a thin, uniform film on the wafer surface (**Figure 3.4 b**). Once the deposition was complete, the silicon wafers were precisely diced into 10 mm by 10 mm chips using a Disco DAD321 dicing machine, ensuring clean and accurate edges for subsequent experimental use.

FIB for milling DNH structures: Finally, the DNH structures were fabricated in the gold layer using a focused ion beam (FIB) with the Crossbeam 550 system with a Gallium source. The sample was placed in the chamber at a tilt angle of 54 degrees to face the ion beam, with a working distance of 5 mm from the SEM detector (**Figure 3.4c**). The DNH geometry comprised two circles, each with a diameter of 160 nm and a centre-to-centre spacing of 200 nm. A rectangle measuring 3 nm by 40 nm was positioned to bridge the gap between the two circles. The FIB process was conducted

with a beam current of 1 pA and an ion beam energy of 30 kV. Dwell times were carefully optimised: 1.25 μs for the circles and 5 μs for the rectangle, to ensure precise milling. This meticulous control of parameters resulted in DNH structures with gap diameters around 20 nm and no residual gold left inside the gaps, yielding clean and well-defined DNH samples.

Figure 3.4d shows SEM images of the DNH structures in the tilted mode. The purpose of this imaging was to ensure the quality of the gap, confirm the absence of gold residue, and measure the gap size. Despite using the same recipe in the FIB, we observed some variations in the gap size, which could be attributed to surface roughness and internal FIB errors. To determine which structure provides greater field enhancement, we conducted optical field simulation analysis. This analysis was essential to identify the DNH structures with higher field enhancement, which are capable of capturing proteins for longer durations.

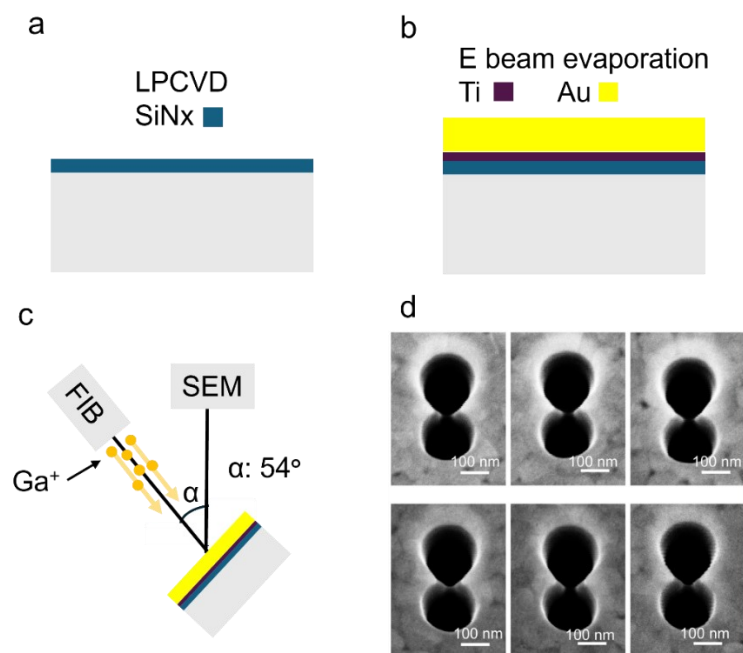


Figure 3.4: Fabrication of DNH samples using FIB. (a) Deposition of SiN_x through LPCVD on the fused silica substrate. (b) Electron beam evaporation for depositing 5 nm Ti and then 100 nm gold on the SiN_x. (c) Schematic representation of the FIB and scanning electron microscopy (SEM) setup used for fabricating and imaging the DNH structures. The gallium (Ga⁺) gold layer is deposited on the silicon nitride (SiN_x) substrate, while the SEM is used to image the resulting structures. (d) SEM images of DNH structures fabricated using the same FIB recipes mentioned in the text with a 20° tilt angle. Adapted from (54). Copyright 2023 The Authors (CC-BY 4.0)

3.3 Simulations and modelling

To analyse the impact of the DNH geometry and gap size, we simulated the optical field distribution within the DNH structure using COMSOL Multiphysics 6.1, which employs finite element simulation. We used an 852 nm laser polarised perpendicular to the line connecting the two holes. We considered a material stack with a refractive index (RI) of 1.333, surrounded by water and composed of a 100 nm Au layer, a 5 nm Ti layer, and a 30 nm SiNx layer on a fused silica substrate. Upon examining the gap geometry, we observed that it has a trapezoidal structure. This trapezoid has a base measuring 20 nm, though this value can vary between 15 and 25 nm (based on the gap size of DNH from SEM images). To account for the tapering in the DNH structures, we implemented an 'n-side truncated pyramid' structure (**Figures 3.5a-c**, upper panel) with a refractive index (RI) of 1.333, transitioning from a ~20 nm gap width at the bottom to ~45 nm at the top of the Au layer.

As mentioned in the previous section fabricating DNH due to the internal errors of FIB can give inconsistency in the gap size of the DNH **Figures 3.5a-c** display the electric field distribution for three structures with gap sizes of 15 nm, 17 nm, and 25 nm, corresponding to #2, #3, and #6, respectively. The colour bar scale indicates that field enhancement reduces as the gap size increases. Considering the hydrodynamic size of the protein under study, which in our case is Ferritin with a size of 10-12 nm, we target a DNH with a 20 nm gap size to create a narrow trapping well while allowing the protein to enter the hotspot. When the laser beam polarisation is parallel to the connecting line of the two holes, as shown in **Figure 3.5d**, there is little to no field enhancement in the DNH gap. This polarisation dependency helps distinguish the DNH from other structures.

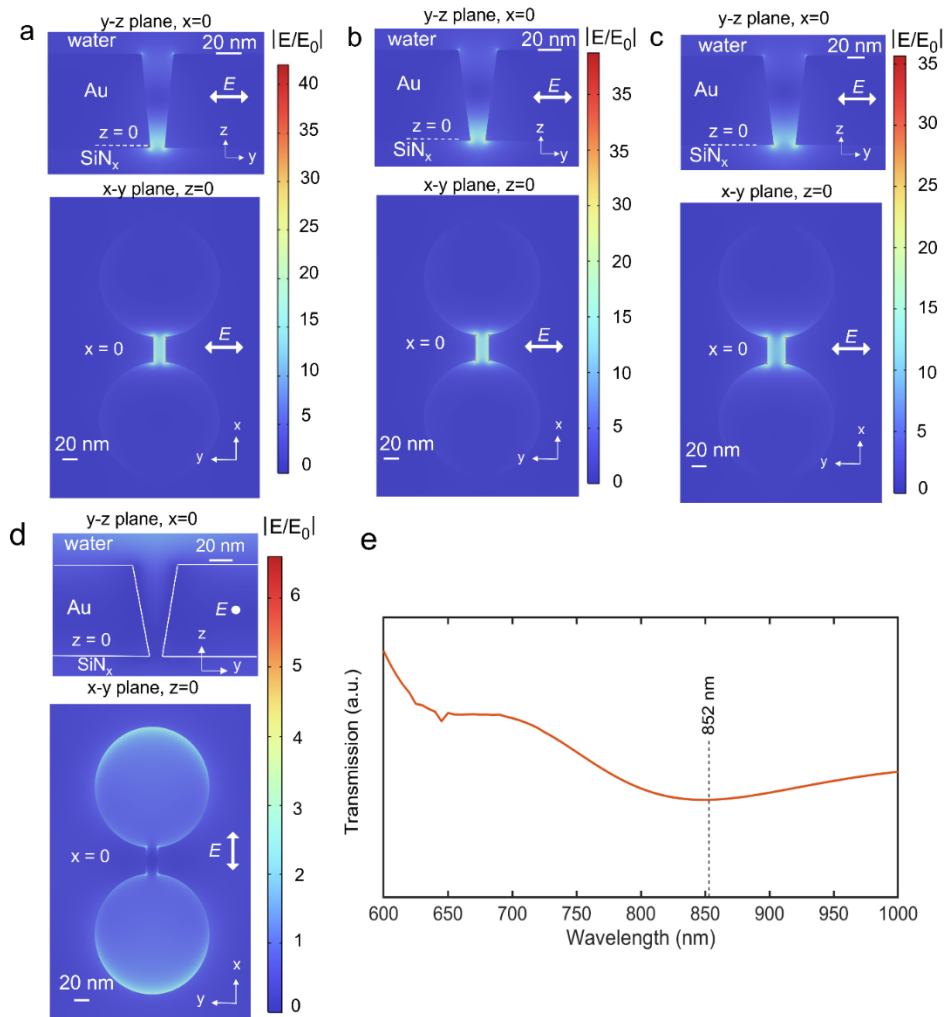


Figure 3.5: Simulated optical properties and field enhancement distribution of DNH structures. (a-c) Electric field distribution in DNH structures with gap sizes of 15 nm, 17 nm and 25 nm corresponding to a, b, and c respectively. The top panels display the electric field distribution in the y-z plane at $x = 0$, while the bottom panels show the x-y plane at $z = 0$ (gold-Ti interface). The incident laser is polarised along the y-axis. (d) The top and bottom panel descriptions are equivalent to (a-c), but the incident laser polarisation is aligned with the x-axis. (e) Simulated normalised transmission spectra of the DNH structure with a 17 nm gap size, with laser polarisation as depicted in panel b. Adapted from (54). Copyright 2023 The Authors (CC-BY 4.0)

It should be noted that the plasmonic optical trapping demonstrated here is based on SIBA trapping, which operates effectively at an off-resonance wavelength (255). The excitation laser wavelength of 852 nm is near the off-peak of the LSPR, as indicated in the transmission spectra in **Figure 3.5e** (around 700 nm). Additionally, according

to the findings of Ghorbanzadeh et al. (306), another resonance is expected in the near-infrared spectrum. Despite being at an off-resonance position, the electric field in the DNH gap remains significantly amplified. This off-resonance measurement confirms the robustness of SIBA trapping, indicating that the DNH structure can provide tightly confined field amplification within the hotspot to trap individual proteins without imposing strict limitations on the excitation wavelength.

3.4 Characterisation

In this section, I will outline the characterisation techniques employed in this thesis, beginning with the optical nanotweezer setup details. I will describe how we characterised the trapping of single ferritin molecules, including the relevant parameters and experimental conditions. Following this, I will detail additional characterisation methods used for proteins, such as size exclusion chromatography (SEC) and mass photometry (MP).

3.4.1 Optical nanotweezers setup for characterising single proteins

In this thesis, we utilised an optical tweezer setup to characterise single proteins. A crucial component of this setup is the fluidic system, which we integrated into the optical tweezers to deliver protein and buffer solution. Thus, our system comprises two main parts: the optical tweezer module and the microfluidic module, both of which will be detailed in the following sections.

3.4.1.1 Optical setup

All optical components for the experiment were procured from Thorlabs. The laser used was an 852 nm diode laser, chosen for its specific wavelength requirements. This laser was focused onto the sample using a 60× Plan Fluor objective with a numerical aperture (NA) of 0.85, provided by Nikon (Tokyo, Japan). The high magnification and numerical aperture of the objective allowed for precise focusing, achieving a spot diameter of approximately 1.2 μm . A half-wave plate, a device that shifts the polarisation of light, was used to adjust the laser polarisation. The power density at the DNH sample was carefully controlled to be 19 $\text{mW}/\mu\text{m}^2$, which was achieved from an incident laser power of 32 mW before it entered the objective lens. This controlled power density was crucial for maintaining the accuracy and consistency of the experimental measurements.

The transmitted light through the DNH structures was detected by a silicon avalanche photodiode (APD120A) from Thorlabs. An avalanche photodiode (APD) is a highly sensitive light detector that uses the photoelectric effect to convert light into an electrical current. When photons strike the APD, they generate electron-hole pairs within the semiconductor material. The diode operates at a high reverse voltage, which causes these carriers to accelerate and multiply, resulting in an avalanche of charge carriers and a larger current. This amplified current is then converted into a voltage signal. The voltage signal from the APD was captured using a data acquisition card (USB-6361, National Instruments), operating at a high sampling rate of 1 MHz. This high sampling rate was essential for accurately capturing the rapid variations in the signal. The recorded data was processed and analysed using a customised LabVIEW program, designed specifically for this experiment.

A schematic illustration of the entire optical setup, including its microfluidic component, is depicted in **Figure 3.6**. This system closely resembles the configuration shown in **Figure 2.9a** of Chapter 2, providing a consistent basis for comparison and analysis.

3.4.1.2 Fluidic system

The flow cells utilised in this study are consistent with those described in earlier reports (268). These flow cells were fabricated using a FormLab 2 printer, employing Clear V4 resin at a 50 μm resolution (Formlabs Inc., USA). A two-component silicone glue (Twinsil, Picodent, Germany) was applied to seal the samples within the flow cell, which was covered with a glass slide of 0.17 mm thickness. The DNH sample was separated from the cover slide by double-sided tape with a thickness of 50 μm (ARcare92712, Adhesive Research, Inc.), forming a fluidic channel with a volume of 3.5 μL . A 12-port valve (Mux Distrib, Elve Flow, France) and a syringe pump (Harvard Apparatus, US) regulated the flow rate and direction. To exchange the buffer after trapping a protein, a buffer was introduced into the flow chamber at a rate of 4.5 $\mu\text{L}/\text{min}$. Based on the internal diameter of the tubing in the flow control system, the buffer solution reached the flow chamber after 25 μL (or 6 minutes post-injection) had passed through the flow controller. **Figure 3.6** clearly illustrates our system, which consists of two parts: the microfluidic section and the optical section, along with the SEM image of the sample placed in the flow cell. In the next subsection, I will detail the protein buffers and solution recipes that were used throughout the fluidic system.

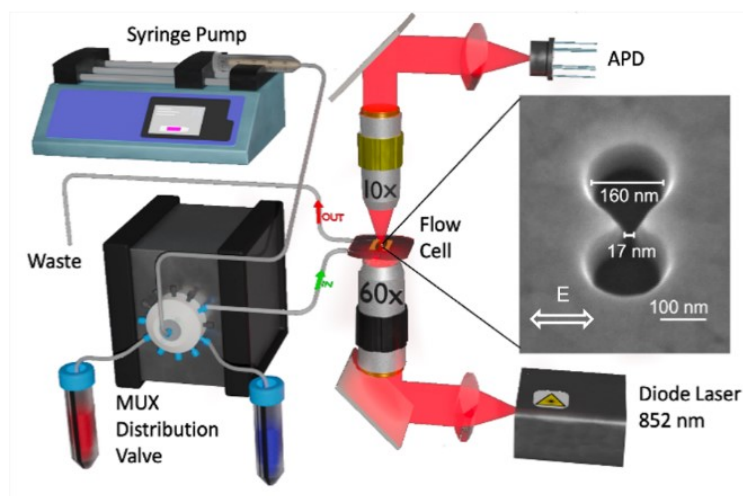


Figure 3.6: Diagram of the optical nanotweezer configuration. A syringe pump draws various buffers through a 12-port valve and subsequently injects them into the flow cell at adjustable flow rates. The flow cell houses a fused silica chip with a double-nanohole (DNH) in a thin layer of gold. A collimated laser beam with a wavelength of 852 nm is focused on the DNH using a 60 \times air objective with a numerical aperture (NA) of 0.85. The transmitted light is captured by a 10 \times objective and detected by an avalanche photodiode (APD). The right inset displays an SEM image of a DNH structure in a 100-nm gold film, taken when the stage is tilted 20 $^\circ$ for better visualisation of the gap of DNH. Adapted from (54). Copyright 2023 The Authors (CC-BY 4.0)

❖ Protein and buffer solution preparation

Below are some recipes we used in this thesis for preparing buffer solutions and proteins in buffers, as used in chapters 4 and 5.

Protein buffers: Commercially available apo-ferritin (equine spleen, A3660) and holo-ferritin (equine spleen, F4503), along with all other chemicals, were obtained from Sigma-Aldrich (UK). Trapping experiments employed either 0.5 μ M apo-ferritin or 0.5 μ M holo-ferritin in 0.1 M phosphate buffer (PB) at pH 7.4.

Fe²⁺ and Fe³⁺ buffers: For the ferrous solution (2 mM), deoxygenation of the media was achieved by initially preparing a 2 mM Na₂S₂O₄ solution in the PB buffer (307). Subsequently, ammonium iron (II) sulphate was added, and the mixture was stirred magnetically for approximately 10 minutes.

A control experiment employing PB buffer with Fe³⁺ was conducted. Here, the 2 mM ferrous solution was prepared as described above. However, to oxidise Fe²⁺ to Fe³⁺, the solution was bubbled with compressed air for at least five minutes. A clear colour change from green to yellow was observed following this step. Freshly prepared solutions were used for each experiment and were filter sterilised through a 0.22 µm pore size membrane before use.

Solutions with varying pH levels: 0.1M hydrochloric acid (HCl) (Fisher Scientific, product code 15697310) was added to a phosphate buffer (PB) at pH 7.4 to change the pH and generate solutions at different pH levels. Experiments were conducted in both a PB at pH 7.4 and a 0.1 M Glycine-HCl buffer at pH 2.0. The Glycine-HCl buffer was used as a control to examine the effects of an abrupt pH change from 7.4 to 2.0.

Ascorbic Acid-Buffer Solution: L-Ascorbic acid (A5960) was dissolved in a PB buffer at pH 7.4 to prepare solutions at three different concentrations (1 mM, 5 mM, and 10 mM). These solutions were freshly prepared before each experiment.

3.4.1.3 DNH for trapping single ferritin molecules

DNH structure used in the optical nanotweezer generates a tightly confined optical field, as illustrated by the field distribution of various DNHs in **Figure 3.5**. This field creates a sufficient gradient force to trap a single protein within a nanoscale hotspot (308). The intensity of light transmitted through the DNH structure is continuously measured in real-time by an APD. The optical signal detected by the APD provides information about the protein conformations and the trapping stiffness, which is influenced by the size of the molecule (309). Once individual proteins are trapped, a specially designed micro-channel flow system introduces different solutions to study their effects on protein conformation.

We successfully trapped both apo-ferritin and holo-ferritin using six identically fabricated double-nanohole (DNH) structures (#1–#6), all created with the same

focused ion beam (FIB) parameters. The signals from these trapping events will be analysed in detail in Chapter 4. **Figure 3.7** illustrates the trapping events for each structure, demonstrating their effectiveness in trapping both apo- and holo-ferritin.

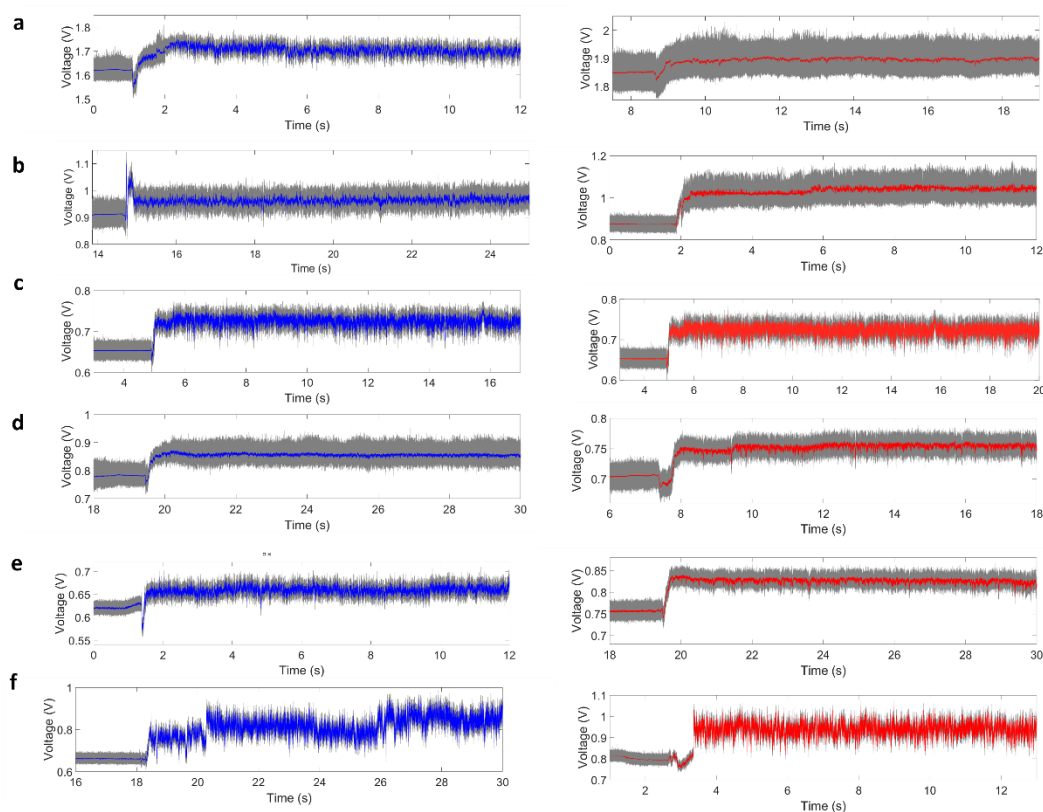


Figure 3.7 Trapping events in distinct DNH structures. Panels (a), (b), (c), (d), (e), and (f) correspond to DNH structures #1, #2, #3, #4, #5, and #6, respectively. Each panel shows the transmission signals for both trapped single apo-ferritin (blue traces) and single holo-ferritin (red traces). All data were acquired at 1 MHz (represented by the grey trace) and subsequently subjected to digital filtering with a 1 kHz cutoff frequency (blue and red traces). Adapted from (54). Copyright 2023 The Authors (CC-BY 4.0)

Figure 3.8 presents the SEM images of the six DNH structures used in this study before (only #2, #3, and #6 are available) and after the trapping experiments. Apart from surface contamination, the edges and cusps of the DNH structures became smoother, and the gap sizes increased after usage. The gap sizes for #2, #3, and #6 changed from 15, 17, and 25 nm to 28, 34, and 37 nm, respectively (indicated by black circles in **Figure 3.8b**). The boxplot in **Figure 3.8b** includes gap sizes measured from

all DNHs, including structures not used in this work but fabricated under the same conditions (SEM images in **Figure 3.4**). We observed an increase in the median gap size from 24.4 nm to 35.6 nm after two to three weeks of use, with typical laser illumination durations of 4-5 hours.

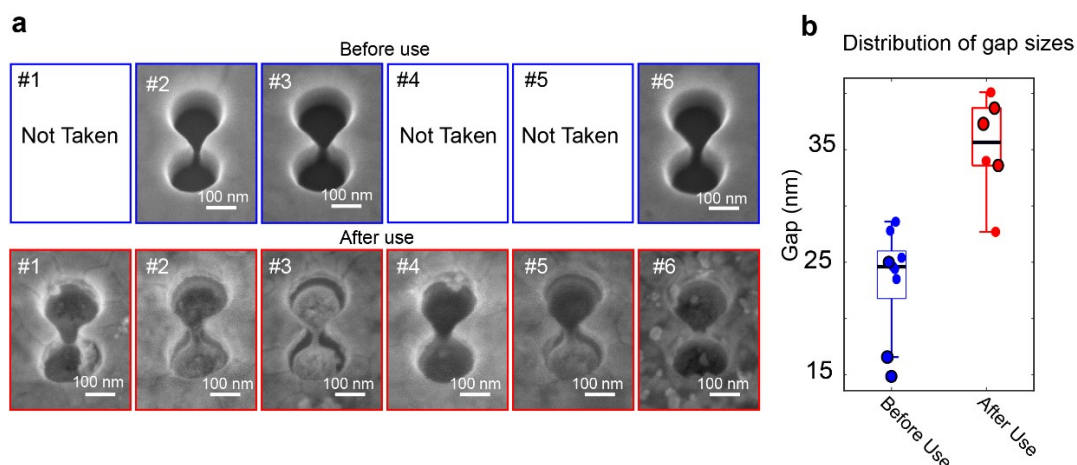


Figure 3.8: Potential DNH geometry change after trapping experiments (a) SEM images of three DNH nanostructures (#2, #3, and #6) captured before their use in trapping experiments. SEM images of DNHs #1, #4, and #5 are not included. The bottom row displays SEM images of all six DNH structures following typical illumination of the laser beam and trapping experiments for 4-5 hours. (b) Boxplot depicting the distribution of gap sizes within the DNH structures before and after experimental use. Data points marked with black circles represent the gap size measurements for DNHs #2, #3, and #6. Adapted from (54). Copyright 2023 The Authors (CC-BY 4.0)

We analysed the duration between activating the laser and successfully trapping a ferritin protein. **Figure 3.9** illustrates the waiting times for 25 trapping events from various DNHs. The histogram shows that ferritin is mostly trapped within 10-15 minutes after the laser is turned on. The time required to trap a single protein is influenced by several factors, including the characteristics of the DNH structure, the size of the protein being trapped, and the laser power used. Additionally, surface repulsion between the negatively charged protein and the negatively charged gold surface can extend the trapping duration (266).

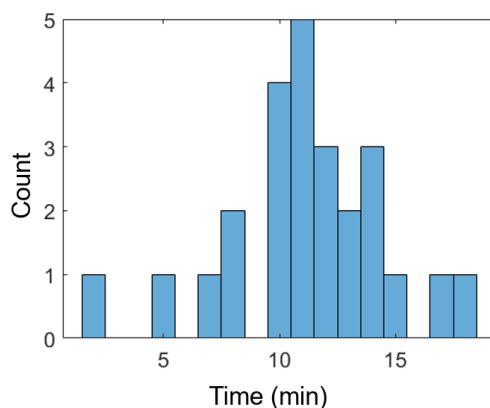


Figure 3.9: Histogram showing the waiting time to trap a ferritin protein after the laser is activated. Adapted from (54). Copyright 2023 The Authors (CC-BY 4.0)

3.4.1.4 Experimental challenges and artifacts in trapping single ferritin molecules using optical nanotweezers

Some challenges and artifacts were encountered during our optical nanotweezer trapping experiments. A significant issue was the tendency of proteins to stick to the DNH structure, which often prevented effective trapping. For instance, **Figure 3.10a** illustrates a scenario where the ferritin protein was released when the laser was turned off, but in **Figure 3.10b**, the protein remained in the trap location even after turning the laser off, indicating that it was firmly attached to the DNH. It is important to note that protein adhesion to the DNH depends on several factors, including the protein's charge, isoelectric point (pI), buffer solution, and the material of the nanostructure. To mitigate against this issue, some studies suggest coating the surface of samples with polymers such as PEG, which can reduce protein adhesion (310).

Another challenge we encountered was double trapping (**Figure 3.10c**) within the DNH, where one protein was trapped, and a second protein entered the trap. This typically occurred at higher laser powers or with higher protein concentrations (in micromolar ranges) in the buffer. When double trapping was observed, we excluded the data from our analysis to maintain accuracy. Contaminants in the chamber caused significant fluctuations in the transmission signal, as shown in **Figure 3.10d**. The SEM image in the right panel of **Figure 3.9d** shows the sample covered in contamination after use. These fluctuations made trapping difficult and compromised the analysis of signals post-trapping. To address the contamination problem, we should ensure that

the fluidic system and tubing are cleaned and washed after use with appropriate solvents like DI water and IPA. The sample should also be rinsed with DI water or IPA. These challenges emphasise the importance of careful experimental conditions and the complexities involved in nanoscale trapping experiments.

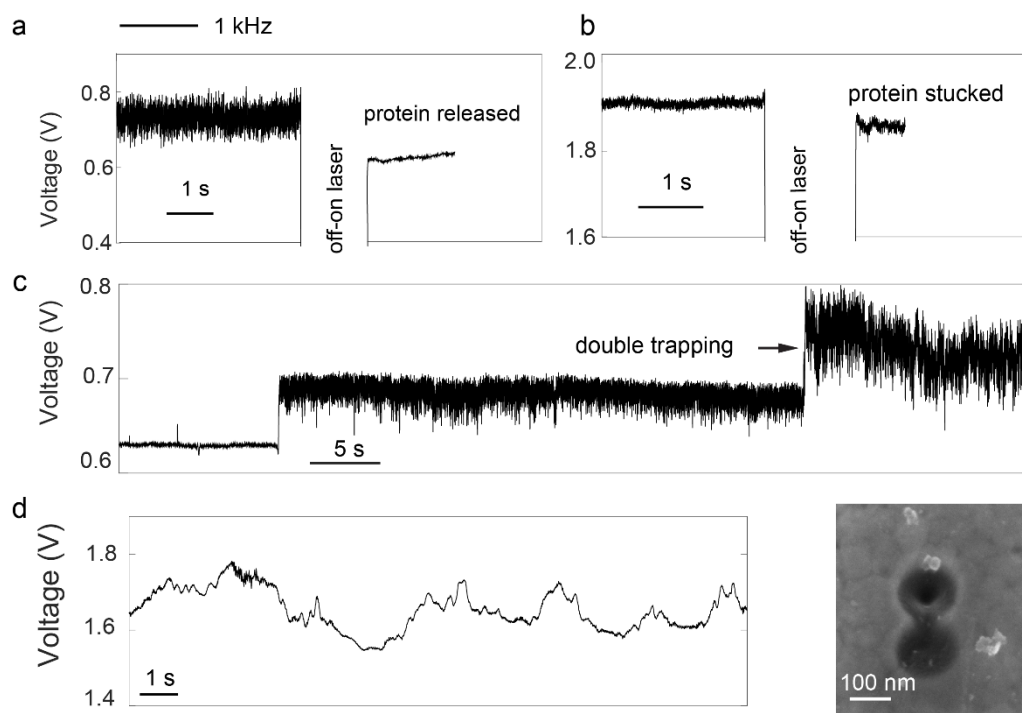


Figure 3.10: Artifacts in single ferritin trapping using optical nanotweezers. (a) Protein release after turning off the laser from the DNH structure. (b) Protein remains in the DNH structure even after the laser is turned off. (c) Double trapping event, where a second protein is trapped after the first one. (d) Transmission signal of the baseline (no protein trapped) and the effect of contamination, resulting in an unstable signal. The right inset shows an SEM image of the DNH structure after use in a contaminated chamber. Data was collected at 1 MHz and Gaussian-filtered to 1 kHz.

3.4.2 Size exclusion chromatography analysis

Size exclusion chromatography (SEC) was employed to investigate the pH-dependent disassembly of ferritin. A Superose 6 Increase 3.2/300 column facilitated the separation of molecules based on their size. Elution volumes of ferritin and its

disassembly products under various pH conditions were compared to those of commercially available standard proteins (Sigma-Aldrich) with known molecular weights including Aprotinin (6.5–22 kDa, Sigma-Aldrich A3886), Carbonic Anhydrase (29 kDa, Sigma-Aldrich C7025), Bovine Serum Albumin (66 kDa, Sigma-Aldrich A8531), Alcohol Dehydrogenase (150 kDa, Sigma-Aldrich A8656), Beta-amylase (200 kDa, Sigma-Aldrich A8781), Apo-ferritin (443 kDa, Sigma-Aldrich A3660), and Thyroglobulin (669 kDa, Sigma-Aldrich T9145) to determine their molecular sizes. Notably, all standards except ferritin were used at a consistent concentration of 0.165 mg/ml for a reliable comparison. Due to ferritin's larger size, a higher concentration of 1.65 mg/ml was used.

For accurate peak identification at pH 2, pepsin (35 kDa), a protein known for its stability under acidic conditions, was included as an internal control at a concentration of 0.4 mg/ml. The mobile phase consisted of two buffers: a neutral 10 mM phosphate buffer (PB) with 50 mM sodium chloride at physiological pH (7.4) and a more acidic 100 mM glycine-HCl buffer at pH 2. The ÄKTA-Explorer FPLC system facilitated all SEC experiments, with protein detection achieved through absorbance monitoring at 280 nm.

3.4.3 Single-molecule mass photometry (MP) analysis

Mass photometry (MP) measurements were conducted using a TwoMP instrument (Refeyn) following the manufacturer's recommended calibration procedures. Native Mark™ standard (Thermo Fisher Scientific) served as the calibration reference in T50 buffer at pH 7.4. The calibration achieved a high accuracy of 1.5%, demonstrated by a strong correlation coefficient ($R^2 = 0.99997$).

Experiments were performed on standard microscope cover glasses (Marienfeld, No. 1.5H) cleaned with a rigorous protocol: rinsing with deionised water (five times) and isopropanol (five times), followed by drying under a nitrogen gas flow. A silicon elastomer gasket (Grace Bio-Labs) defined the sample volume and prevented evaporation. Each measurement utilised a 20 μ L aliquot of ferritin solution in buffer (50 nM) introduced into a clean well formed by the gasket. To minimise contamination, all MP measurement buffers were pre-filtered through 0.22 μ m syringe filters.

Protein adsorption events were recorded for 60 seconds per sample using the AcquireMP software (Refeyn). Subsequent data analysis employed DiscoverMP software (Refeyn) alongside OriginPro 2021 (OriginLab).

3.5 Data analysis

A key aspect of this thesis is the data analysis, particularly the examination of trapping signals. The data analysis specific to Chapters 4 and 5 is as follows:

Chapter 4: All data presented in this work were analysed using MATLAB scripts. The raw data were filtered with a zero-phase Gaussian low-pass filter to the desired cut-off frequency (1 kHz or 5 kHz) using the `filtfilt.m` function. Probability density functions (PDF) were calculated with the `ksdensity.m` function. To compare two trapping signals, we aligned the signals by subtracting the median value from the trace (**Figure 4.1c**). Normalised RMS values (**Figure 4.2**) were determined by dividing the standard deviation of a 1-second trace by its mean value.

Chapter 5: In this study, MATLAB scripts were utilised for analysing all the presented data. Raw data were filtered using a zero-phase Gaussian low-pass filter with a specified cut-off frequency (1 kHz or 5 kHz) by applying the `filtfilt.m` function. Probability density functions (PDFs) were determined using the `ksdensity.m` function and filtered at 10 Hz. Normalised root mean square (RMS) values (**Figures 5.2, 5.6**) were calculated by dividing the standard deviation of a 0.5-second trace by its mean value. These values are statistically represented as a boxplot for a 5-second trace at different time intervals. The trace length for the last **Figure 5.13** was 0.015 seconds due to the short duration of each step.

Chapter 4: Monitoring the Dynamic of Single Ferritin Molecules upon Iron Loading

In this chapter, we explore the use of plasmonic optical nanotweezers to understand the effects of iron loading on single ferritin molecules. By using this advanced technique, we successfully trapped single apo- and holo-ferritins indefinitely, distinguished between them, and monitored their structural dynamics upon iron loading in real-time. The findings presented here have already been published in (54).

4.1 Introduction

Ferritin is a vital iron-storage protein found in large quantities across bacteria, plants, and the blood of many mammals, including humans (311–313). This intracellular protein plays a critical role in storing and releasing iron in a controlled manner. In humans, ferritin helps prevent diseases and detoxifies metals (311). Iron deficiency can lead to anaemia, while excess iron may cause oxidative stress in cells, potentially resulting in neurodegenerative diseases like Alzheimer's (312). When iron is loaded into ferritin, the protein undergoes conformational changes, shifting from its iron-free (apo) form to its iron-containing (holo) form (313,314). This conversion enables ferritin to function as an iron buffer within cells (315,316). However, the precise dynamics of this transformation remain unclear, as no current single-molecule techniques can observe these conformational changes without modifying the properties of ferritin.

Conventionally, iron accumulation in ferritin has been studied using ensemble measurements such as nuclear magnetic resonance (NMR) spectroscopy (317), X-ray diffraction (318), circular dichroism (319), and infrared spectroscopy (320). These methods are effective for analysing large quantities of proteins. While these techniques have provided valuable insights into ferritin's structure and function (318,321,322),

they are restricted in detailing the dynamic structural changes during iron loading and the interactions between iron and ferritin. Consequently, single-ferritin molecule characterisation techniques have gained attention for their potential to clarify molecular mechanisms, dynamic chemical processes, and molecular heterogeneity (323–325).

Electron microscopy (EM) techniques, like Cryo-scanning transmission EM (Cryo-STEM), have been used to study the crystallisation process of ferritin by capturing various conformations of individual ferritin proteins and reconstructing their dynamic pathways (326). However, the requirement for a vacuum environment in EM prevents study of proteins in their native liquid state. Additionally, the sample preparation process poses significant challenges in this procedure. Graphene liquid cell-transmission electron microscopy (GLC-TEM) has been employed by Narayanan et al. (327), to observe biomineralisation within individual ferritin proteins. This technique, however, requires encapsulating ferritin between graphene sheets to maintain a liquid environment, which can impact protein dynamics and potentially damage the protein structure (327). Conductive probe atomic force microscopy (CP-AFM) has demonstrated that holo-ferritin exhibits higher conductivity than apo-ferritin due to its metal core (328). Yet, the high stiffness of the AFM cantilever restricts its ability to detect minor domain movements or conformational changes in proteins (329).

Despite the invasive nature of these single-molecule characterisation techniques, they have provided significant insights into ferritin. Structurally, ferritin is a spherical protein consisting of 24 identical subunits, with an outer diameter of approximately 12 nm and an inner diameter of about 8 nm (330). These subunits self-assemble to form two types of channels—three-fold and four-fold—which facilitate the entry and exit of ions or molecules (331). The three-fold channels play a crucial role in ion transport and contain the ferroxidase activity site, where Fe^{2+} is oxidised to Fe^{3+} using O_2 or H_2O_2 (330). Furthermore, the acidic residues within the ferritin cavity generate a negatively charged environment, facilitating the incorporation of up to 4500 Fe^{3+} ions and the formation of inorganic crystals (92,330).

Recent advancements in molecular dynamics (MD) simulations and theoretical predictions have provided deeper insights into ferritin, particularly regarding the

dynamics of metal ion accumulation and the conformational changes in amino acid side chains (332). The mechanisms of metal-binding and biomineralisation within the ferritin cage have been explored through theoretical calculations and simulations. However, MD studies are generally limited to short timescales (nanoseconds).

This study presents the first direct observation of dynamic differences between individual, unmodified apo- and holo-ferritin molecules within a liquid environment. We used a custom-built characterisation setup to employ optical nanotweezers based on a double nanohole (DNH) (308,309,333,334). This setup as discussed in previous chapters, concentrates light into nanoscale hotspots using the DNH, generating a strong electric field gradient that traps single proteins, preventing them from diffusing away. Importantly, the nanoaperture approach allows for label-free detection, enabling us to monitor the dynamics of the trapped protein within a physiological solution (309). Our findings demonstrate that holo-ferritin exhibits a more rigid and compact conformation compared to apo-ferritin.

Significantly, this work represents the first real-time, dynamic tracking of iron mineralisation within individual ferritin molecules without protein modification. Controllable loading and release of iron ions (or other targeted ions and biomolecules) are crucial for applications related to iron regulation and nanotechnology using ferritin (335). Additionally, the hollow shell structure of apo-ferritin makes it a promising candidate for drug delivery and bioimaging in cancer cells (336–338). In-situ observation of iron loading in ferritin offers not only a deeper understanding of iron-related diseases but also potential avenues for their treatment. The ability to monitor the structural dynamics of ferritin during iron loading opens doors for the discovery of innovative strategies in these areas.

4.2 Optical nanotweezers distinguish between apo and holo-ferritin

When a dielectric object, such as ferritin, enters the hotspot of the DNH, the transmitted intensity through the DNH changes due to the higher refractive index of the protein compared to its surrounding environment, a phenomenon known as dielectric loading (308,339,340). **Figures 4.1a and 4.1b** illustrate the capability of the

developed setup to detect and distinguish between apo-ferritin (a) and holo-ferritin (b) based on the transmitted optical signals through the DNH structure.

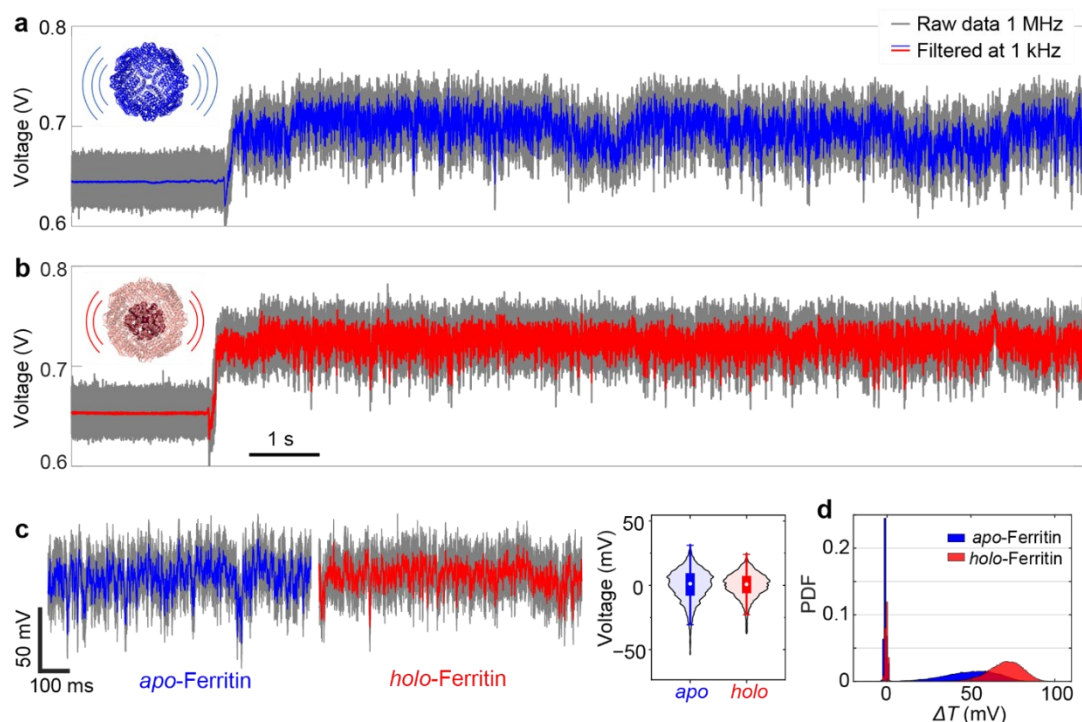


Figure 4.1: Single-molecule dynamics of apo- and holo-ferritin revealed by DNH. (a,b) Transmission measured through the DNH upon trapping a single apo-ferritin (a, blue) and holo-ferritin (b, red) for 12 seconds. Inset Figures depict the crystal structures of apo-ferritin (PDB: 2W0O) and holo-ferritin (PDB: 6TRZ), with curved lines illustrating their hypothesised structural fluctuations within the trap. (c) Left panel: Magnified 1-second traces from panels a and b, normalised to the transmission value with the highest probability for each trace. Right panel: Boxplot showing the interquartile range alongside a violin plot of two 1-second traces filtered at 1 kHz. (d) The probability density function (PDF) of the transmitted optical signal was calculated from the 12-second trapping traces of apo-ferritin (panel a, blue) and holo-ferritin (panel b, red). All traces were digitally filtered with a 1 kHz cutoff frequency. Data acquisition occurred at 1 MHz. Adapted from (54). Copyright 2023 The Authors (CC-BY 4.0)

A single DNH structure was used for trapping both apo- and holo-ferritin proteins within each experiment. Notably, the data presented in **Figures 4.1a** and **4.1b** were specifically obtained using DNH #3. The observed transmission signal from the DNH trapping apo-ferritin (**Figure 4.1a**) displayed a greater magnitude of fluctuation

compared to that of holo-ferritin (**Figure 4.1b**). This finding of a more stable optical signal for single-molecule holo-ferritin supports previous hypotheses suggesting a more rigid structure for the holo form compared to the apo form (341,342). To the best of our knowledge, this work presents the first experimental evidence of differential structural rigidity at the individual protein level for native ferritin molecules.

Figure 4.1c further reveals the distinction in structural dynamics between apo- and holo-ferritin by comparing 1-second transmission signals recorded by the DNH during the trapping of apo-ferritin (blue) and holo-ferritin (red). The transmission intensity of apo-ferritin exhibits a broader distribution in comparison to holo-ferritin (**Figure 4.1c**, left panel), suggesting a less stable structure for the apo form. This observation is confirmed by the right panel of **Figure 4.1c**, which presents the kernel density distribution of the two filtered (1 kHz) traces alongside a boxplot depicting the interquartile range.

Figure 4.1d presents the probability density function (PDF) for the change in transmission signal through the DNH (ΔT) recorded before and after trapping individual apo-ferritin and holo-ferritin molecules. Notably, trapping holo-ferritin resulted in a larger change in transmission amplitude compared to its apo counterpart. We propose that this increased ΔT for holo-ferritin can be attributed to its enhanced polarisability caused by the presence of a ferrihydrite core.

Two potential mechanisms might explain this observation. First, the ferrihydrite core in holo-ferritin likely increases the protein's overall conductivity by introducing two tunnelling barriers within the protein shell (328). As established by the Drude model (343), a direct correlation exists between a particle's conductivity and its polarisability. Second, existing research suggests a potential size difference between apo- and holo-ferritin, with holo-ferritin being approximately 2 nm larger (327,344,345). As documented in various studies, the size of a particle directly influences its polarisability (346–348).

The larger size and enhanced conductivity of individual holo-ferritin molecules are clearly identified by the higher $\Delta T/T_0$ in the optical signal, attributable to their increased polarisability. Table 4.1 provides the $\Delta T/T_0$ data for the proteins, measured across all six sets (trapping events in DNH #1-#6) of DNH structures which were shown in chapter 3. V_0 denotes the average APD signal for the empty DNH, and V_I

indicates the average APD signal when the protein is trapped. The transmission signal changes ($\Delta T/T_0$) were determined using the formula $(V_1 - V_0)/V_0$. Notably, four out of the six structures showed a greater $\Delta T/T_0$ value for holo-ferritin compared to apo-ferritin.

Table 4-1. Change in the transmission signal of six different DNHs upon trapping apo and holo-ferritin proteins. Adapted from (54). Copyright 2023 The Authors (CC-BY 4.0)

DNH	Protein form	V_0	V_1	$\Delta T/T_0$
#1	Apo	1621	1715	0.057
	Holo	1838	1895	0.031
#2	Apo	909	960	0.056
	Holo	874	1040	0.189
#3	Apo	644	695	0.079
	Holo	653	724	0.108
#4	Apo	776	853	0.099
	Holo	704	752	0.068
#5	Apo	620	659	0.062
	Holo	755	825	0.092
#6	Apo	660	760	0.151
	Holo	813	939	0.154

Figure 4.2 presents the normalised root mean square (NRMS) and the probability density function (PDF) of the normalised voltage, both reflecting fluctuations in the transmission signal when individual ferritins are trapped. The results shown in **Figure 4.2** indicate that the differences in trapping dynamics between apo- and holo-ferritins are independent of potential geometrical variations or the resonant behaviour of DNH structures (333,349). Previous studies have shown that the hydrodynamic movement of particles in a harmonic trap result in a linear relationship between the protein's molecular weight and the RMS of the trapping signal. Consequently, trapping holo-ferritin is expected to yield a higher NRMS due to its larger molecular weight compared to apo-ferritin. However, in our experiment, four out of the six DNH structures (#1, #2, #3, #5) reported significantly lower RMS values for holo-ferritins (p-value < 0.0001, **Figure 4.2a**). Also, the binding of iron to the negatively charged interface of holo-ferritin reduces its overall motion, resulting in a more stabilised conformation and, consequently, a lower NRMS in the trapping signal.

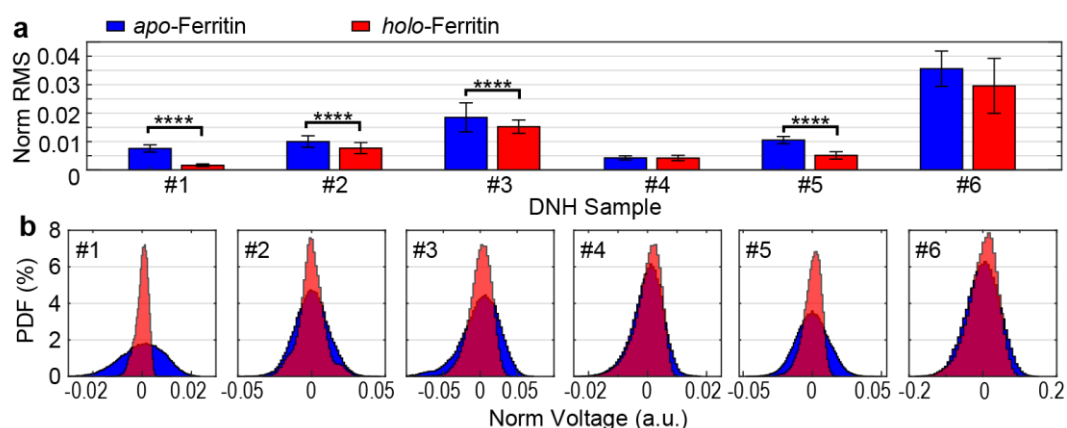


Figure 4.2: Characterisation of single-molecule trapping dynamics for apo- and holo-ferritin. (a) Normalised root mean square (NRMS) of the transmission signal obtained during the trapping of individual apo-ferritin (blue) and holo-ferritin (red) molecules within six distinct DNH structures. (b) Probability density function (PDF) of 20-second transmission signal traces recorded for apo-ferritin (blue) and holo-ferritin (red) trapped in six different DNH structures. All data were acquired at 1 MHz and subsequently subjected to Gaussian filtering at 1 kHz. Statistically significant differences are represented by asterisks (**** $p < 0.0001$). Adapted from (54). Copyright 2023 The Authors (CC-BY 4.0)

We conducted a control experiment to show trapping signal from the same DNH structure is generally consistent when acquired within a narrow time frame. We trapped the same protein—two single apo-ferritin molecules—within a short time frame (3 minutes) using the same DNH structure (**Figure 4.3 a-b**). Both the RMS and the normalised change in transmission signal ($\Delta T/T_0$) exhibited a high degree of similarity between the two trapping events (**Figure 4.3 c-d**). This consistency in the dynamic characteristics of identical proteins trapped within the same DNH structure highlights the reproducibility of our measurement technique.

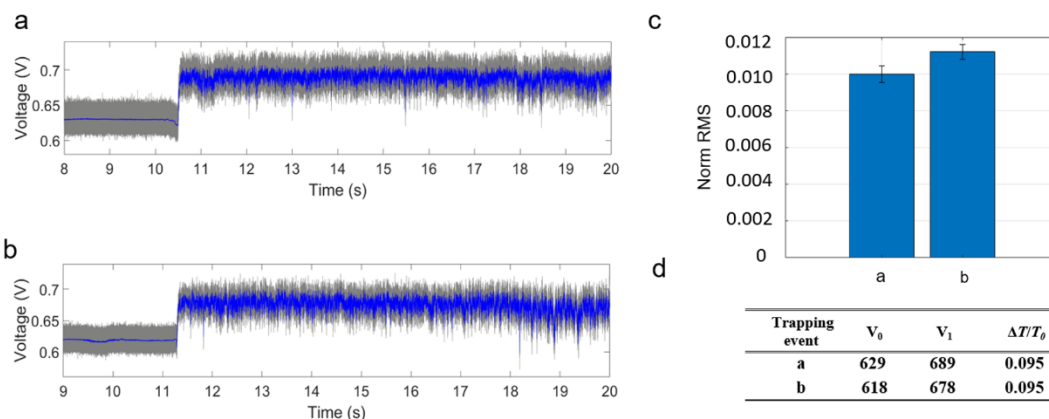


Figure 4.3: Two trapping events of apo-ferritin within the same DNH structure. (a) the first trapping event and transmission signal of single apo-ferritin in DNH #2, (b) the second trapping event and transmission signal recorded 3 minutes after the first trap, (c) a comparison of the normalised RMS values for the two traces with apo-ferritin trapped, and (d) a comparison of the changes in the transmission signal ($\Delta T/T_0$) between the two consecutive trapping events of apo-ferritin.

Figure 4.4, the power spectral density (PSD) graph illustrates the dynamic behaviours of apo-ferritin and holo-ferritin under various trapping scenarios. **Figure 4.4a** shows the APD signal over time, with trapped apo-ferritin exhibiting larger fluctuations than trapped holo-ferritin. **Figure 4.4b** presents the PSD derived from the Fourier transform of the time-domain signal to the frequency domain. This graph shows apo-ferritin exhibits significantly higher PSD values in the 3–150 Hz (lower frequencies) range, indicating larger conformational fluctuations compared to holo-ferritin (350). These fluctuations are captured by the optical signal and reflected in the RMS values, which are similar to the root mean square deviation (RMSD) in molecular dynamics simulations. Higher RMS values for apo-ferritin suggest lower structural stability, while lower RMS values for holo-ferritin indicate a more rigid and stable structure due to the ferrihydrite core (351).

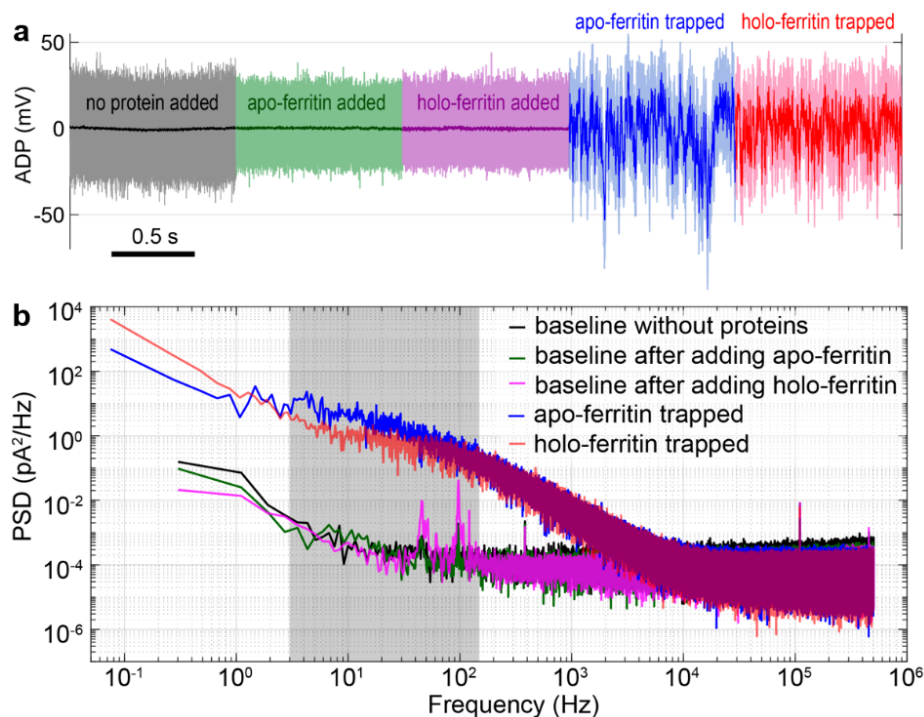


Figure 4.4: Noise comparison across different frequency domains for the same DNH (#3) under various conditions. (a) Shows baseline before protein addition, after adding apo-ferritin, and after adding holo-ferritin, with no protein trapped. Data are presented in raw form (light-coloured) and digitally filtered at 1 kHz. (b) Displays the power spectral density (PSD) of the baselines and transmission traces from panel (a). The grey area highlights the frequency range where the transmission signal of trapped apo-ferritin exhibits larger fluctuations compared to holo-ferritin. Baselines show no significant differences except for slightly higher line noise (50 Hz and 100 Hz) after adding holo-ferritin, possibly due to alignment variations. Data were recorded at a sampling rate of 1 MHz. Adapted from (54). Copyright 2023 The Authors (CC-BY 4.0)

It is worth noting that at the same time, we were working on this research, another group at Nanjing Normal University was clarifying the differences in the dynamics of ferritin (323). Using ferritin and apo-ferritin as models, they demonstrated that nanopores of comparable size can effectively discriminate proteins based on dwell time and fraction distribution. Smaller nanopores achieve discrimination through current fluctuations caused by protein vibrations. The major challenge of using nanopores to study ferritin or single proteins is the rapid protein translocation, occurring within microseconds, which prevents tracking large domain protein movement and kinetics (352).

4.3 *In situ* iron loading on single apo-ferritin molecules

The findings in **Figures 4.1** and **4.2** establish a robust technique for differentiating between individual apo- and holo-ferritin molecules based on their distinct structural dynamics. **Figure 4.5** further underlines this technique's exceptional capability to monitor real-time, global conformational changes within apo-ferritin during iron ion loading, describing the link between structural dynamics and the folding/unfolding of pore channels. This experiment involved monitoring the transmission signal of a trapped apo-ferritin molecule as Fe^{2+} ions were introduced via a microfluidic system.

Figure 4.5a depicts the 30-minute transmission trace of a single apo-ferritin trapped within a DNH structure, along with magnified views presented in **Figures 4.5b-e**. These **Figures** illustrate the *in situ* iron loading process. Following the trapping of apo-ferritin, the solution was replaced with a 2 mM Fe^{2+} ferrous solution using a flow rate of 4.5 $\mu\text{L}/\text{min}$ within the microfluidic system. The arrows in **Figure 4.5a** designate specific time points: protein trapping, initiation of iron injection (flow rate change from 0 to 4.5 $\mu\text{L}/\text{min}$), a point before the ferrous solution reaches the protein (**Figure 4.5b**), and time points after the protein's exposure to the ferrous solution for varying durations (**Figures 4.5c-e**).

Prior to the ferrous solution reaching the protein (**Figure 4.5b**), the apo-ferritin's trapping signal exhibits relatively stable fluctuations, consistent with the observations in **Figure 4.1a**. Once the ferrous solution arrives at the trapping site (**Figures 4.5c** and **d**), non-uniform patterns emerge in the transmission signal. Notably, certain segments (highlighted in purple) display reduced fluctuations, suggesting a potential correlation between iron loading and conformation dynamics of the trapped protein.

These "on-off" (seen as blue-purple) patterns in the signal are explained by the folding of eight gated pores, or three-fold channels, in ferritin, which is created by assembling 24 identical subunits. Ferritin's three-fold channels, which are hydrophilic due to the polar side chains aspartate and glutamate lining them, serve as the main channel for iron ion transport (331,353). Due to the ion channels' unfolding, the apo-ferritin is dynamically unstable, which causes large-magnitude fluctuations in the trapping signals (blue segments).

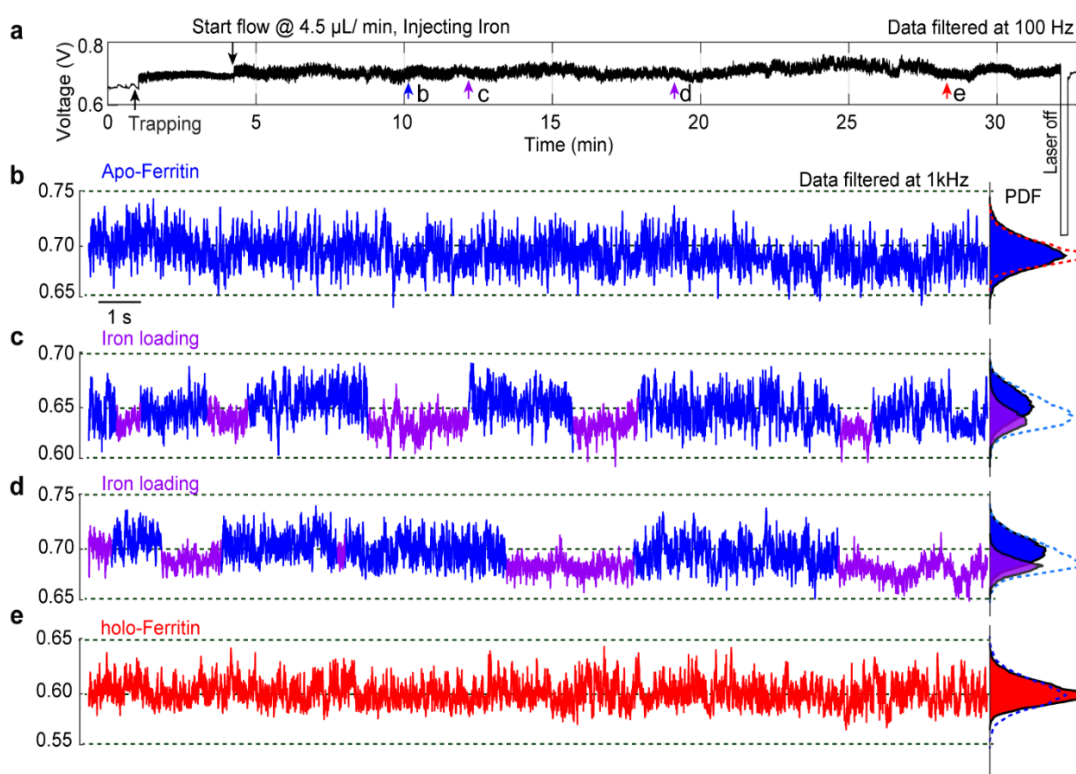


Figure 4.5: In-situ iron loading into a trapped apo-ferritin. (a) This panel shows the continuous transmission trace of a single apo-ferritin trapped in the hotspot of a DNH, which was then exposed to a ferrous solution for over 20 minutes. Turning off the laser for 5 seconds caused the transmission signal to return to baseline, indicating the protein was released. (b) Displays a 20-second transmission trace of the trapped apo-ferritin before the ferrous solution reached the hotspot, along with the probability density function (PDF) of the trace on the right (blue). For comparison, the red dashed curve represents the PDF from panel e. (c, d) Show 20-second transmission traces after the apo-ferritin was exposed to the ferrous solution. Segments with lower RMS are highlighted in purple, identified by RMS changes as detailed in **Figure 4.6**. The PDF plot on the right presents the PDFs of the purple and blue segments, as well as the PDF of the entire trace (cyan dashed curve). (e) Illustrates a 20-second transmission trace after the apo-ferritin was exposed to the ferrous solution for more than 20 minutes, accompanied by the PDF of the trace (red) and the PDF from panel b (dashed blue). Adapted from (54). Copyright 2023 The Authors (CC-BY 4.0)

When Fe^{2+} binds to all the channels' available sites, the channels fold, making the protein more rigid and reducing the fluctuations in the trapping signal (purple

segments). The three-fold channels transport the resultant Fe^{3+} to the protein cavity following the first oxidation of Fe^{2+} at the ferroxidase sites. When the transfer is complete, these channels unfold again, causing the protein to relax and increasing the trace's fluctuations (blue segments). The "on-off-on" patterns in the trapping signal are produced by repeating the mentioned actions.

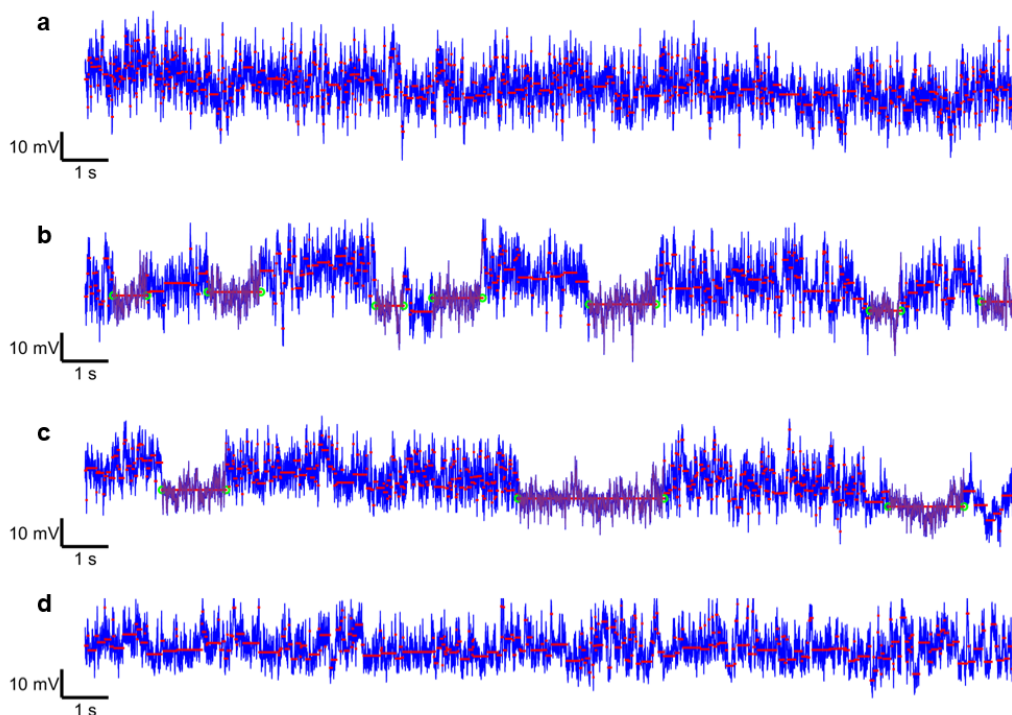


Figure 4.6: Level detection using standard deviation changes. Red lines with green circles at both end mark segments with lower RMS values. A custom MATLAB program was developed to identify low RMS segments within the trapping traces presented in **Figure 4.5**. This program identified the steps based on changes in standard deviation (STD). The red represents stability regions with similar STD values across traces. A threshold of 0.5 times the maximum standard deviation ($0.5 \times \max(\text{STD})$) was established for step identification. This algorithm validated segments longer than 500 milliseconds as lower RMS segments. The program successfully identified these segments and marked them in purple. Following automated identification, some very closely spaced segments were manually connected to ensure accurate representation. Adapted from (54). Copyright 2023 The Authors (CC-BY 4.0).

It is noteworthy that the average duration of the on-off cycle observed in this study aligns with the binding times previously reported through bulk measurement techniques (353). As reported previously, when ions occupy all ferritin metal binding sites, it takes approximately 10-20 seconds for the metal to be transported to the

ferroxidase centres, where it binds and undergoes oxidation to Fe^{3+} (353). The traces presented in **Figures 4.5c-d** suggest that the dwell time for the on and off states ranges from 2 to 5 seconds. Notably, these dwell times exhibit variability between individual ferritin molecules, as evidenced by repeated experiments using different DNH structures, which revealed distinct dwell times of approximately 20 seconds (**Figure 4.7**).

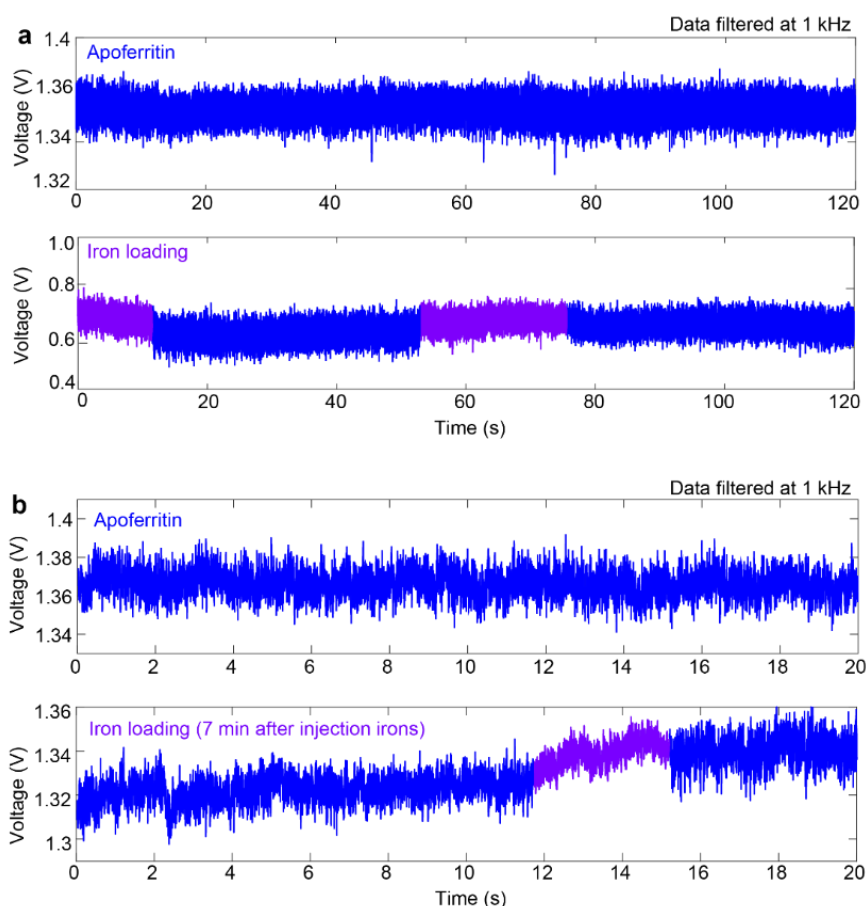


Figure 4.7: Two repeat experiments of iron (Fe^{2+}) loading on a single apo-ferritin molecule. (a) The top trace displays a two-minute transmission signal while a single apo-ferritin is trapped in the DNH structure. The bottom trace shows the transmission signal after the apo-ferritin is exposed to the ferrous solution, resulting in distinct "on" (blue) and "off" (purple) patterns. (b) The top trace depicts a twenty-second transmission signal while a single apo-ferritin is trapped in the DNH structure. The bottom trace illustrates the transmission signal for twenty seconds after the apo-ferritin is exposed to the ferrous solution, again showing "on" (blue) and "off" (purple) patterns. All data were acquired at a sampling rate of 1 MHz and then digitally filtered with a cut-off frequency of 1 kHz. Adapted from (54). Copyright 2023 The Authors (CC-BY 4.0)

Furthermore, the observed repetitive on-off patterns, likely induced by ferroxidase pore gating (conformational change), not only facilitate the entry of additional Fe^{2+} ions into the protein cage but also assist in the translocation of Fe^{3+} from the ferroxidase centre to the ferritin's internal cavity (313,354).

We ensured that the ferrous solution was continuously supplied to the protein site to maintain a ratio of Fe^{2+} to ferritin greater than 200:1 (355,356). Following 22 minutes of iron delivery to the trapping site, the transmission signal amplitude exhibited a decrease accompanied by reduced fluctuations (**Figure 4.5e**). This observation is confirmed by the decrease in median RMS from 6.8 mV to 5.4 mV (see RMS bar plot, **Figure 4.8**), suggesting increased protein rigidity upon iron mineralisation within its core. This finding aligns with the observations presented in **Figures 4.1** and **4.2**.

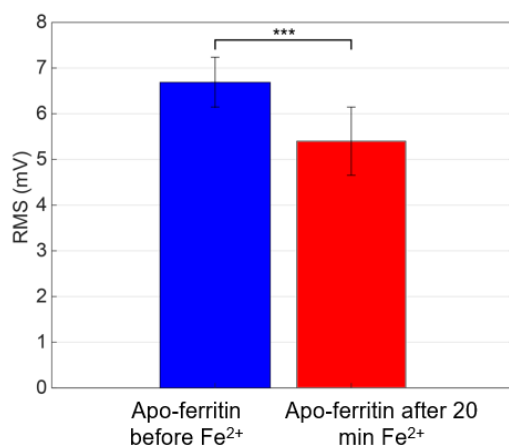


Figure 4.8: Transmission signal RMS before and after biomineralization. (a) RMS of the transmission signal for a single trapped apo-ferritin (blue) after 20 minutes of exposure to the Fe^{2+} solution (red) (from **Figure 4.5**). The asterisks denote that these two data sets are significantly different with a p-value of 0.0002. Adapted from (54). Copyright 2023 The Authors (CC-BY 4.0)

Previous studies employing GLC-TEM reported the initiation of iron oxide core formation within apo-ferritin after 1 hour of biomineralisation (327). However, our single-molecule data indicate that this biomineralisation process occurs within approximately 20-30 minutes (marked by the red arrow in **Figure 4.5a**), significantly faster than the previously reported timeframe. This accelerated process may be

attributed to the elevated temperature (~ 49.8 °C) at the trapping site due to laser heating.

4.4 Temperature at the trapping site

It is important to note that due to the high absorption at metallic nanostructures, we ohmic losses happens which result in heating (79). To determine the temperature at the trapping site, we performed finite-element simulations using COMSOL Multiphysics (85). **Figure 4.9** shows the simulated temperature profile of a double nanohole at the laser power of 32 mW used in this study. Considering the best-case scenario, where all the absorbed laser power is converted to heat, the temperature in the DNH structure is estimated to be 49.8 °C.

this temperature remains below the 56 °C threshold at which ferritin pores have been observed to melt (357). Additionally, the global structure of ferritin exhibits stability up to 85 °C (357), suggesting that laser-induced heating does not significantly affect the overall protein structure.

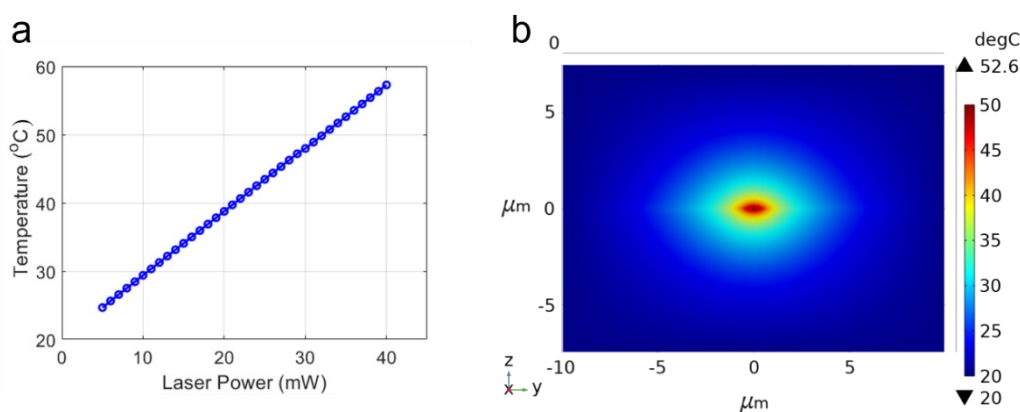


Figure 4.9: Simulation estimates of laser heating. (a) Finite-element simulation illustrating the temperature within the DNH gap as a function of laser power. (b) Finite-element simulation depicting the temperature profile of the DNH structure when illuminated by a focused 32 mW laser beam. Adapted from (54). Copyright 2023 The Authors (CC-BY 4.0)

4.5 Control test of iron loading on single ferritin molecules

Control experiments involving the injection of a phosphate buffer solution containing Fe^{3+} (instead of Fe^{2+}) into a DNH containing a trapped apo-ferritin did not yield the (358)

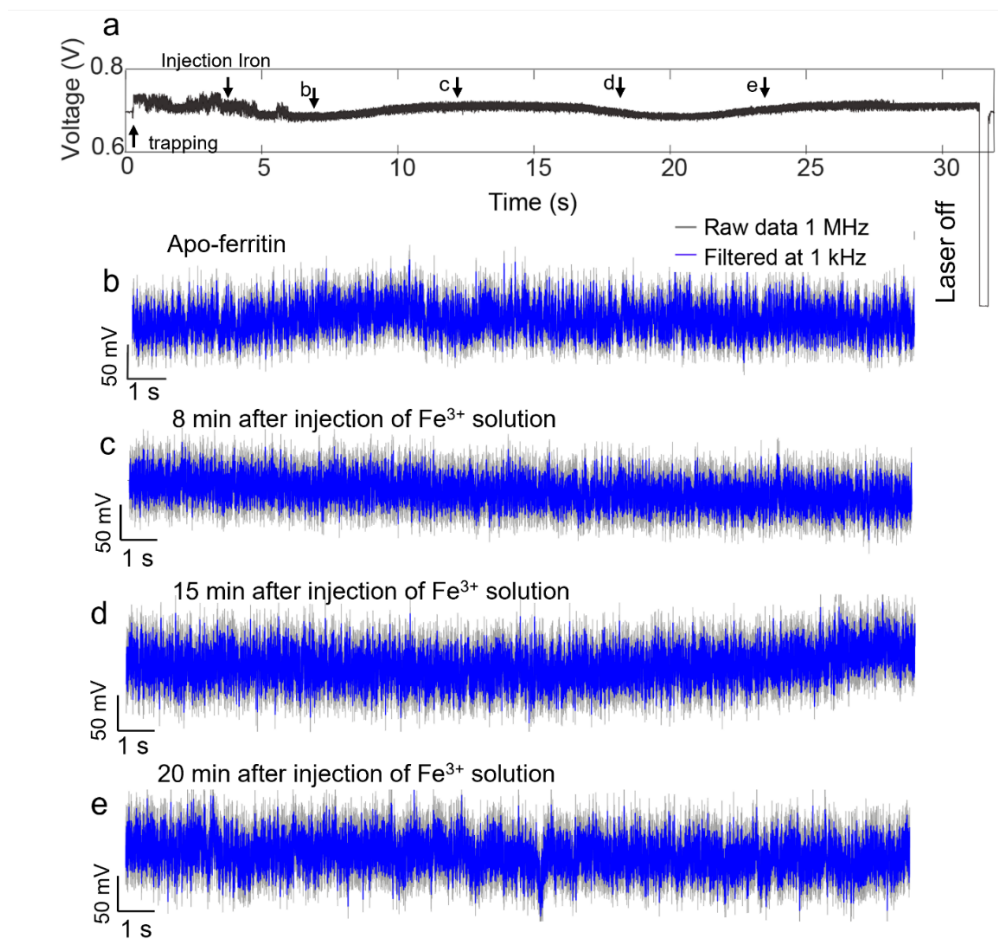


Figure 4.10: Introducing iron (Fe^{3+}) to the trapped single ferritin molecule. (a) Continuous transmission trace of a single apo-ferritin trapped within the hotspot of a DNH structure. The apo-ferritin was subsequently exposed to the ferrous solution for an extended period exceeding 20 minutes. Following laser deactivation for 5 seconds, the transmission signal returned to baseline, indicating the release of the protein molecule. (b) A 20-second segment of the transmission trace was recorded before the ferrous solution reached the hotspot, capturing the behaviour of the trapped apo-ferritin alone. (c) & (d) 20-second segments of the transmission trace acquired after the apo-ferritin was exposed to the ferric solution. These segments illustrate the response of the apo-ferritin to the presence of ferric ions, which is expected to differ from the response to ferrous ions (as shown in **Figure 4.5**). (e) A 20-second segment of the transmission trace was recorded after prolonged exposure of the apo-ferritin to the ferric solution (over 20 minutes). This segment provides additional information about the interaction between the apo-ferritin and ferric ions. Adapted from (54). Copyright 2023 The Authors (CC-BY 4.0)

observed on-off pattern (**Figure 4.10**). As the iron-binding sites in ferritin specifically bind to ferrous (Fe^{2+}) ions (358), we conducted a control experiment where apo-ferritin was exposed

to ferric iron (Fe^{3+}) solutions. **Figure 4.10a** shows the transmission signal of the DNH with apo-ferritin trapped in the PB solution. We then replaced the solution in the chamber with a 2 mM ferric solution while keeping the protein trapped. **Figures 4.10b-d** illustrate the optical trace after the apo-ferritin was exposed to the ferric solution for 8 minutes, 15 minutes, and 20 minutes, respectively. No “on-off” patterns were observed. **Figure 4.11** compares the RMS of the optical trace obtained before apo-ferritin was exposed to the ferric solution (trace shown in **Figure 4.10b**) and after 20 minutes of exposure (trace shown in **Figure 4.10e**). The lack of significant difference in the RMS between the two traces suggests that apo-ferritin retained its relatively flexible conformation, indicating no iron loading occurred. These **Figures** confirm that the “on-off” patterns observed in **Figure 4.5** are due to the iron-loading activity of ferritin.

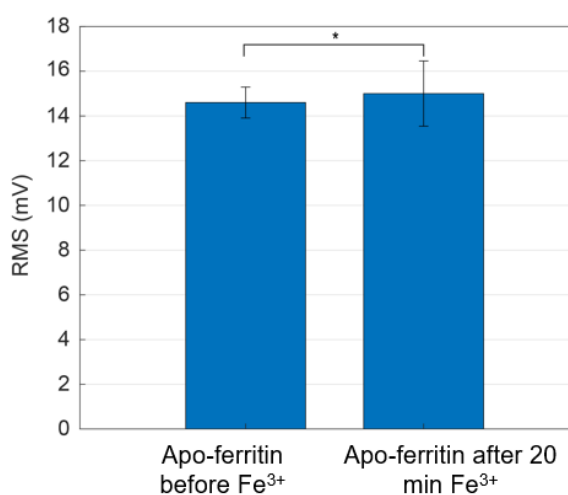


Figure 4.11: RMS of 20-second transmission traces was measured for a single apo-ferritin molecule both when trapped in PB solution and after exposure to a Fe^{3+} solution for over 20 minutes. The analysis showed no significant difference ($p = 0.119$) between the RMS values from these two conditions. Adapted from (54). Copyright 2023 The Authors (CC-BY 4.0)

4.6 Conclusion

This study presented the first experimental demonstration of the dynamic differences between individual, unlabelled apo- and holo-ferritin molecules using an optical nanotweezer system. This precise optical setup facilitated the differentiation of apo- and holo-ferritin at the single-molecule level and enabled the label-free monitoring of a single apo-ferritin's real-time conversion into holo-ferritin.

Detailed analysis revealed that the optical trapping signals from the same DNH structure, when trapping different protein forms (apo- or holo-ferritin), provided two effective parameters for discrimination between these two forms: 1) RMS of the trapping signal: consistent with the inherent structural stability of holo-ferritin, it exhibited a lower RMS compared to its apo counterpart. 2) Transmission signal change: trapping holo-ferritin resulted in a 41% larger average change in the transmission signal (Table 4.1) compared to apo-ferritin. This can be attributed to the higher polarisability of holo-ferritin due to its larger size and increased conductivity.

Furthermore, this work provides the first experimental evidence for *in situ* iron loading into a single, unmodified apo-ferritin molecule. By analysing the transmission signals, we tracked the structural dynamics of ferritin related to the gating behaviour of its three-fold channels. These channels undergo unfolding (on) and folding (off) cycles, allowing Fe^{2+} entry into the ferroxidase centres (unfolding) and facilitating the transfer of Fe^{3+} to the protein core (folding). Monitoring this process associated with the biomineralisation of iron ions within ferritin opens exciting possibilities for precise control of protein cages for drug delivery in living systems and metal nanoparticle encapsulation.

Chapter 5: Structural Dynamics and Disassembly of Single Ferritin Molecules

In the previous chapter, we extensively explored the structural dynamic differences between apo- and holo-ferritin and the effect of iron loading on single ferritin molecules. In this chapter, we investigate the effect of iron loading on single ferritin molecules using optical nanotweezers. Additionally, we analyse the impact of acidic pH on the structure of ferritin and track the disassembly of individual ferritin molecules in acidic environments. Notably, the results of this chapter are published in reference (55).

5.1 Introduction

Ferritin comprises a spherical cage formed by 24 identical subunits (24-mer) (359,360). It sequesters iron in the form of a ferrihydrite (Fe^{3+}) core, strategically located within its central cavity. Upon cellular demand, ferritin releases iron as ferrous iron (Fe^{2+}) through a controlled mechanism (361,362). This released Fe^{2+} is vital for cellular function, particularly in preventing oxidative damage (361,362). Its participation in the Fenton reaction, involving the decomposition of hydrogen peroxide and interaction with reactive oxygen species (ROS), highlights its importance in maintaining cellular redox balance (361,362).

The mobilisation of iron from the ferritin core is facilitated by various reductants interacting with the protein through its 3-fold channels (93,363). Ascorbic acid (AA), a key player in cellular metabolism, acts as a reducing agent to promote iron release from ferritin (364). Notably, patients with hemochromatosis, a genetic disorder characterised by iron overload, exhibit lower ascorbate levels compared to healthy individuals (365) This deficiency necessitates ascorbate supplementation during chelation therapy, a treatment strategy for iron overload. However, high ascorbate

levels can be detrimental, as the Fenton reaction can generate free radicals, potentially damaging proteins, lipids, and DNA (366). Additionally, high ascorbate concentrations can create an acidic environment, potentially impacting ferritin dynamics and iron release mechanisms (87). Studies have shown that ferritin disassembles under extremely acidic conditions ($\text{pH} \leq 2$), but it can reassemble at higher pH values due to electrostatic interactions (367).

These unique properties of ferritin, particularly its ability to store and release iron in a controlled manner, make it a promising candidate for various biomedical applications. Its potential application spans drug delivery systems (96,99) and imaging techniques (368,369). However, to fully harness its potential for these applications, a deeper understanding of ferritin's behaviour under diverse conditions, including the influence of various reductants like ascorbate, is essential (98). This knowledge will help in developing optimised ferritin-based therapeutic strategies.

Ferritin's response to pH changes has been extensively studied using various analytical tools. Techniques like gel electrophoresis (370) circular dichroism (371) ultracentrifugation (372) and fluorescence microscopy (373) have provided valuable data on the reversible disassembly and assembly of ferritin at different pH levels. Additionally, small-angle X-ray scattering (SAXS) has offered detailed insights into the pH-dependent structural alterations and assembly kinetics of ferritin at the population level (367). However, a key limitation of these bulk measurement techniques is that they only offer an averaged response for the entire protein population, failing to capture the heterogeneity present within the sample (374).

Recent advancements have witnessed the application of high-speed atomic force microscopy (HS-AFM) and molecular dynamics (MD) simulations to investigate ferritin disassembly and reassembly at a single-molecule level (324). Maity et al. (324) employed these techniques to observe the real-time behaviour of individual ferritin molecules under acidic conditions. Their study revealed a two-stage disassembly process involving pore formation through the 3-fold channels and fragmentation into dimers. This work provides significant insights into the dynamics of subunit-subunit interactions during ferritin disassembly. Nevertheless, HS-AFM is limited by the rigidity of its cantilever, potentially hindering the capture of certain intermediate steps and subtle domain movements within the disassembly process (29). Conversely,

although MD simulations offer valuable information on protein behaviour, their short simulation times (typically nanoseconds) pose a challenge in accurately tracking large domain movements within biological entities such as ferritin (375). Therefore, fully grasping the dynamic and kinetic behaviours of single, native ferritins—particularly their iron binding, release, and interactions with other biomolecules—remains difficult with these methods.

Building upon our previous work (Chapter 4) demonstrating the use of optical nanotweezers to monitor dynamic changes in individual, unmodified ferritins during in-situ iron loading (54), this study investigates the structural flexibility and disassembly kinetics of single ferritin molecules under two distinct conditions: exposure to ascorbic acid (reducing agent) and acidic environments. Our findings reveal that ferritin exhibits increased structural fluctuations at ascorbic acid concentrations approaching saturation, attributable to substantial iron release caused by the reducing agent. Additionally, when exposed to a highly acidic environment (pH 2), ferritin shows evident instability, that ultimately leads to a stepwise disassembly process. This work represents the first instance where the disassembly pathway of single ferritin molecules has been tracked, along with the temporal duration of each intermediate fragment during the disassembly process. Furthermore, to validate the existence of these intermediate fragments at pH 2, we employed a recent application of interferometric scattering known as Mass Photometry (MP) (189). This complementary technique confirmed the presence of the intermediate fragments at pH 2. Understanding the disassembly process of ferritin at a single-molecule level sheds light on a critical initial step for exploiting ferritin's potential in nanotechnology-based applications, such as drug delivery and bio-imaging (96,98,99).

5.2 DNH structures used in this study

In this study, we employed five different DNH nanostructure designs, detailed in **Figure 5.1**. Although we used the same FIB parameters described in the materials and methods section, variations in gap size were observed. As previously explored in our research, these differences in gap size can potentially affect the transmission signal (54).

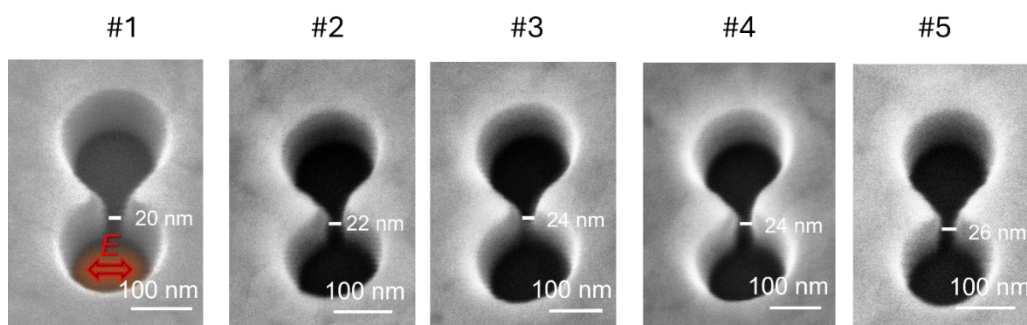


Figure 5.1: Scanning electron microscopy (SEM) images of the five DNH structures utilised throughout this study. All images are captured at a 20° tilt angle for optimal visualisation of the gap. The inset within panel #1 indicates the polarisation direction of the incident light beam. For clarity, the specific DNH structures employed in each subsequent **Figure** are explicitly identified within the corresponding **Figure** captions. Adapted from (55). Copyright 2024 The Authors.

5.3 Effect of ascorbic acid (AA) on the dynamic of single ferritin molecules

Ascorbic acid (vitamin C) acts as a reducing agent, facilitating the conversion of ferric iron (Fe^{3+}) into ferrous iron (Fe^{2+}). This reduction process, however, is accompanied by an increase in the production of reactive oxygen species (ROS), particularly hydroxyl radicals ($\bullet\text{OH}$). (376) As depicted in Eq. 5-1, this oxidation reaction leads to the formation of ascorbyl radicals and ferrous ions:

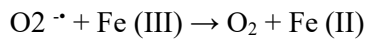


The ascorbyl radical, a transient intermediate, subsequently reacts with molecular oxygen (O_2) in a regeneration step (Eq. 5-2). This reaction reforms ascorbic acid and generates the superoxide anion ($\text{O}_2^{\bullet -}$):



Both the superoxide radical and the ascorbate radicals interact with ferritin, the primary iron storage protein within cells. These interactions facilitate the conversion of ferric iron stored within the ferritin core to ferrous iron, thereby promoting the mobilisation of iron from the protein (Eqs. 5-3 and 5-4): (377,378)





5-4

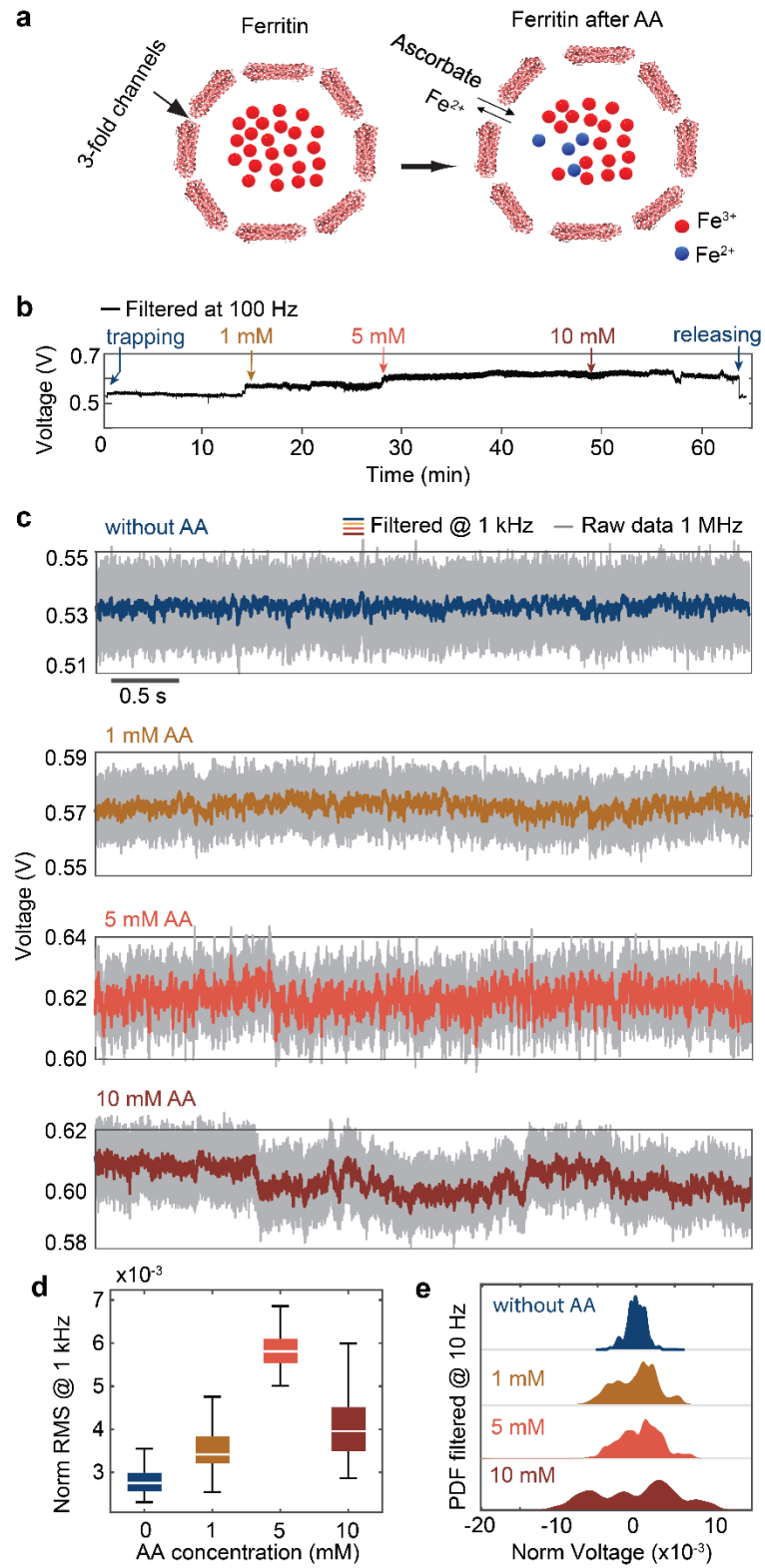


Figure 5.2: Impact of ascorbic acid on the dynamics and iron release of ferritin. (a) The cartoon depicts a schematic representation of ferritin before and after exposure to ascorbic acid. The illustration highlights the permeation of ascorbate and ferrous iron (Fe^{2+}) through the 3-fold channels of the protein. (b) Continuous transmission traces acquired during the trapping of a single ferritin molecule within a phosphate buffer (PB) solution. The traces depict the sequential introduction of increasing ascorbic acid concentrations at the trapping site, followed by the eventual release of the ferritin. (c) Five-second selections of the transmission traces from panel (b) for the same trapped ferritin exposed to various ascorbic acid concentrations. The positions of these selections are indicated by arrows within panel (b). (d) The box plots represent the normalised RMS values calculated every 0.5 seconds from the five-second traces shown in panel (c). The data were Gaussian-filtered at a cut-off frequency of 1 kHz. White lines within each box plot show the median value for the corresponding dataset. The boxes represent the interquartile range, covering the 25th and 75th percentiles of the data. (e) This panel displays the PDF for the five-second transmission traces of a single ferritin molecule exposed to different ascorbic acid concentrations. The data were acquired at a sampling rate of 1 MHz and subsequently Gaussian-filtered at cut-off frequencies of 1 kHz and 10 Hz. Statistical significance testing ($p < 0.0001$ for all comparisons) was performed on the normalised RMS data presented in this **Figure**. DNH structure #1, whose SEM image is shown in **Figure 5.1**, was used for this experiment. Adapted from (55). Copyright 2024 The Authors.

Figure 5.2a depicts the proposed mechanism of ascorbate-mediated iron release from ferritin. Ascorbic acid diffuses into the ferritin core through the 3-fold channels, where it binds to ferric ions (Fe^{3+}) at the ferroxidase centre (379). This binding facilitates the reduction of ferric ions to ferrous iron (Fe^{2+}), leading to their subsequent release from the protein (379). **Figures 5.2b** and **5.2c** show the transmission signals of a trapped ferritin molecule exposed to different ascorbic acid concentrations. The intensity of the transmitted light correlates with the conformation of the trapped protein. Therefore, the RMS of the optical signals reflects the fluctuation in protein conformation (54). The RMS values of the traces in **Figure 5.2d**, along with a repeat experiment presented in **Figure 5.3**, reveal a significant increase in the dynamic behaviour of ferritin at higher ascorbic acid concentrations.

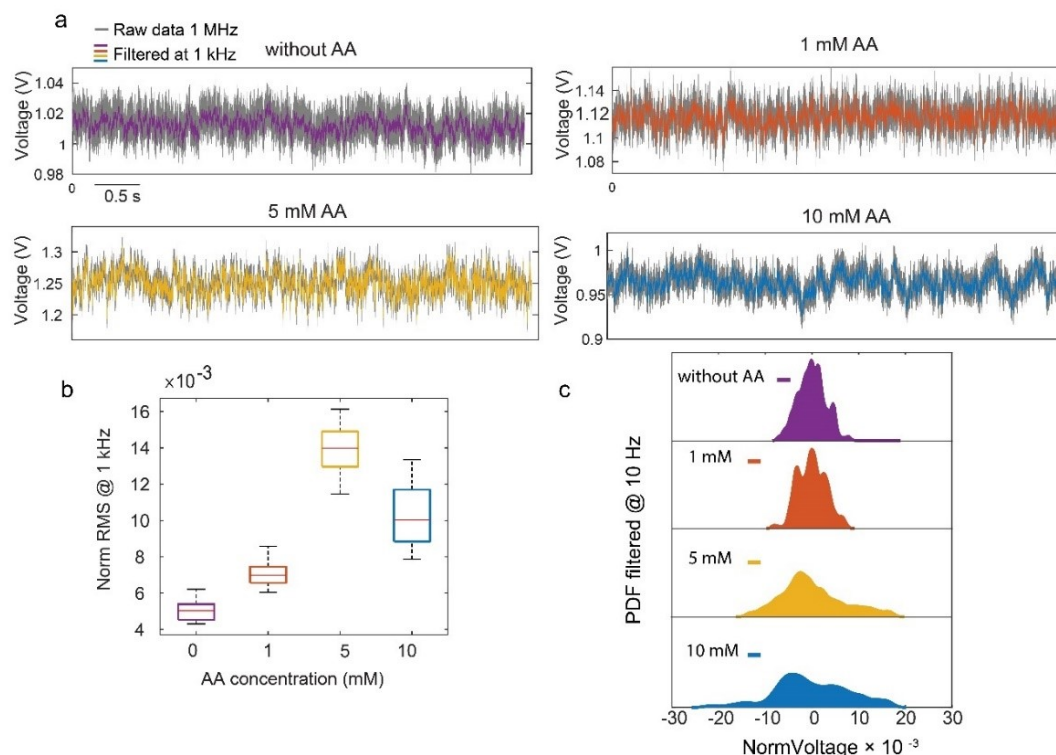


Figure 5.3. Repeating test on the effect of AA on the dynamics of a single ferritin molecule. (a) This panel displays the transmission signal recorded during the trapping of a single ferritin molecule within DNH structure #2 (refer to **Figure 5.1** for the SEM image). The signal depicts the response to varying AA concentrations (1 mM, 5 mM, and 10 mM). (b) This panel presents the normalised RMS values calculated from 5-second segments of the transmission signal in panel (a). The RMS values were obtained while the trapped ferritin was exposed to different ascorbic acid concentrations within a phosphate buffer (PB) solution. The data were collected every 0.5 seconds and subsequently subjected to Gaussian filtering at a cut-off frequency of 1 kHz. The box plot illustrates the interquartile range, encompassing the 25th and 75th percentiles of the data. (c) This panel illustrates the probability density function (PDF) for the 5-second transmission traces acquired from the single ferritin exposed to different ascorbic acid concentrations. The data were initially acquired at a sampling rate of 1 MHz and then processed using a Gaussian filter with cut-off frequencies of 1 kHz and 10 Hz. Adapted from (55). Copyright 2024 The Authors.

Introducing 1 mM and 5 mM ascorbic acid solutions to the trapped ferritin resulted in 21% and 110% increases in RMS, respectively. This observation suggests an accelerated rate of iron chelation and subsequent release of ferrous ions at higher

ascorbate concentrations (377). The enhanced protein dynamics likely arise from the opening and closing of 3-fold channels as ascorbate anions cross these channels and interact with residues like cysteine (380,381). A concentration of 10 mM ascorbic acid resulted in an RMS value that remained higher than 1 mÅ but lower than 5 mÅ (**Figure 5.2d**). This can be attributed to saturation kinetics, where the available binding sites for interaction between ascorbate and the iron core become limited, leading to the formation of surface complexes, as reported previously (377). Furthermore, the opening of channels facilitates the permeation of ascorbate and ferrous iron, ultimately accelerating the dissolution of the ferric core (380). The reduction of the ferric core, which acts as a ligand for ferritin, destabilises the protein due to diminished ligand binding (54). Also, the transmission trace for 10 mM ascorbic acid (**Figure 5.2c**) following exposure for more than 40 minutes displays slower fluctuations with larger amplitudes, further evidenced by the wider distribution of the probability density function (PDF) at 10 mM AA (**Figure 5.2e**).

This channel-gating behaviour mentioned above is also observed when apo-ferritin is exposed to AA. **Figure 5.4** investigates the effect of AA on a single apo-ferritin molecule, which lacks an iron core. The experiment involves trapping the apo-ferritin in the absence of ascorbic acid, followed by exposure to 5 mM AA solution in different time sets. We observed a subsequent increase in the RMS value of the transmission signal upon exposure. This change in RMS suggests fluctuations in the protein conformation, potentially due to the opening and closing of ferritin channels. We attribute this dynamic behaviour to the interaction between electron donors, such as superoxide anion ($O_2^{\bullet-}$) or ascorbate anion ($AscH^-$), previously reported, or ascorbate radical ($Asc^{\bullet-}$) (380), with the residues present within the ferritin channels (381). Notably, **Figure 5.4** demonstrates that these interactions can occur within the channels even when the iron core (Fe^{3+}) is absent.

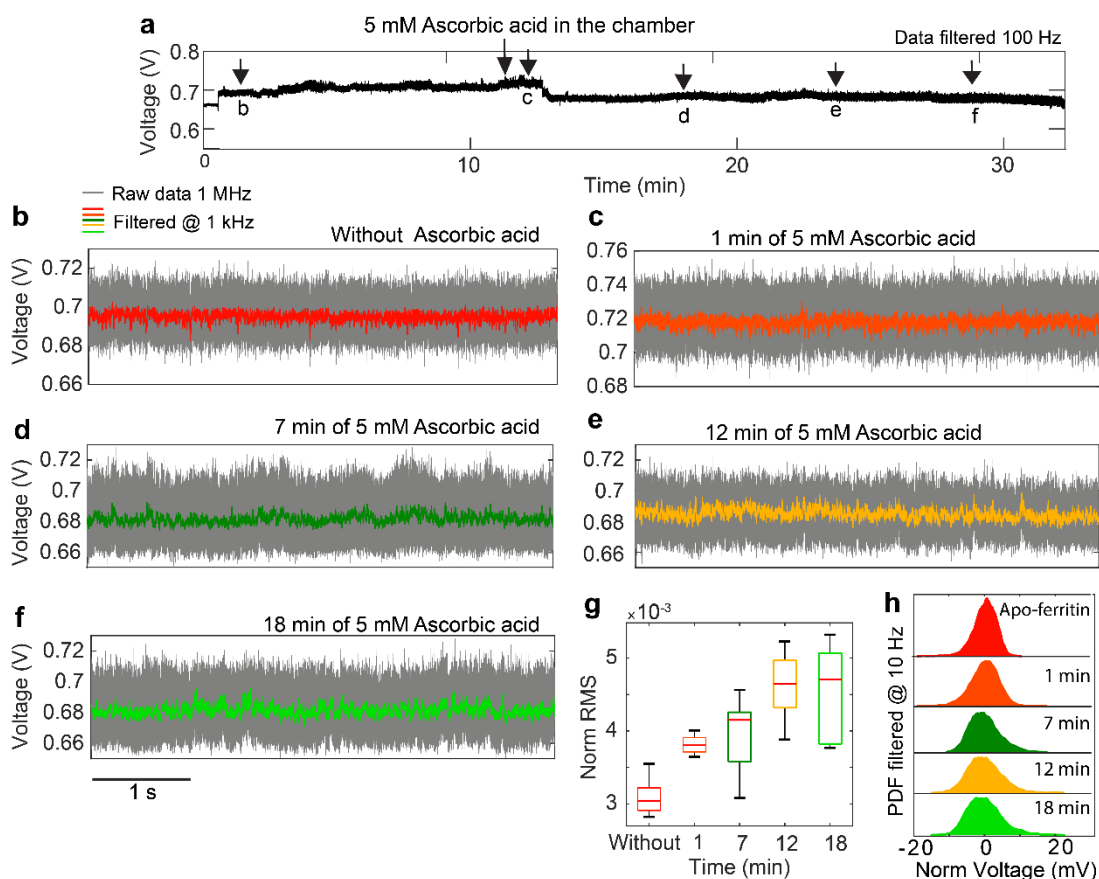


Figure 5.4: Effect of AA on single apo-ferritin (a) This panel presents the continuous transmission signal recorded during the trapping of a single apo-ferritin molecule within the hotspot of a DNH structure #5 (refer to **Figure 5.1** for the SEM image). The apo-ferritin, initially trapped within a phosphate buffer (PB) solution, is subsequently exposed to 5 mM ascorbic acid. (b-f) These panels display magnified selections (5 seconds each) of the transmission signal from panel (a). Each selection corresponds to a specific time point indicated within panel (a). (g) The normalised RMS values calculated for the transmission traces are presented in this panel. The RMS values were obtained for every 0.5-second segment of the traces shown in panels (b-f) after applying a digital filter with a 1 kHz cut-off frequency. The box plot illustrates the interquartile range, encompassing the 25th and 75th percentiles of the data. (h) This panel shows the PDF for the 5-second transmission traces presented in panels (b-f) after applying a Gaussian filter with a 10 Hz cut-off frequency. Adapted from (55). Copyright 2024 The Authors.

5.3.1 Impact of high AA concentration on the single ferritin transmission signal

Exposing ferritin to high AA concentrations (1.5 M) resulted in a strongly acidic solution ($\text{pH} \approx 2$) and triggered the disassembly of the protein (**Figure 5.5a**). This

disassembly process proceeded in a stepwise manner, with the complete escape from the trap taking approximately 12 minutes after high concentrations of AA solution arrived at the trapping site. Notably, the RMS value exhibited a simultaneous increase during this timeframe, potentially reflecting the unfolding of ferritin channels due to their destabilisation (**Figure 5.5b-d**). Furthermore, to explore the specific effects of an acidic environment on ferritin structure, we investigated the conformational dynamics of individual ferritin molecules subjected to controlled variations in pH within the trapping environment which we will discuss in following sections.

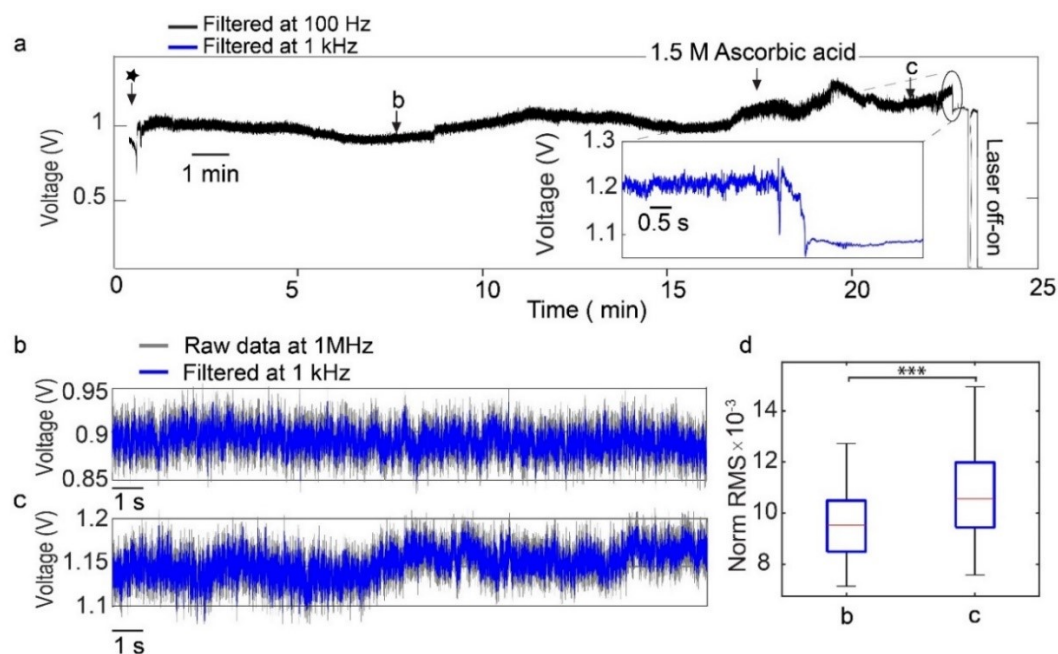


Figure 5.5: Disassembly of a single ferritin exposed to 1.5 M AA. (a) The trace highlights the trapping event for the ferritin molecule (marked by a star), subsequent exposure to 1.5 M ascorbic acid (indicated by an arrow), the disassembly process (magnified in the inset), and finally, the release of the ferritin upon laser deactivation. (b, c) These panels display magnified 20-second selections of the transmission signal from panel (a). Panel (b) focuses on the pre-exposure period (marked by the arrow), while panel (c) represents the behaviour during exposure to 1.5 M ascorbic acid. (d) This panel presents a boxplot depicting the normalised RMS values calculated for the 20-second transmission traces shown in panels (b) and (c) at 0.5-second intervals. Data acquisition was performed at a sampling frequency of 1 kHz. Asterisks indicate statistically significant differences between datasets (**p < 0.01, ***p < 0.0015). DNH Structure #2 used in this experiment (as depicted in **Figure 5.1**). Adapted from (55). Copyright 2024 The Authors.

5.4 Effect of acidic pH on the dynamic of single ferritin molecules

To clarify the influence of pH on ferritin dynamics, individual ferritin molecules were trapped at a neutral pH of 7.4. Subsequently, the surrounding environment was sequentially exposed to acidic solutions with decreasing pH values ranging from 6.0 to 2.0 (as depicted in the transmission traces of **Figures 5.6a, b**). The normalised RMS values calculated from the traces at pH 7.4 to 3.0 remained relatively stable, ranging between 0.005 and 0.01 (**Figure 5.6c**). This observation suggests a structurally stable conformation of ferritin within these solutions.

Ferritin is a protein complex composed of 24 subunits categorised as either heavy (H) or light (L) chains. The L-chains exhibit greater structural stability due to the presence of hydrogen bonds and salt bridges between subunits (367,382). Consistent with this, the equine spleen ferritin used in this study displayed a relatively stable structure at acidic pH values, likely attributable to the predominance of L-chain subunits (360,367,382). However, a significant increase in RMS (140%) was observed upon transitioning to a pH of 2.0 (**Figure 5.6c**). This dramatic rise indicates a substantial increase in protein dynamics in this acidic condition.

The observed mechanical instability of ferritin at pH 2.0 is thought to be a consequence of protein swelling, followed by monomer rotation and subsequent dimer movement within the 3-fold channels, ultimately leading to channel opening (324,367,383). As previously reported, this channel opening mechanism might facilitate the dissolution of the ferrihydrite core before disassembly (324,384,385).

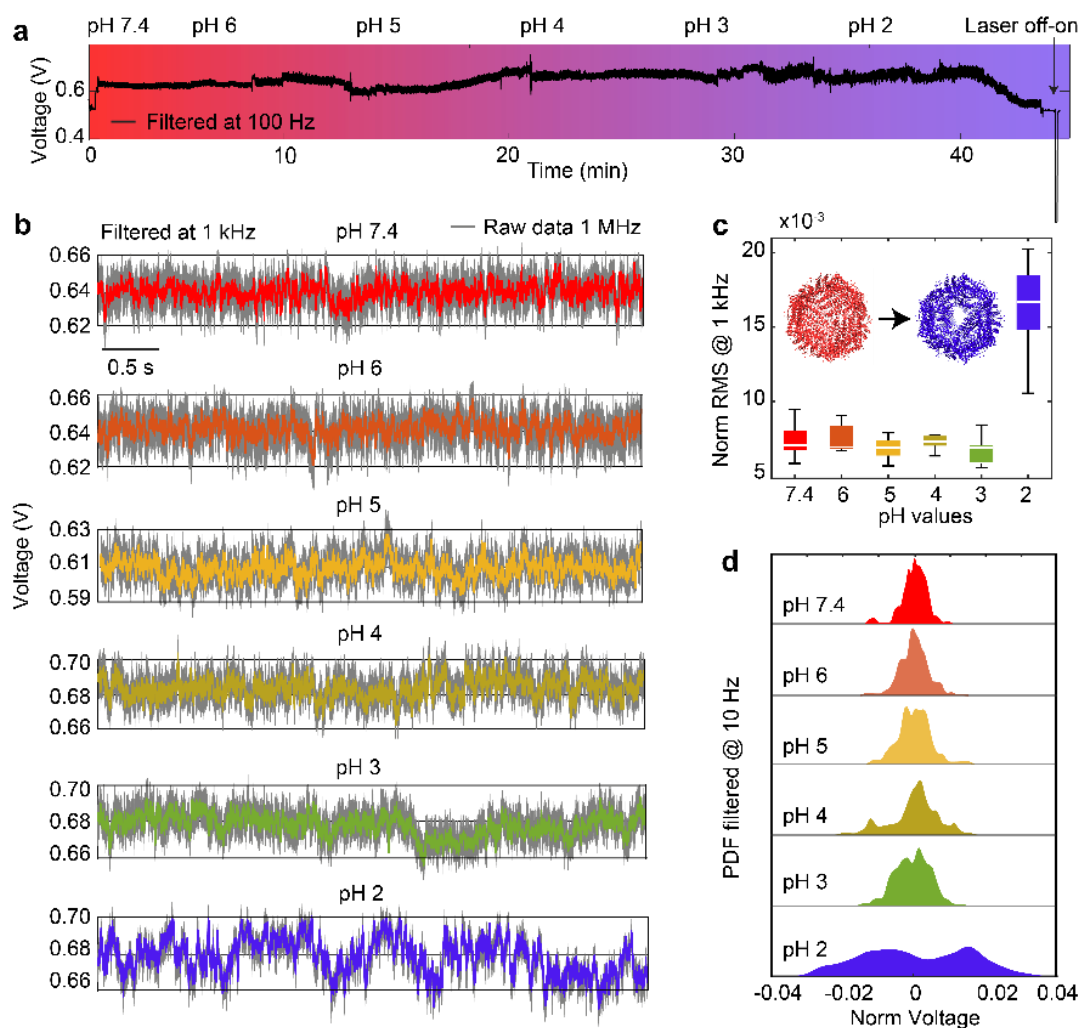


Figure 5.6: Conformational dynamics of a trapped ferritin under varying pH conditions (a) This panel presents a continuous transmission trace recorded during the experiment. The trace depicts a single ferritin molecule initially trapped at pH 7.4. Subsequently, solutions with progressively decreasing pH values (6.0, 5.0, 4.0, 3.0, and 2.0) were introduced sequentially at the trapping site. Notably, the transmission signal displayed a decrease in intensity over time following exposure to pH 2.0, eventually returning to baseline levels. (b) This panel showcases magnified 5-second segments of the transmission signal from panel (a). Each segment corresponds to a specific pH value (7.4, 6.0, 5.0, 4.0, 3.0, and 2.0) experienced by the trapped ferritin molecule in sequence. (c) The boxplots in this panel depict the interquartile range for the normalised RMS values calculated every 0.5 seconds from the 5-second traces shown in panel (b). The data were subjected to Gaussian filtering at a cut-off frequency of 1 kHz. The inset cartoon illustrates the hypothesised opening of the 3-fold channels within the ferritin structure upon exposure to the highly acidic environment (pH 2.0). Statistical significance testing revealed p-values less than 0.0001 ($p < 0.0001$) when comparing the normalised RMS at pH 2.0 with all other pH values. Comparisons between the remaining pH

values did not yield statistically significant differences. (d) This panel displays a PDF for the 5-second transmission traces presented in panel (b) after applying a Gaussian filter with a cut-off frequency of 10 Hz. The data were initially acquired at a sampling rate of 1 MHz and subsequently processed using Gaussian filters with cut-off frequencies of 1 kHz (panels b and c) or 10 Hz (panel d). DNH structure #1 (refer to **Figure 5.1** for the SEM image) was used for this experiment. Adapted from (55). Copyright 2024 The Authors.

5.5 Tracking disassembly kinetic and fragmentation of single ferritin molecules

Our approach tracks the complete disassembly kinetics of ferritin upon exposure to an acidic solution (pH 2.0) within the trapping chamber (**Figure 5.7a**). The stepwise reductions observed in the transmission signal (**Figure 5.7b**) directly correlate with the sequential dissociation of ferritin subunits. As this dissociation progresses, the molecular weight of the remaining protein fragment in the trap decreases, consequently affecting the transmission signal.

The transmission signal intensity in DNH structures is directly influenced by the trapped biomolecule's refractive index, which is in turn determined by the molecule's polarisability (386). Three key parameters contribute to the overall polarisability of a single protein: dielectric constant, volume, and shape (387). In this study, the ferritin subunits exhibit similar dielectric constants due to their predominant composition of L-chains (382,387). Additionally, assuming a uniform mass density for the oligomers, their volume scales linearly with their molecular weight. Furthermore, approximating the protein shape as spherical, a linear relationship is expected between the particle volume and the transmitted signal within DNH structures, as previously reported (268).

This linear relationship is further validated by the finite element method (FEM) simulation presented in **Figure 5.7c-d**. Consequently, our approach enables quantitative monitoring of the ferritin disassembly process. Spherical particles (with a refractive index of 1.8) with radii ranging from 1 to 8 nm in 1 nm intervals were positioned at the bottom of the DNH gap (**Figure 5.7c**). A plane-wave incidence along the z-axis at 852 nm was used as the light source, with the polarisation indicated by red arrows in **Figure 5.7c**. We consider the transmission value without the particle as the baseline (T_0). The relative transmission difference was calculated as $(T-T_0)/T_0$, where T is the transmission value for different spheres. **Figure 5.7d** demonstrates a

clear linear correlation between these parameters. This finding reinforces the reliability of our method in tracking the disassembly process by confirming the expected linear relationship between particle size and transmission signal within the DNH hotspot.

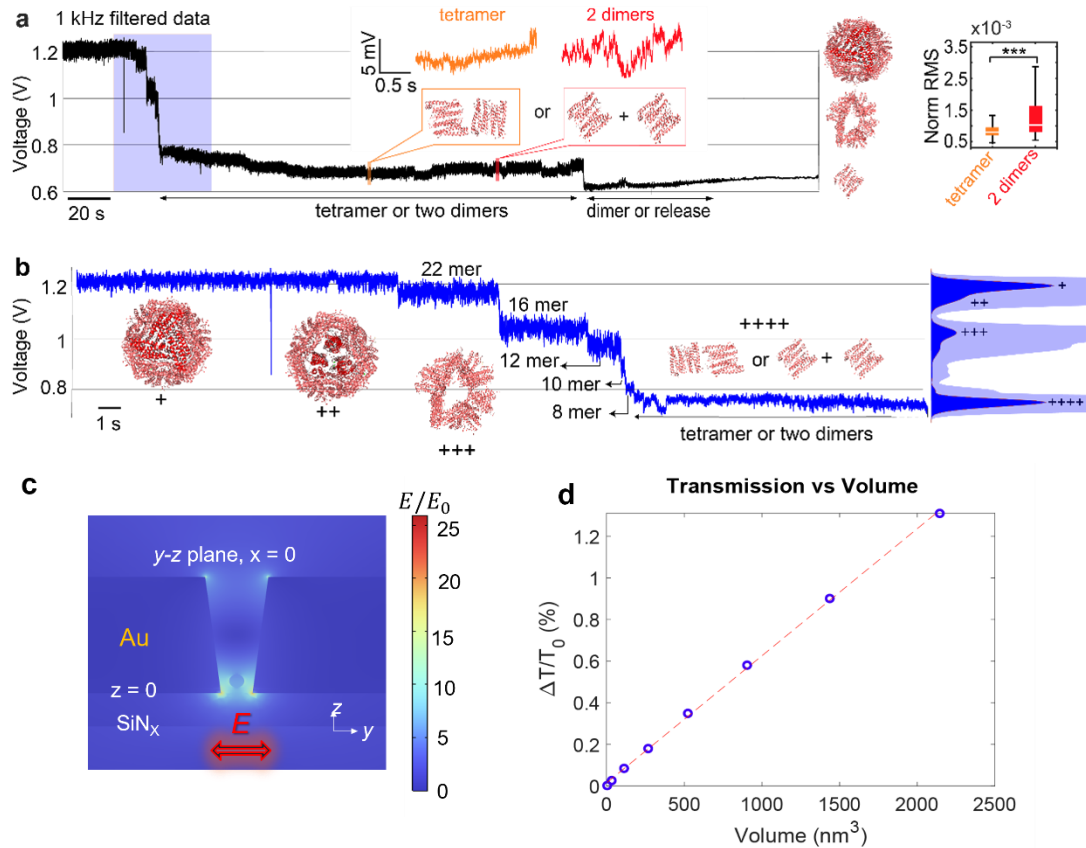


Figure 5.7: Disassembly kinetics of single ferritin molecules. (a) Continuous transmission trace depicting the complete disassembly of a single ferritin molecule upon exposure to pH 2.0. The trace exhibits distinct reductions in intensity, signifying sequential disassembly events. The insets show magnified segments potentially corresponding to the presence of a single tetramer (orange) or the co-existence of two dimers (red) within the trapping site. The normalised RMS values for these potential intermediates are displayed on the right, with asterisks indicating statistically significant differences compared to the baseline ($p < 0.005$). Crystal structures retrieved from the Protein Data Bank (PDB: 1IER) are included alongside the insets. These structures represent potential protein conformations corresponding to the observed transmission levels. (b) This panel provides a magnified view of the blue-shaded region in panel (a), focusing on the ferritin fragmentation process during disassembly. The "+" symbols highlight specific points in the trace that potentially correspond to remaining protein fragments, including 24-mer, 22-mer, 16-mer, and either a tetramer or two dimers. These potential disassembly stages are further supported by the peaks observed in the probability

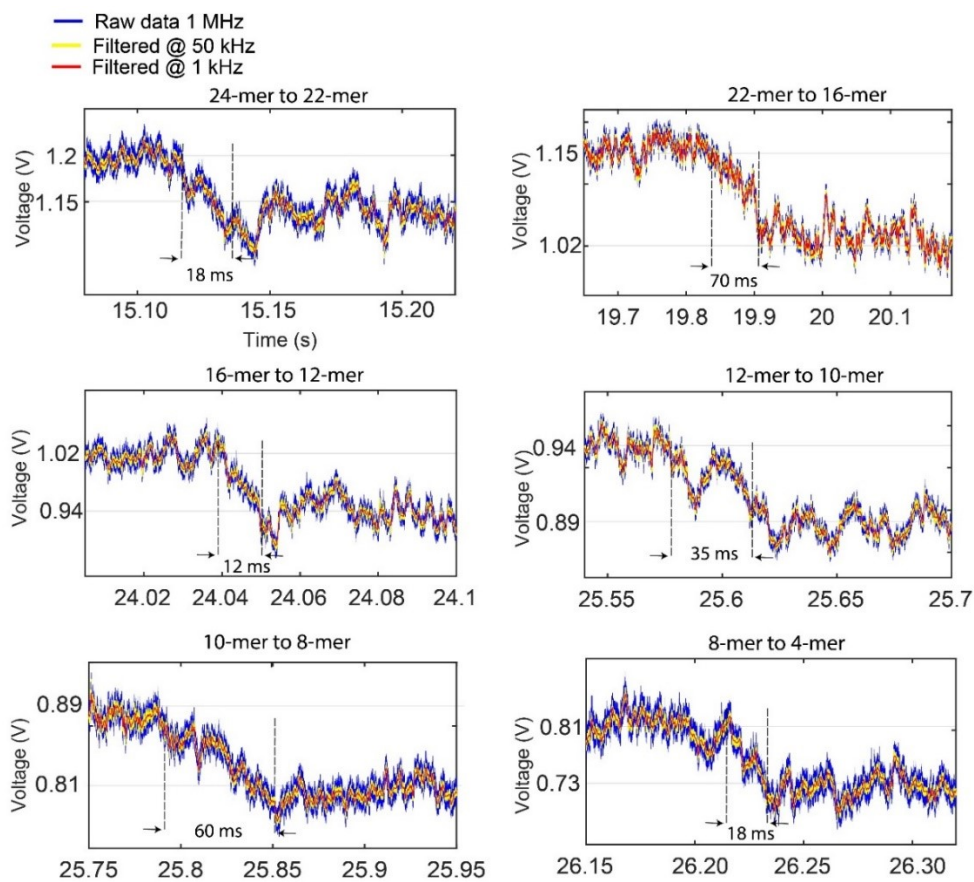
density function (PDF) on the right (with the magnified PDF region shown in transparent blue). DNH structure #2 (refer to **Figure 5.1** for the SEM image) was used for this experiment. (c) Simulation of the electric field enhancement distribution in the DNH structure in both the y-z and x-y planes, with a spherical particle of 1.8 refractive index and a 6 nm radius positioned in the DNH trap. (d) Illustration of the correlation between particle size (ranging from 1 nm to 8 nm in radius) and the transmission signal within the DNH hotspot. Adapted from (55).
Copyright 2024 The Authors

The maximum transmission intensity observed during the disassembly process ($V_{24\text{mer}}$) corresponds to the signal from a fully assembled ferritin molecule containing 24 subunits. Conversely, the transmission level at which the protein is released from the trap is denoted as V_{DNH} . To facilitate quantitative analysis, the transmission signal (APD signal) was linearly normalised. Here, the signal from trapped ferritin ($V_{24\text{mer}}$) was assigned a value of 100%, while the signal from the empty DNH structure (V_{DNH}) was set to 0%. Under the assumption of a spherical protein shape, each individual subunit is estimated to contribute approximately 4.17% to the overall optical signal. Based on this assumption, we correlated each distinct decrease in the APD signal with the dissociation of a specific number of subunits.

Table 5.1 summarises the obtained mean values of the APD signals for each plateau observed in **Figure 5.7**, along with their corresponding normalised values and the estimated number of remaining subunits. The initial drop in the signal by 10% suggests the dissociation of a dimer, leaving behind a 22-mer ferritin complex. This is followed by a series of reductions in the trapping signal – 30%, 45%, 70%, 80%, and 95-100% – attributed to the sequential dissociation of subunits, resulting in 16-mer, 12-mer, 8-mer, tetramer, and dimer forms, respectively. Disassembly steps were identified by analysing deviations from the mean value of the transmission signal, with zoomed-in views of these steps presented in **Figure 5.8**.

Table 5-1: Disassembly of single ferritin molecules when exposed to pH 2.0. Adapted from (55). Copyright 2024 The Authors.

V_{mean} (mV)	$\frac{V_{X\text{mer}} - V_{\text{DNH}}}{V_{24\text{mer}} - V_{\text{DNH}}}$	Ferritin Fragments
1200	100%	24-mer
1154	91%	22-mer
1024	68%	16-mer
943	53%	12-mer
890	44%	10-mer
810	29%	8-mer
730	16%	4-mer
611	7%	2-mer
645	0%	released

**Figure 5.8:** Disassembly stages of single ferritin at pH 2.0 (expanded view). This **Figure** presents magnified views of the disassembly trace observed for a single ferritin molecule upon

exposure to pH 2.0 (corresponding to the disassembly trace displayed in **Figure 5.7**). The grey horizontal lines indicate the mean transmission levels for each plateau identified in Table 1. The dashed vertical lines highlight the duration between the time point when the filtered (1 kHz) transmission signal deviates from the upper level and the time it reaches the lower level. The data are presented in three forms: raw (blue), digitally filtered at 50 kHz (yellow), and digitally filtered at 1 kHz (red). Adapted from (55). Copyright 2024 The Authors.

Figure 5.8 offers close-up views of the transitions between different steps as depicted in **Figure 5.7**. These transitions occur within a timescale of 12 ms to 70 ms. However, this transition time encompasses both the dissociation of the ferritin subunits and the departure of the smaller fragments from the trapping site, rather than solely reflecting the dissociation dynamics.

We observed that ferritin subunits primarily dissociate in units of single or multiple dimers. This behaviour can be attributed to the structural stability of the protein's 2-fold axis. The 24 subunits within a ferritin molecule interact through hydrogen bonds and electrostatic interactions, forming structures with 2-, 3-, and 4-fold symmetries. (367,388,389) Among these, the 2-fold axis exhibits the greatest stability due to the presence of the highest number of interaction sites. Conversely, the 3-fold axis, characterised by the fewest interaction sites, is the weakest point in the structure. (367,389) Consequently, the initial disassembly of ferritin is highly likely to occur within one of these 3-fold channels (367).

Out of five individual ferritin disassembly experiments, four displayed a characteristic stepwise disassembly signal (excluding one instance where the protein was suddenly released from the trap, detailed in **Figure 5.9**). These experiments are designated as Tests 1, 2, 3, and 4. Test 1 corresponds to the data presented in **Figure 5.7** and Table 5-1. The disassembly traces for Tests 2 and 3 are provided in **Figures 5.10** and **5.11**, respectively. Additionally, Test 4 investigates the disassembly process of apo-ferritin (ferritin without an iron core) at pH 2.0, with the corresponding transmission trace shown in **Figure 5.12**.

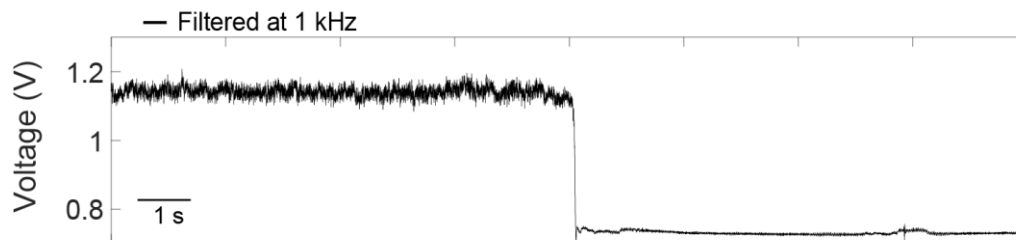


Figure 5.9: A trace of single ferritin disassembly when exposed to pH 2, exhibiting non-stepwise behaviour. Data was acquired at 1 MHz, with 1 kHz filtered data displayed in this Figure. (DNH structure #2 was used for this test, as shown in **Figure 5.1**). Adapted from (55). Copyright 2024 The Authors.

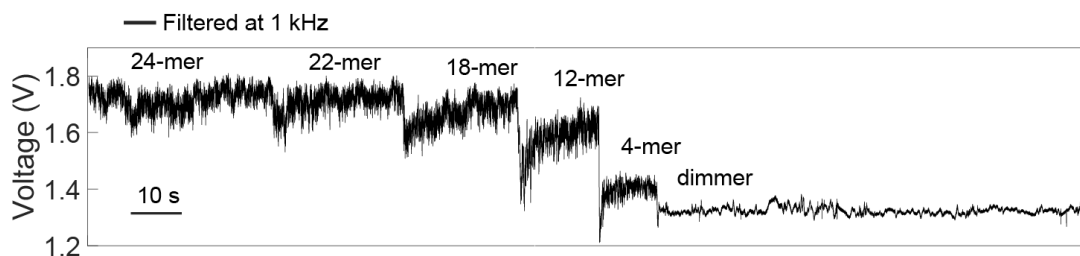


Figure 5.10: Complete trace of stepwise disassembly for test 2. Data was acquired at 1 MHz and filtered to 1 kHz. (DNH structure #3 was used for this test—refer to **Figure 5.1**). Adapted from (55). Copyright 2024 The Authors.

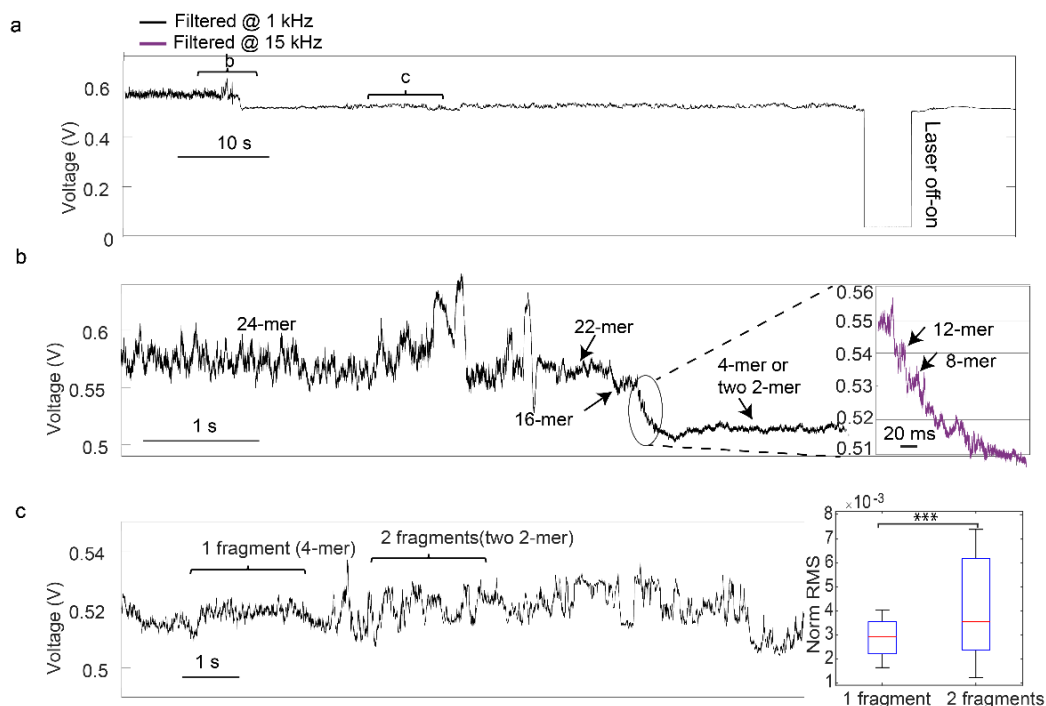


Figure 5.11: Disassembly trace of test 3. (a) The transmission trace illustrates the disassembly of ferritin at pH 2.0, including the process of turning off the laser to release the dimer fragments from the trap. (b) A magnified view of the ferritin disassembly highlights the distinct stepwise progression. The right panel provides an enlarged section of the trace, emphasising the disassembly steps. (c) An enlarged section of the transmission signal captures the moment when two dimer fragments are present in the DNH hotspot. The right panel shows the normalised RMS of the 2-second transmission segments marked in the trace, indicating the presence of one tetramer and two dimers in the trap. (DNH structure #4 was used for this test—refer to **Figure 5.1**). Adapted from (55). Copyright 2024 The Authors.

Figure 5.12 illustrates the effect of pH 2 on the disassembly of apo-ferritin (previous experiments in this chapter were on holo-ferritin). To enable a more detailed comparison, individual apo-ferritin molecules were trapped and exposed to the acidic environment of pH 2, revealing a stepwise disassembly pattern similar to that seen with holo-ferritin (**Figures 5.7, 5.10, and 5.11**). This disassembly process is attributed to protonation within the protein shell, which facilitates the dissociation of the structure (367). As depicted in **Figure 5.12b**, the 24-mer ferritin dissociates into 16-mer and 12-mer fragments. After reaching the 12-mer state, there is a sudden drop in the transmission signal (marked with an asterisk in **Figure 5.12b**). This decrease in the

transmission signal is likely due to a change in the shape of the 12-mer ferritin fragments, which affects the molecule's polarisability and thus alters the transmission signal. Despite this change, the fragments appear to revert to their original conformation before ultimately breaking down into even smaller subunits.

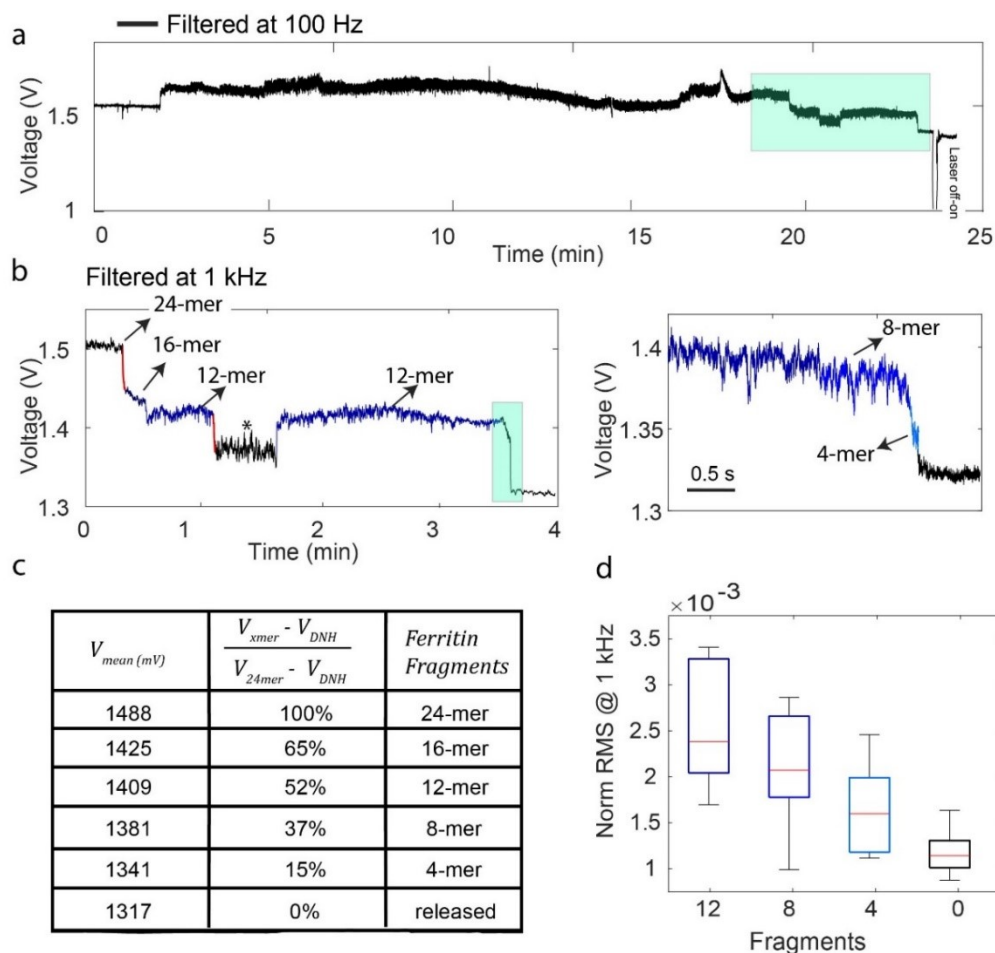


Figure 5.12: Exposure of Single apo-ferritin to pH 2. (a) The transmission trace captures the behaviour of a DNH structure with an apo-ferritin protein initially trapped at pH 7.4, which is then subjected to an acidic environment of pH 2. The gradual decrease in the transmission signal over time signifies the protein's disassembly process. (b) The highlighted segment in panel (a) demonstrates the step-by-step disassembly of the 24-mer apo-ferritin into smaller fragments. The right panel zooms in on one of the disassembly steps highlighted on the left. (c) The table lists the average values of the disassembly steps and the ferritin fragments that remained within the DNH trap. (d) The normalised RMS values, associated with the disassembly stages from the 12-mer state to when the DNH is empty, are presented. The data, filtered using a Gaussian filter at 1 kHz, includes the 25th and 75th percentiles. (DNH structure #3 was utilised for this test—refer to **Figure 5.1**). Adapted from (55). Copyright 2024 The Authors.

All four transmission traces exhibit distinct reductions in signal intensity upon exposure to pH 2.0, followed by complete protein release reflected by a return to baseline levels.

Figure 5.13a uses Equation 5-5 to estimate the number of remaining subunits based on the observed transmission level during the disassembly process, as described previously.

$$i = \frac{V_{Xmer} - V_{DNH}}{V_{24mer} - V_{DNH}} \quad 5-5$$

The high sensitivity of optical nanotweezers allows for the high resolution of the ferritin disassembly pathway, revealing the formation of distinct intermediate fragments (**Figure 5.13a**). This level of detail surpasses the capabilities of other single-molecule techniques. Our observations consistently demonstrate that holo-ferritin disassembly initiates with the dissociation of a single dimer, resulting in a 22-mer intermediate trapped within the optical nanotweezers. Notably, the 22-mer fragment can further dissociate into various smaller structures during the disassembly process. Despite the observed variability in the fragmentation pathways across three independent holo-ferritin disassembly experiments (tests 1-3), specific subunit assemblies (22-mer, 12-mer, 4-mer, and 2-mer) consistently maintain their structural integrity throughout the disassembly process, as highlighted in **Figure 5.13a**.

It is crucial to mention that the above analysis relies on the assumption that the oligomers possess a spherical shape. However, anisotropic (non-spherical) shapes can lead to a greater change in transmission compared to their spherical counterparts (268). In **Figure 5.13a**, lines were drawn connecting the 24-mer state to the 0-mer state for each of the four datasets. While the majority of data points closely follow these lines, there are slight deviations observed, with some points falling above the linear trend. These somewhat higher transmission values might be attributed to the anisotropic shape of the disassembled fragments. An anisotropic shape could lead to a higher overall polarisability compared to a perfect sphere, potentially explaining the observed deviations.

The normalised RMS values presented in **Figure 5.13b**, show the transition from 12-mer structures to the release of disassembled fragments, aligning with previous studies

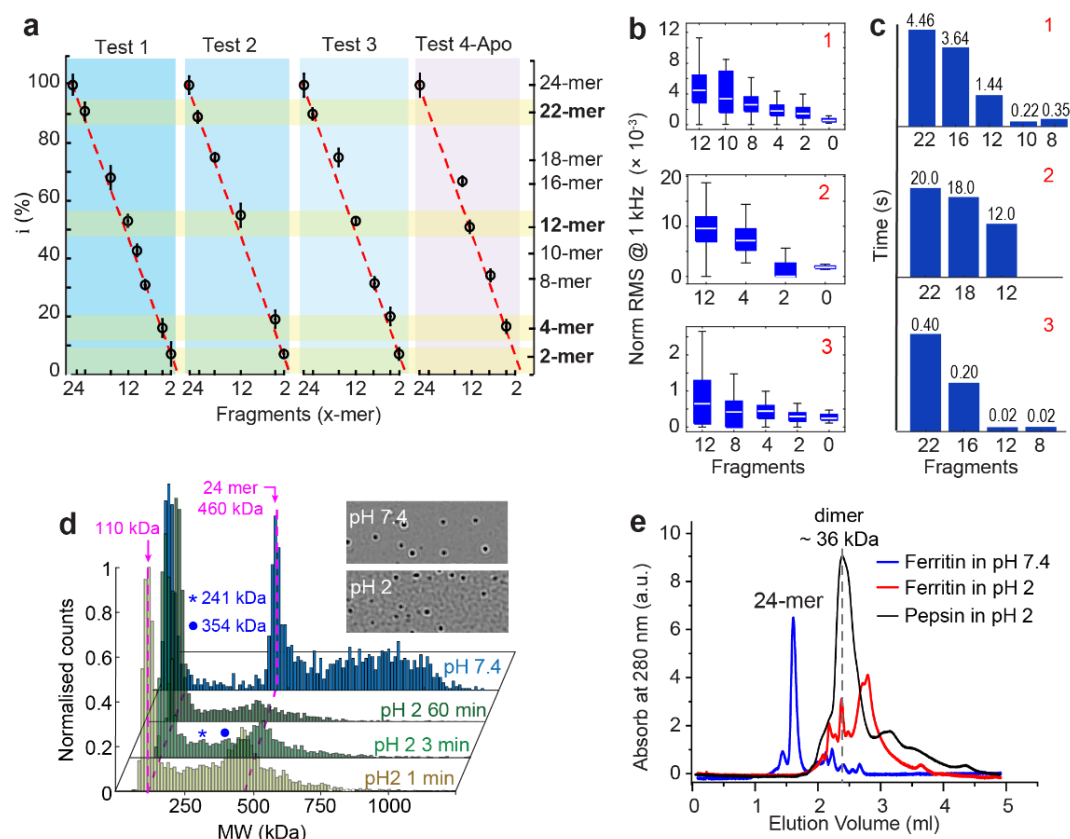


Figure 5.13: Kinetic analysis of single ferritin molecule disassembly. (a) Estimated number of remaining subunits within the trap during disassembly across four experiments: three for holo-ferritin (tests 1-3) and one for apo-ferritin (test 4). The number of subunits at each stage was calculated using Equation 5 from the manuscript, with red dashed lines connecting the 24-mer state (100% transmission) and the 0-mer state (0% transmission). (b) This panel presents the normalised RMS values for the disassembly steps observed in the three holo-ferritin experiments (tests 1-3), covering the transition from the 12-mer fragment stage to the point of protein release from the trap. (c) The dwelling time of individual subunits within the trap is shown for tests 1-3 (holo-ferritin disassembly), excluding tetramer and dimer data due to the potential coexistence of dimers from tetramer dissociation. (d) This panel displays mass photometry (MP) results for ferritin at pH 2.0 at 1, 3, and 60 minutes, along with a reference measurement at pH 7.4. The PDF is normalised to the maximum count for a fair comparison. The asterisk and circles highlight the disappearance of intermediate subunit peaks at pH 2.0. Sample interferometric contrast images for ferritin at both pH 7.4 and pH 2.0 are provided on the same contrast scale, with a field of view of $10.8 \times 6.8 \mu\text{m}$. See **Figure 5.14a** for MP graphs related to buffer (pH 7.4) with and without ferritin (e) Size-exclusion chromatography (SEC) results are shown for ferritin at pH 7.4 (blue), pH 2.0 (red), and pepsin at pH 2.0 (black) for comparison, with peak positions of protein markers in pH 7.4. See **Figure 5.14b** for the peak positions of protein markers in pH 7.4. Adapted from (55). Copyright 2024 The Authors.

demonstrating that the RMS value of the transmission trace decreases as the size of trapped globular proteins reduces (386). Interestingly, our observations suggest that smaller fragments exit the trap immediately following their disassembly. This is supported by the consistent RMS values within each transmission level. If two fragments were to co-exist within the trapping site, their Brownian motion would introduce additional noise into the transmission trace compared to that observed for a single entity. However, except for tetramers (or potentially two co-existing dimers), we did not detect instances of two fragments simultaneously residing within the trap. Tetramers, or pairs of dimers, exhibit identical sizes, and their presence can indeed lead to a noticeable increase in noise within the transmission trace, as exemplified in **Figure 5.7a** and **Figure 5.11c**.

The high RMS value observed for the 12-mer fragment can be attributed to its large accessible surface areas at subunit interfaces. These extensive interfaces result in a reduced number of hydrogen bonds formed by inter-dimer interactions, as reported previously (383). While prior investigations into ferritin disassembly and assembly kinetics have utilised techniques such as circular dichroism with SAXS and native PAGE (390–392), these methods primarily focused on bulk measurements. Disassembly kinetics at the single-molecule level remained largely unexplored. The application of optical tweezers offers the unique advantage of resolving the dwell time of each subunit during disassembly, with a sensitivity reaching millisecond timescales (**Figure 5.13c**). Our observations unveil a cooperative disassembly process, where the disassembly of individual subunits facilitates and accelerates the overall disassembly of the entire structure. This cooperative mechanism has been previously supported by simulation studies (393). It is important to note that the dwell time measurements for tetramers and dimers may not be entirely accurate. Tetramers can dissociate into two dimers, and these fragments might coexist within the trap, as illustrated in **Figure 5.13a**.

To further validate our findings on single-molecule ferritin fragmentation at pH 2, we employed mass photometry (MP) as a complementary single-molecule approach. The results are presented in **Figure 5.13d**.

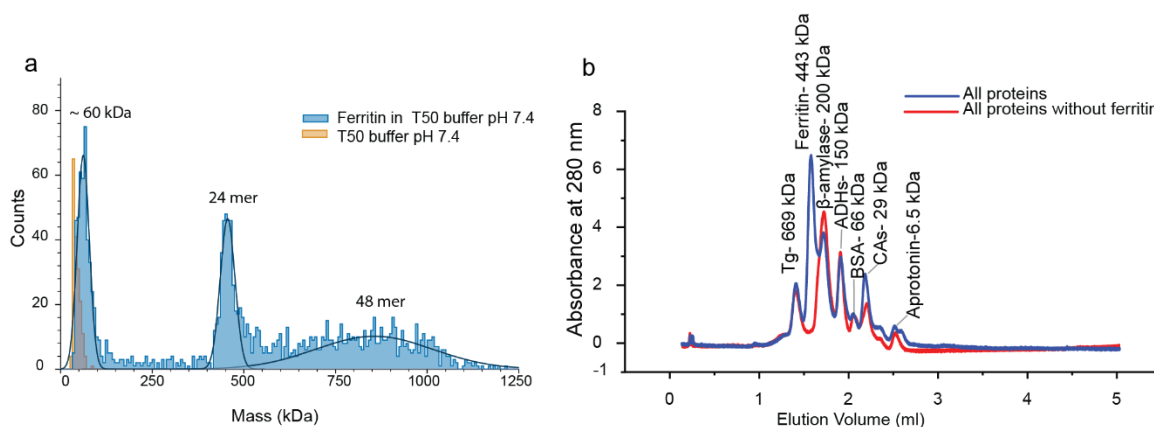


Figure 5.14: Mass photometry analysis of ferritin at buffer pH 7.4 and FPLC profiles of protein markers. (a) MP of T50 buffer pH 7.4 with and without 50 nM ferritin (b) FPLC chromatograms of protein markers with ferritin (blue) and without ferritin (red) were used to verify the peak position of ferritin. Adapted from (55). Copyright 2024 The Authors.

At a neutral pH (pH 7.4), the ferritin population primarily exhibited a mass of approximately 460 kDa, consistent with the fully assembled 24-mer structure. However, a minor population of small fragments around 60 kDa was also observed. The presence of these fragments is potentially attributable to minor impurities within the protein sample, which aligns with the Fast Protein Liquid Chromatography (FPLC) data presented in **Figure 5.13e** (blue trace).

In contrast, at pH 2.0, the dominant peak in the MP data shifted to a lower mass, approximately 110 kDa. Additionally, two intermediate mass species were identified in the ferritin sample at pH 2.0, potentially corresponding to 12-mer (marked with an asterisk) and 18-mer (marked with a circle) intermediates. These intermediate fragments showed a decrease in abundance with extended exposure of ferritin to pH 2.0, further supporting our observations of a stepwise disassembly process.

While MP offers valuable insights into the impact of acidic pH on the mass of ferritin fragments, it is limited in its ability to provide details on the dynamic behaviour and dwell time of individual subunits during the disassembly process. Furthermore, as shown in **Figure 5.13e**, the technique cannot resolve the presence of tetrameric and dimeric states of ferritin at lower molecular weights. This limitation stems from the inherent technical limits of the instrument when operating under extreme conditions such as low pH. However, by using FPLC, we confirmed the presence of the dimeric

state of ferritin at pH 2.0 (36 kDa) by its co-elution with pepsin, a stable protein at pH 2.0 with a molecular weight of 35 kDa (**Figure 5.13e**).

5.6 Conclusion

This study employed optical nanotweezers with DNH and microfluidic to investigate the behaviour of single ferritin molecules in situ under varying conditions of ascorbic acid concentration and acidic pH. At the single-molecule level, we observed a gradual increase in ferritin dynamics as the concentration of ascorbic acid increased, reaching a saturation point at 5 mM. This suggests a higher rate of Fe^{3+} reduction to Fe^{2+} within the ferritin core at this concentration. Exposure to a highly acidic environment (pH 2.0) resulted in significant structural fluctuations in both ferritin and apo-ferritin. These changes are likely due to protein swelling and protonation of hydrogen bonds, ultimately leading to disassembly. We were able to identify the number of subunits present during the disassembly pathway and highlight the most consistently observed fragments: 22-mer, 12-mer, 4-mer, and 2-mer. Notably, the 12-mer fragment exhibited the highest level of protein dynamics among all observed subunits.

Furthermore, this study provides insights into the kinetic parameters of single ferritin disassembly at acidic pH, revealing a cooperative disassembly process. These single-molecule findings offer valuable knowledge for the potential engineering of ferritin structures to achieve desired functionalities, such as in the design of molecular machines and drug delivery platforms (394,395). Additionally, this work highlights the quantitative analytical potential of optical nanotweezers in biomolecule analysis. This capability extends to a wide range of protein applications in future research and paves the way for the application of other single-molecule techniques, including solid-state nanopores and atomic force microscopy (AFM), in the investigation of ferritin (323,396).

Chapter 6: Thesis summary and future work

6.1 Thesis summary

In this thesis, the use of optical nanotweezers is presented as a single-molecule approach to study proteins, specifically single ferritin molecules. The study begins by introducing single-molecule techniques, highlighting their importance and potential impact on the understanding of protein dynamics. Unlike ensemble measurements, which average the behaviour of many molecules, single-molecule techniques allow for the observation of detailed dynamics and interactions of individual molecules, providing deeper insights into their conformational changes and functions.

In Chapter 2, I explored the literature related to various optical-based single-molecule approaches for studying proteins. We discussed several techniques, including smFRET, single-molecule Raman spectroscopy, iSCAT and mass photometry, optical tweezers, whispering gallery mode single-molecule techniques, and plasmonic optical tweezers (optical nanotweezers). For each method, we explored their advantages and disadvantages and how they have advanced our understanding of the dynamic and conformational behaviour of single proteins. By comparing these techniques, I demonstrated the unique capabilities of optical nanotweezers in providing precise manipulation and measurement at the single-molecule level, paving the way for significant advancements in molecular biology and biophysics.

In Chapter 3, I detailed the methodology used in our study of single ferritin molecules with optical nanotweezers. The chapter begins with an overview of the nanostructure fabrication techniques I used during my PhD, including electron beam lithography (EBL) for creating silicon nanostructures and focused ion beam (FIB) techniques for fabricating DNH structures. I provided a thorough account of the fabrication steps involved in each technique, along with an explanation of the simulation methods used to model the DNH structures and assess field enhancement across varying gap sizes.

Following this, I discussed the characterisation processes, which included the optical setup integrated with microfluidic systems and the analysis of single ferritin trapping events. The chapter also covers the impact of laser irradiation on the DNH structures, other protein characterisation techniques such as size-exclusion chromatography (SEC) and mass photometry (MP) and concludes with an explanation of the data analysis methods used in this thesis.

Chapter 4 explored the dynamic differences between individual, unlabelled apo-ferritin and holo-ferritin molecules using an optical nanotweezer system. This approach allowed for the crucial differentiation of apo- and holo-ferritin at the single-molecule level and enabled the label-free monitoring of a single apo-ferritin molecule converting into holo-ferritin in real-time. Detailed analysis identified key parameters for discrimination based on the optical trapping signals from the same DNH structure when trapping different protein forms. The RMS of the trapping signal indicated that holo-ferritin had a lower RMS, reflecting its inherent structural stability. Additionally, the transmission signal change was significantly larger (41%) for holo-ferritin compared to apo-ferritin, due to the higher polarisability of holo-ferritin.

The chapter further presented the first experimental evidence for the *in situ* loading of iron into a single, unmodified apo-ferritin molecule. By carefully analysing the transmission signals, researchers tracked the dynamic structural changes of ferritin related to the gating behaviour of its three-fold channels. These channels underwent cycles of unfolding ("on") and folding ("off"), allowing Fe^{2+} ions to enter the ferroxidase centres and facilitating the subsequent transfer of Fe^{3+} ions to the protein core. The significance of this study lies in its potential to enable precise control of protein cages for targeted drug delivery within living systems and the encapsulation of metal nanoparticles.

Chapter 5 examined the behaviour of single ferritin molecules *in situ* under varying conditions of ascorbic acid concentration and acidic pH using optical nanotweezers with DNH and a microfluidic setup. At the single-molecule level, we observed a gradual increase in ferritin dynamics as the concentration of ascorbic acid increased, reaching a saturation point at 5 mM. This indicated a higher rate of Fe^{3+} reduction to Fe^{2+} within the ferritin core at this concentration. Exposure to a highly acidic environment (pH 2.0) caused significant structural fluctuations in both holo-ferritin

and apo-ferritin, likely due to protein swelling and protonation of hydrogen bonds, ultimately leading to disassembly.

We identified the number of subunits present during the disassembly pathway and highlighted the most consistently observed fragments: 22-mer, 12-mer, 4-mer, and 2-mer. The 12-mer fragment exhibited the highest level of protein dynamics among all observed subunits. This study also provided insights into the kinetic parameters of single ferritin disassembly at acidic pH, revealing a cooperative disassembly process.

The impact of this study lies in its potential to enhance the design of ferritin-based drug delivery systems. Understanding the disassembly kinetics at the single-molecule level is crucial for engineering ferritin structures with desired functionalities. Additionally, this work highlighted the quantitative analytical potential of optical nanotweezers in biomolecule analysis, offering valuable knowledge for the development of molecular machines and other advanced applications.

6.2 Future work

There are several challenges in using optical nanotweezers as a single-molecule technique and addressing these challenges could significantly advance the field of single-molecule science and serve as important paths for future research. Key issues include the heating effects caused by plasmonic nanostructures, surface interactions with the molecules under study, and the challenge of analysing a diverse range of molecules.

In this thesis, we used plasmonic DNH structures to trap single proteins. However, the high absorption of metallic structures like gold at visible and near-infrared ranges causes significant heating, impacting protein studies (79). Heat and plasmonic absorption can disrupt the function of biological samples such as enzymes, membrane proteins, signalling proteins, and antibodies, all of which are sensitive to temperature changes (397–399). This sensitivity can compromise their binding affinity and specificity, affecting experimental accuracy and reliability (397–399). To minimise heat effects, new optical nanotweezer designs with reduced optical absorption are necessary.

In response to the challenges associated with traditional plasmonics, recent advances have emerged in an alternative nano-optics approach using subwavelength, high

refractive index dielectric nanostructures, known as all-dielectric nanoantennas. These devices generate near-field hotspots with significantly lower absorption losses compared to conventional plasmonics (103,279).

Recent studies have shown significant progress in this field, including the trapping of polystyrene particles ranging from 20 to 100 nm using all-silicon nanoantennas (400), trapping small particles such as quantum dots (401), or on simulations proposing the trapping of viruses (402). However, there is a gap in using these techniques to study proteins in real conditions and to understand them at the single-molecule level.

Several challenges remain in achieving this goal. The local field enhancement generated by dielectric antenna structures is generally weaker than that produced by metal plasmonic structures (400). While high-throughput designs, such as multi-ring structures, have been proposed and simulated to achieve significant field enhancement in dielectric systems, these designs have yet to be realised experimentally (400). Another challenge is variations in design parameters which can affect the target resonance wavelength. Consequently, trapping small molecules may not occur due to fabrication defects. In the future, the goal should be to reduce this sensitivity to fabrication defects and develop dielectric nanostructures for optical trapping that are robust.

Additionally, the development of hybrid nanostructures, specifically dielectric-plasmonic nanostructures, is a promising idea. Recent simulations suggest that field enhancement using plasmonic nanoantenna-dielectric nanocavity hybrids can achieve an order of magnitude higher field enhancement in the gap compared to individual antennas (403).

Optical nanotweezers have mainly been used to trap globular proteins, but extending their application to a wider range of protein types could provide significant insights in protein structure and biology science. To achieve this, several steps are necessary: designing nanoaperture structures to improve field localisation and interaction strength for various proteins, adapting the size and spacing of the nanoholes to suit different protein shapes and sizes; functionalising the surfaces of the nanostructures with specific chemical or biological coatings to enhance selectivity and reduce nonspecific binding; optimising experimental conditions such as pH and ionic strength to better mimic the physiological environment of the target proteins; and incorporating

advanced detection methods like fluorescence or Raman spectroscopy to enhance sensitivity of the system to fast protein movements and obtain more detailed information about protein behaviour and interactions. By addressing these factors, optical nanotweezers could be adapted to trap and analyse a broader spectrum of proteins, offering new opportunities for research in molecular biology and biophysics.

Finally, in the field of single-molecule protein detection, it is crucial to use various approaches to ensure the reliability of studies. Investigating proteins from multiple single-molecule perspectives provides a comprehensive understanding by looking at the problem from different angles. Since these techniques are currently limited to laboratory settings and are often expensive, efforts should be made to reduce costs and increase accessibility for researchers. Making these advanced single-molecule detection technologies more available will facilitate broader research opportunities and speed up scientific discoveries.

References

1. Easterling LF, Yerabolu R, Kumar R, Alzarieni KZ, Kenttämaa HI. Factors Affecting the Limit of Detection for HPLC/Tandem Mass Spectrometry Experiments Based on Gas-Phase Ion-Molecule Reactions. *Anal Chem.* 2020;92(11).
2. Lerner E, Cordes T, Ingargiola A, Alhadid Y, Chung SY, Michalet X, et al. Toward dynamic structural biology: Two decades of single-molecule Förster resonance energy transfer. Vol. 359, *Science.* 2018.
3. Neuman KC, Lionnet T, Allemand JF. Single-molecule micromanipulation techniques. Vol. 37, *Annual Review of Materials Research.* 2007.
4. Armstrong RE, Horáček M, Zijlstra P. Plasmonic Assemblies for Real-Time Single-Molecule Biosensing. Vol. 16, *Small.* 2020.
5. Gooding JJ, Gaus K. Single-Molecule Sensors: Challenges and Opportunities for Quantitative Analysis. Vol. 55, *Angewandte Chemie - International Edition.* 2016.
6. Kumari S, Roy S, Singh P, Singla-Pareek SL, Pareek A. Cyclophilins: Proteins in search of function. Vol. 8, *Plant Signaling and Behavior.* 2013.
7. Nguyen TN, Goodrich JA. Protein-protein interaction assays: Eliminating false positive interactions. *Nat Methods.* 2006;3(2).
8. Seroz T, Hwang JR, Moncollin V, Egly JM. TFIIH: a link between transcription, DNA repair and cell cycle regulation. *Curr Opin Genet Dev.* 1995;5(2).
9. Shugar D. Dynamics of proteins and nucleic acids. *FEBS Lett.* 1989;253(1–2).
10. Grant BJ, Gorfe AA, McCammon JA. Large conformational changes in proteins: Signaling and other functions. Vol. 20, *Current Opinion in Structural Biology.* 2010.
11. Hartl FU. Protein Misfolding Diseases. *Annu Rev Biochem* [Internet]. 2017;86(1):21–6. Available from: <https://doi.org/10.1146/annurev-biochem-061516-044518>
12. Thakur G, Jiang K, Lee D, Prashanthi K, Kim S, Thundat T. Investigation of pH-induced protein conformation changes by nanomechanical deflection. *Langmuir.* 2014;30(8).
13. Olson KM, Campbell A, Alt A, Traynor JR. Finding the Perfect Fit: Conformational Biosensors to Determine the Efficacy of GPCR Ligands. Vol. 5, *ACS Pharmacology and Translational Science.* 2022.

References

14. Nguyen M Van, Thorarinsdottir KA, Gudmundsdottir A, Thorkelsson G, Arason S. The effects of salt concentration on conformational changes in cod (*Gadus morhua*) proteins during brine salting. *Food Chem.* 2011;125(3).
15. Shaw DE, Maragakis P, Lindorff-Larsen K, Piana S, Dror RO, Eastwood MP, et al. Atomic-level characterization of the structural dynamics of proteins. *Science* (1979). 2010;330(6002).
16. Henzler-Wildman K, Kern D. Dynamic personalities of proteins. Vol. 450, *Nature.* 2007.
17. Frauenfelder H, Fenimore PW, Young RD. Protein dynamics and function: Insights from the energy landscape and solvent slaving. Vol. 59, *IUBMB Life.* 2007.
18. Mazal H, Haran G. Single-molecule FRET methods to study the dynamics of proteins at work. Vol. 12, *Current Opinion in Biomedical Engineering.* 2019.
19. Maveyraud L, Mourey L. Protein X-ray crystallography and drug discovery. Vol. 25, *Molecules.* 2020.
20. Atkinson RA. NMR of proteins and nucleic acids. *Nuclear Magnetic Resonance.* 2021;46.
21. Minor W, Dauter Z, Jaskolski M. The young person's guide to the PDB. Vol. 62, *Postepy biochemii.* 2016.
22. Liu Z, Zhang C, Zhang Q, Zhang Y, Yu DJ. TM-search: An Efficient and Effective Tool for Protein Structure Database Search. *J Chem Inf Model.* 2024;64(3).
23. Raskatov JA, Teplow DB. Using chirality to probe the conformational dynamics and assembly of intrinsically disordered amyloid proteins. *Sci Rep.* 2017;7(1).
24. Wang X, Guerrand L, Wu B, Li X, Boldon L, Chen WR, et al. Characterizations of polyamidoamine dendrimers with scattering techniques. Vol. 4, *Polymers.* 2012.
25. Sharon M, Robinson C V. The role of mass spectrometry in structure elucidation of dynamic protein complexes. Vol. 76, *Annual Review of Biochemistry.* 2007.
26. Fang S, Hu YH. Open the door to the atomic world by single-molecule atomic force microscopy. Vol. 4, *Matter.* 2021.
27. Bustamante CJ, Chemla YR, Liu S, Wang MD. Optical tweezers in single-molecule biophysics. Vol. 1, *Nature Reviews Methods Primers.* 2021.
28. Sarkar R, Rybenkov V V. A guide to magnetic tweezers and their applications. Vol. 4, *Frontiers in Physics.* 2016.

29. Mandal SS. Force Spectroscopy on Single Molecules of Life. ACS Omega [Internet]. 2020;5(20):11271–8. Available from: <https://pubs.acs.org/doi/10.1021/acsomega.0c00814>
30. Sluysmans D, Devaux F, Bruns CJ, Fraser Stoddart J, Duwez AS. Dynamic force spectroscopy of synthetic oligorotaxane foldamers. Proc Natl Acad Sci U S A. 2018;115(38).
31. Woodside MT, Block SM. Reconstructing folding energy landscapes by single-molecule force spectroscopy. Annu Rev Biophys. 2014;43(1).
32. Camunas-Soler J, Ribezzi-Crivellari M, Ritort F. Elastic Properties of Nucleic Acids by Single-Molecule Force Spectroscopy. Vol. 45, Annual Review of Biophysics. 2016.
33. Dey S, Dolci M, Zijlstra P. Single-Molecule Optical Biosensing: Recent Advances and Future Challenges. Vol. 3, ACS Physical Chemistry Au. 2023.
34. Hutter H. Fluorescent Protein Methods: Strategies and Applications. In: Methods in Cell Biology. 2012.
35. Mauriz E, Lechuga LM. Plasmonic biosensors for single-molecule biomedical analysis. Biosensors (Basel). 2021;11(4).
36. Chen Y, Bai X, Su L, Du Z, Shen A, Materny A, et al. Combined Labelled and Label-free SERS Probes for Triplex Three-dimensional Cellular Imaging. Sci Rep. 2016;6.
37. Moerner WE, Fromm DP. Methods of single-molecule fluorescence spectroscopy and microscopy. Review of Scientific Instruments [Internet]. 2003;74(8):3597–619. Available from: <https://doi.org/10.1063/1.1589587>
38. Lockwood DJ, Bowen W, Vollmer F, Gordon R. Single Molecule Sensing Beyond Fluorescence [Internet]. Available from: <https://link.springer.com/bookseries/6331>
39. Beutner EH. IMMUNOFLUORESCENT STAINING: THE FLUORESCENT ANTIBODY METHOD. Bacteriol Rev. 1961;25(1).
40. Im K, Mareninov S, Diaz MFP, Yong WH. An introduction to performing immunofluorescence staining. In: Methods in Molecular Biology. 2019.
41. Cai B, Yu L, Sharum SR, Zhang K, Diao J. Single-vesicle measurement of protein-induced membrane tethering. Colloids Surf B Biointerfaces. 2019;177.
42. Taniguchi Y, Kawakami M. Application of Halotag protein to covalent immobilization of recombinant proteins for single molecule force spectroscopy. Langmuir. 2010;26(13).

43. Maciuba K, Zhang F, Kaiser CM. Facile tethering of stable and unstable proteins for optical tweezers experiments. *Biophys J*. 2021;120(13).
44. Eisenberg-Bord M, Shai N, Schuldiner M, Bohnert M. A Tether Is a Tether Is a Tether: Tethering at Membrane Contact Sites. Vol. 39, *Developmental Cell*. 2016.
45. Song D, Mousley B, Gambino S, Helou E, Loparo J, Price AC. Tethered particle motion with single DNA molecules. *Am J Phys*. 2015;83(5).
46. Lerner E, Barth A, Hendrix J, Ambrose B, Birkedal V, Blanchard SC, et al. FRET-based dynamic structural biology: Challenges, perspectives and an appeal for open-science practices. Vol. 10, *eLife*. 2021.
47. Al Balushi AA, Gordon R. A label-free untethered approach to single-molecule protein binding kinetics. *Nano Lett*. 2014;14(10).
48. Guan J, Jia C, Li Y, Liu Z, Wang J, Yang Z, et al. Direct single-molecule dynamic detection of chemical reactions. *Sci Adv*. 2018;4(2).
49. Zhou X, Chieng A, Wang S. Label-Free Optical Imaging of Nanoscale Single Entities. *ACS Sens* [Internet]. 2024 Feb 12; Available from: <https://pubs.acs.org/doi/10.1021/acssensors.3c02526>
50. Yu D, Humar M, Meserve K, Bailey RC, Chormaic SN, Vollmer F. Whispering-gallery-mode sensors for biological and physical sensing. Vol. 1, *Nature Reviews Methods Primers*. 2021.
51. Juan ML, Righini M, Quidant R. Plasmon nano-optical tweezers. Vol. 5, *Nature Photonics*. 2011.
52. Taylor RW, Sandoghdar V. Interferometric Scattering (iSCAT) Microscopy and Related Techniques. In 2019.
53. Asor R, Kukura P. Characterising biomolecular interactions and dynamics with mass photometry. Vol. 68, *Current Opinion in Chemical Biology*. 2022.
54. Yousefi A, Ying C, Parmenter CDJ, Assadipapari M, Sanderson G, Zheng Z, et al. Optical Monitoring of In Situ Iron Loading into Single, Native Ferritin Proteins. *Nano Lett* [Internet]. 2023;23(8):3251–8. Available from: <https://doi.org/10.1021/acs.nanolett.3c00042>
55. Yousefi A, Zheng Z, Zargarbashi S, Assadipapari M, Hickman GJ, Parmenter CDJ, et al. Structural Flexibility and Disassembly Kinetics of Single Ferritin Molecules Using Optical Nanotweezers. *ACS Nano* [Internet]. 2024 Jun 8; Available from: <https://pubs.acs.org/doi/10.1021/acsnano.4c01221>
56. Pang Y, Gordon R. Optical Trapping of a Single Protein. *Nano Lett* [Internet]. 2012;12(1):402–6. Available from: <https://pubs.acs.org/doi/10.1021/nl203719v>

References

57. Ashkin A. Acceleration and Trapping of Particles by Radiation Pressure. *Phys Rev Lett.* 1970;24(4).
58. Ashkin A, Dziedzic JM, Chu S. Observation of a single-beam gradient-force optical trap for dielectric particles in air. *Opt Lett.* 1986;22(11).
59. Ashkin A, Dziedzic JM. Optical levitation by radiation pressure. *Appl Phys Lett.* 1971;19(8).
60. Raab EL, Prentiss M, Cable A, Chu S, Pritchard DE. Trapping of Neutral Sodium Atoms with Radiation Pressure. *Phys Rev Lett.* 1987;59(23).
61. Chu S, Bjorkholm JE, Ashkin A, Cable A. Experimental observation of optically trapped atoms. *Phys Rev Lett.* 1986;57(3).
62. Chu S, Hollberg L, Bjorkholm JE, Cable A, Ashkin A. Three-dimensional viscous confinement and cooling of atoms by resonance radiation pressure. *Phys Rev Lett.* 1985;55(1).
63. Ashkin A, Dziedzic JM. Optical trapping and manipulation of viruses and bacteria. *Science* (1979). 1987;235(4795).
64. Ashkin A, Dziedzic JM. Internal cell manipulation using infrared laser traps. *Proc Natl Acad Sci U S A.* 1989;86(20).
65. Li X, Zheng H, Yuen CH, Du J, Chen J, Lin Z, et al. Quantitative study of conservative gradient force and non-conservative scattering force exerted on a spherical particle in optical tweezers. *Opt Express.* 2021;29(16).
66. Baxter C, Loudon R. Radiation pressure and the photon momentum in dielectrics. Vol. 57, *Journal of Modern Optics.* 2010.
67. Song S, Wang N, Lu W, Lin Z. Optical force on a large sphere illuminated by Bessel beams: comparisons between ray optics method and generalized Lorenz–Mie theory. *Journal of the Optical Society of America A.* 2014;31(10).
68. Ashkin A. Optical trapping and manipulation of neutral particles using lasers. *Proc Natl Acad Sci U S A.* 1997;94(10).
69. Grigorenko AN, Roberts NW, Dickinson MR, Zhang Y. Nanometric optical tweezers based on nanostructured substrates. *Nat Photonics* [Internet]. 2008;2(6):365–70. Available from: <https://www.nature.com/articles/nphoton.2008.78>
70. Brenner H. Dynamics of a particle in a viscous fluid. *Chem Eng Sci.* 1962;17(6).
71. Bradac C. Nanoscale Optical Trapping: A Review. Vol. 6, *Advanced Optical Materials.* 2018.

References

72. Kotsifaki DG, Chormaic SN. Plasmonic optical tweezers based on nanostructures: fundamentals, advances and prospects. *Nanophotonics*. 2019;8(7):1227–45.
73. Quidant R. Plasmonic tweezers-The strength of surface plasmons. *MRS Bull*. 2012;37(8).
74. Shoji T, Tsuboi Y. Plasmonic optical tweezers toward molecular manipulation: Tailoring plasmonic nanostructure, light source, and resonant trapping. *Journal of Physical Chemistry Letters*. 2014;5(17).
75. Zhang Y, Min C, Dou X, Wang X, Urbach HP, Somekh MG, et al. Plasmonic tweezers: for nanoscale optical trapping and beyond. Vol. 10, *Light: Science and Applications*. 2021.
76. Coyle S, Netti MC, Baumberg JJ, Ghanem MA, Birkin PR, Bartlett PN, et al. Confined plasmons in metallic nanocavities. *Phys Rev Lett*. 2001;87(17).
77. Wu J, Gan X. Optimization of plasmonic nanostructure for nanoparticle trapping. *Opt Express*. 2012;20(14).
78. Tanaka Y, Kaneda S, Sasaki K. Nanostructured potential of optical trapping using a plasmonic nanoblock pair. *Nano Lett*. 2013;13(5).
79. Jones S, Andrén D, Karpinski P, Käll M. Photothermal Heating of Plasmonic Nanoantennas: Influence on Trapped Particle Dynamics and Colloid Distribution. *ACS Photonics*. 2018;5(7).
80. Chen KY, Lee AT, Hung CC, Huang JS, Yang YT. Transport and trapping in two-dimensional nanoscale plasmonic optical lattice. *Nano Lett*. 2013;13(9).
81. Gordon R. Metal Nanoapertures and Single Emitters. Vol. 8, *Advanced Optical Materials*. 2020.
82. Pang Y, Gordon R. Optical trapping of 12 nm dielectric spheres using double-nanoholes in a gold film. *Nano Lett*. 2011;11(9):3763–7.
83. Sergides M, Truong VG, Chormaic SN. Highly tunable plasmonic nanoring arrays for nanoparticle manipulation and detection. *Nanotechnology*. 2016;27(36).
84. Yoon SJ, Lee J, Han S, Kim CK, Ahn CW, Kim MK, et al. Non-fluorescent nanoscopic monitoring of a single trapped nanoparticle via nonlinear point sources. *Nat Commun*. 2018;9(1).
85. Baffou G, Girard C, Quidant R. Mapping Heat Origin in Plasmonic Structures. *Phys Rev Lett* [Internet]. 2010;104(13):136805. Available from: <https://link.aps.org/doi/10.1103/PhysRevLett.104.136805>

References

86. Gutiérrez Y, Ortiz D, Saiz JM, González F, Albella P, Moreno F. The quest for low loss high refractive index dielectric materials for UV photonic applications. *Applied Sciences (Switzerland)*. 2018;8(11).
87. Harrison PM. The structure and function of ferritin. *Biochem Educ*. 1986;14(4).
88. Lv C, Zhao G, Lönnnerdal B. Bioavailability of iron from plant and animal ferritins. *J Nutr Biochem* [Internet]. 2015;26(5):532–40. Available from: <https://linkinghub.elsevier.com/retrieve/pii/S0955286315000224>
89. Arosio P, Elia L, Poli M. Ferritin, cellular iron storage and regulation. *IUBMB Life* [Internet]. 2017;69(6):414–22. Available from: <https://onlinelibrary.wiley.com/doi/10.1002/iub.1621>
90. Bradley JM, Le Brun NE, Moore GR. Ferritins: furnishing proteins with iron. *JBIC Journal of Biological Inorganic Chemistry* [Internet]. 2016;21(1):13–28. Available from: <http://link.springer.com/10.1007/s00775-016-1336-0>
91. Pead S, Durrant E, Webb B, Larsen C, Heaton D, Johnson J, et al. Metal ion binding to apo, holo, and reconstituted horse spleen ferritin. *J Inorg Biochem* [Internet]. 1995;59(1):15–27. Available from: <http://www.ncbi.nlm.nih.gov/pubmed/7782791>
92. Chasteen ND, Harrison PM. Mineralization in Ferritin: An Efficient Means of Iron Storage [Internet]. 1999. Available from: <http://www.idealibrary.com>
93. Takahashi T, Kuyucak S. Functional Properties of Threefold and Fourfold Channels in Ferritin Deduced from Electrostatic Calculations. Vol. 84, *Biophysical Journal*. 2003.
94. Srivastava AK, Reutovich AA, Hunter NJ, Arosio P, Bou-Abdallah F. Ferritin microheterogeneity, subunit composition, functional, and physiological implications. *Sci Rep*. 2023;13(1).
95. Tosha T, Ng HL, Bhattasali O, Alber T, Theil EC. Moving Metal Ions through Ferritin–Protein Nanocages from Three-Fold Pores to Catalytic Sites. *J Am Chem Soc* [Internet]. 2010;132(41):14562–9. Available from: <https://pubs.acs.org/doi/10.1021/ja105583d>
96. Palombarini F, Fabio E Di, Boffi A, Macone A, Bonamore A. Ferritin nanocages for protein delivery to tumor cells. Vol. 25, *Molecules*. 2020.
97. Khoshnejad M, Parhiz H, Shuvaev V V, Dmochowski IJ, Muzykantov VR. Ferritin-based drug delivery systems: Hybrid nanocarriers for vascular immunotargeting. *Journal of Controlled Release* [Internet]. 2018;282:13–24. Available from: <https://linkinghub.elsevier.com/retrieve/pii/S0168365918301196>

98. Song N, Zhang J, Zhai J, Hong J, Yuan C, Liang M. Ferritin: A Multifunctional Nanoplatfom for Biological Detection, Imaging Diagnosis, and Drug Delivery. *Acc Chem Res* [Internet]. 2021;54(17):3313–25. Available from: <https://pubs.acs.org/doi/10.1021/acs.accounts.1c00267>
99. Palombarini F, Masciarelli S, Incocciati A, Liccardo F, Di Fabio E, Iazzetti A, et al. Self-assembling ferritin-dendrimer nanoparticles for targeted delivery of nucleic acids to myeloid leukemia cells. *J Nanobiotechnology*. 2021;19(1).
100. Orrit M, Bernard J. Single pentacene molecules detected by fluorescence excitation in a p-terphenyl crystal. *Phys Rev Lett*. 1990;65(21).
101. Yoshikawa H, Masuhara H. Near-field fluorescence spectroscopy and photochemistry of organic mesoscopic materials. Vol. 1, *Journal of Photochemistry and Photobiology C: Photochemistry Reviews*. 2000.
102. Gupta A, Sankaran J, Wohland T. Fluorescence correlation spectroscopy: The technique and its applications in soft matter. Vol. 4, *Physical Sciences Reviews*. 2019.
103. Regmi R, Berthelot J, Winkler PM, Mivelle M, Proust J, Bedu F, et al. All-Dielectric Silicon Nanogap Antennas to Enhance the Fluorescence of Single Molecules. *Nano Lett*. 2016;16(8).
104. Choi J, Grosely R, Puglisi E V., Puglisi JD. Expanding single-molecule fluorescence spectroscopy to capture complexity in biology. Vol. 58, *Current Opinion in Structural Biology*. 2019.
105. Chamorro-Garcia A, Merkoçi A. Nanobiosensors in diagnostics. *Nanobiomedicine (Rij)*. 2016;3.
106. Sasmal DK, Pulido LE, Kasal S, Huang J. Single-molecule fluorescence resonance energy transfer in molecular biology. Vol. 8, *Nanoscale*. 2016.
107. Deniz AA, Laurence TA, Beligere GS, Dahan M, Martin AB, Chemla DS, et al. Single-molecule protein folding: Diffusion fluorescence resonance energy transfer studies of the denaturation of chymotrypsin inhibitor 2. *Proc Natl Acad Sci U S A*. 2000;97(10).
108. Kretschy N, Sack M, Somoza MM. Sequence-Dependent Fluorescence of Cy3- And Cy5-Labeled Double-Stranded DNA. *Bioconjug Chem*. 2016;27(3).
109. Baibakov M, Patra S, Claude JB, Wenger J. Long-Range Single-Molecule Förster Resonance Energy Transfer between Alexa Dyes in Zero-Mode Waveguides. *ACS Omega*. 2020;5(12).
110. Heilemann M, Van De Linde S, Mukherjee A, Sauer M. Super-resolution imaging with small organic fluorophores. *Angewandte Chemie - International Edition*. 2009;48(37).

-
111. Roy R, Hohng S, Ha T. A practical guide to single-molecule FRET. Vol. 5, Nature Methods. 2008.
 112. Holden SJ, Uphoff S, Hohlbein J, Yadin D, Le Reste L, Britton OJ, et al. Defining the limits of single-molecule FRET resolution in TIRF microscopy. *Biophys J*. 2010;99(9).
 113. Israels B, Lund LM, Birkedal V. Single-Molecule FRET: Principles and Analysis. In 2022.
 114. Kim JY, Kim C, Lee NK. Real-time submillisecond single-molecule FRET dynamics of freely diffusing molecules with liposome tethering. *Nat Commun*. 2015;6.
 115. Nguyen TD, Chen YI, Chen LH, Yeh HC. Recent Advances in Single-Molecule Tracking and Imaging Techniques. Vol. 16, Annual Review of Analytical Chemistry. 2023.
 116. Hoffmann A, Nettels D, Clark J, Borgia A, Radford SE, Clarke J, et al. Quantifying heterogeneity and conformational dynamics from single molecule FRET of diffusing molecules: Recurrence analysis of single particles (RASP). *Physical Chemistry Chemical Physics*. 2011;13(5).
 117. Gopich I V., Szabo A. Decoding the pattern of photon colors in single-molecule FRET. *Journal of Physical Chemistry B*. 2009;113(31).
 118. Kalinin S, Felekyan S, Valeri A, Seidel CAM. Characterizing multiple molecular states in single-molecule multiparameter fluorescence detection by probability distribution analysis. *Journal of Physical Chemistry B*. 2008;112(28).
 119. Holmstrom ED, Holla A, Zheng W, Nettels D, Best RB, Schuler B. Accurate Transfer Efficiencies, Distance Distributions, and Ensembles of Unfolded and Intrinsically Disordered Proteins From Single-Molecule FRET. In: *Methods in Enzymology*. 2018.
 120. Haran G. Single-molecule fluorescence spectroscopy of biomolecular folding. Vol. 15, *Journal of Physics Condensed Matter*. 2003.
 121. Wang Y, Liu Y, DeBerg HA, Nomura T, Hoffman MT, Rohde PR, et al. Single molecule FRET reveals pore size and opening mechanism of a mechano-sensitive ion channel. *Elife*. 2014;3.
 122. Dustin ML, Depoil D. New insights into the T cell synapse from single molecule techniques. Vol. 11, *Nature Reviews Immunology*. 2011.
 123. Sako Y, Minoghchi S, Yanagida T. Single-molecule imaging of EGFR signalling on the surface of living cells. *Nat Cell Biol*. 2000;2(3).

124. Farooq S, Fijen C, Hohlbein J. Studying DNA-protein interactions with single-molecule Förster resonance energy transfer. Vol. 251, *Protoplasma*. 2014.
125. Israels B, Lund LM, Birkedal V. Single-Molecule FRET: Principles and Analysis. In 2022.
126. Martinelli AHS, Lopes FC, John EBO, Carlini CR, Ligabue-Braun R. Modulation of disordered proteins with a focus on neurodegenerative diseases and other pathologies. Vol. 20, *International Journal of Molecular Sciences*. 2019.
127. Krainer G, Keller S, Schlierf M. Structural dynamics of membrane-protein folding from single-molecule FRET. Vol. 58, *Current Opinion in Structural Biology*. 2019.
128. Leblanc SJ, Kulkarni P, Weninger KR. Single molecule FRET: A powerful tool to study intrinsically disordered proteins. Vol. 8, *Biomolecules*. 2018.
129. Van Der Lee R, Buljan M, Lang B, Weatheritt RJ, Daughdrill GW, Dunker AK, et al. Classification of intrinsically disordered regions and proteins. Vol. 114, *Chemical Reviews*. 2014.
130. Wen J, Hong L, Krainer G, Yao QQ, Knowles TPJ, Wu S, et al. Conformational Expansion of Tau in Condensates Promotes Irreversible Aggregation. *J Am Chem Soc*. 2021;143(33).
131. Wickramasinghe SP, Rhoades E. Measuring interactions between tau and aggregation inducers with single-molecule Förster resonance energy transfer. In: *Methods in Molecular Biology*. 2020.
132. Mollica L, Bessa LM, Hanouille X, Jensen MR, Blackledge M, Schneider R. Binding mechanisms of intrinsically disordered proteins: Theory, simulation, and experiment. Vol. 3, *Frontiers in Molecular Biosciences*. 2016.
133. Šponer J, Krepl M, Banáš P, Kührová P, Zgarbová M, Jurečka P, et al. How to understand atomistic molecular dynamics simulations of RNA and protein–RNA complexes? Vol. 8, *Wiley Interdisciplinary Reviews: RNA*. 2017.
134. Heesink G, Marseille MJ, Fakhree MAA, Driver MD, van Leijenhorst-Groener KA, Onck PR, et al. Exploring Intra- and Inter-Regional Interactions in the IDP α -Synuclein Using smFRET and MD Simulations. *Biomacromolecules*. 2023;24(8).
135. Vafabakhsh R, Levitz J, Isacoff EY. Conformational dynamics of a class C G-protein-coupled receptor. *Nature*. 2015;524(7566).
136. Wallin E, Von Heijne G. Genome-wide analysis of integral membrane proteins from eubacterial, archaean, and eukaryotic organisms. *Protein Science*. 1998;7(4).

-
137. Alberts B, Johnson A, Lewis J, Morgan D, Raff M, Roberts K, et al. *Molecular Biology of the Cell*. Molecular Biology of the Cell. 2017.
 138. Hilger D. The role of structural dynamics in GPCR-mediated signaling. Vol. 288, *FEBS Journal*. 2021.
 139. Bartels K, Lasitza-Male T, Hofmann H, Löw C. Single-Molecule FRET of Membrane Transport Proteins. Vol. 22, *ChemBioChem*. 2021.
 140. Wang L, Johnson ZL, Wasserman MR, Levring J, Chen J, Liu S. Characterization of the kinetic cycle of an ABC transporter by single-molecule and cryo-EM analyses. *Elife*. 2020;9.
 141. Vermeer B, Schmid S. Can DyeCycling break the photobleaching limit in single-molecule FRET? *Nano Res*. 2022;15(11).
 142. Chen BC, Legant WR, Wang K, Shao L, Milkie DE, Davidson MW, et al. Lattice light-sheet microscopy: Imaging molecules to embryos at high spatiotemporal resolution. *Science* (1979). 2014;346(6208).
 143. Banterle N, Lemke EA. Nanoscale devices for linkerless long-term single-molecule observation. Vol. 39, *Current Opinion in Biotechnology*. 2016.
 144. Smekal A. Zur Quantentheorie der Dispersion. *Naturwissenschaften*. 1923;11(43).
 145. Raman C V. A change of wave-length in light scattering [8]. Vol. 121, *Nature*. 1928.
 146. Heuke S, Rigneault H. Coherent Stokes Raman scattering microscopy (CSRS). *Nat Commun*. 2023;14(1).
 147. Guimarães AVA, Santos MF, Jorio A, Monken CH. Stokes-anti-Stokes light-scattering process: A photon-wave-function approach. *Phys Rev A (Coll Park)*. 2020;102(3).
 148. Müller M, Zumbusch A. Coherent anti-Stokes Raman scattering microscopy. Vol. 8, *ChemPhysChem*. 2007.
 149. Abalde-Cela S, Aldeanueva-Potel P, Mateo-Mateo C, Rodríguez-Lorenzo L, Alvarez-Puebla RA, Liz-Marzán LM. Surface-enhanced Raman scattering biomedical applications of plasmonic colloidal particles. Vol. 7, *Journal of the Royal Society Interface*. 2010.
 150. Alvarez-Puebla RA, Liz-Marzán LM. SERS-based diagnosis and biodetection. *Small*. 2010;6(5).
 151. Orlando A, Franceschini F, Muscas C, Pidkova S, Bartoli M, Rovere M, et al. A comprehensive review on Raman spectroscopy applications. Vol. 9, *Chemosensors*. 2021.

References

152. Langer J, de Aberasturi DJ, Aizpurua J, Alvarez-Puebla RA, Auguie B, Baumberg JJ, et al. Present and future of surface-enhanced Raman scattering. Vol. 14, ACS Nano. 2020.
153. Jones RR, Hooper DC, Zhang L, Wolverson D, Valev VK. Raman Techniques: Fundamentals and Frontiers. Vol. 14, Nanoscale Research Letters. 2019.
154. Rodriguez V, Couzi M, Adamietz F, Dussauze M, Guery G, Cardinal T, et al. Hyper-Raman and Raman scattering in paratellurite TeO₂. Journal of Raman Spectroscopy. 2013;44(5).
155. Day JPR, Domke KF, Rago G, Kano H, Hamaguchi HO, Vartiainen EM, et al. Quantitative coherent anti-stokes raman scattering (CARS) microscopy. Journal of Physical Chemistry B. 2011;115(24).
156. Chase B. Fourier transform Raman spectroscopy. Mikrochim Acta. 1987;93(1–6).
157. Moura CC, Tare RS, Oreffo ROC, Mahajan S. Raman spectroscopy and coherent anti-Stokes Raman scattering imaging: Prospective tools for monitoring skeletal cells and skeletal regeneration. Vol. 13, Journal of the Royal Society Interface. 2016.
158. Pérez-Jiménez AI, Lyu D, Lu Z, Liu G, Ren B. Surface-enhanced Raman spectroscopy: Benefits, trade-offs and future developments. Vol. 11, Chemical Science. 2020.
159. Siddhanta S, Narayana C. Surface enhanced Raman spectroscopy of proteins: Implications for drug designing. Nanomaterials and Nanotechnology. 2012;2(1).
160. Kumar N, Mignuzzi S, Su W, Roy D. Tip-enhanced Raman spectroscopy: principles and applications. EPJ Tech Instrum. 2015;2(1).
161. Kneipp K, Wang Y, Kneipp H, Perelman LT, Itzkan I, Dasari RR, et al. Single molecule detection using surface-enhanced raman scattering (SERS). Phys Rev Lett. 1997;78(9).
162. Nie S, Emory SR. Probing single molecules and single nanoparticles by surface-enhanced Raman scattering. Science (1979). 1997;275(5303).
163. Habuchi S, Cotlet M, Gronheid R, Dirix G, Michiels J, Vanderleyden J, et al. Single-molecule surface enhanced resonance Raman spectroscopy of the enhanced green fluorescent protein. J Am Chem Soc. 2003;125(28).
164. Xu H, Bjerneld EJ, Käll M, Börjesson L. Spectroscopy of single hemoglobin molecules by surface enhanced raman scattering. Phys Rev Lett. 1999;83(21).
165. Almeahadi LM, Curley SM, Tokranova NA, Tenenbaum SA, Lednev IK. Surface Enhanced Raman Spectroscopy for Single Molecule Protein Detection. Sci Rep. 2019;9(1).

166. Schuknecht F, Kołataj K, Steinberger M, Liedl T, Lohmueller T. Accessible hotspots for single-protein SERS in DNA-origami assembled gold nanorod dimers with tip-to-tip alignment. *Nat Commun.* 2023;14(1).
167. Qiu Y, Kuang C, Liu X, Tang L. Single-Molecule Surface-Enhanced Raman Spectroscopy. *Sensors* [Internet]. 2022;22(13):4889. Available from: <https://www.mdpi.com/1424-8220/22/13/4889>
168. Kumar S, Gahlaut SK, Singh JP. Sculptured thin films: Overcoming the limitations of surface-enhanced Raman scattering substrates. Vol. 12, *Applied Surface Science Advances*. 2022.
169. Michon J, Benzaouia M, Yao W, Miller OD, Johnson SG. Limits to surface-enhanced Raman scattering near arbitrary-shape scatterers. *Opt Express.* 2019;27(24).
170. Toscano G, Raza S, Xiao S, Wubs M, Jauho AP, Bozhevolnyi SI, et al. Surface-enhanced Raman spectroscopy: nonlocal limitations. *Opt Lett.* 2012;37(13).
171. Li L, Cao X, Zhang T, Wu Q, Xiang P, Shen C, et al. Recent Developments in Surface-Enhanced Raman Spectroscopy and Its Application in Food Analysis: Alcoholic Beverages as an Example. Vol. 11, *Foods*. 2022.
172. Stöckle RM, Suh YD, Deckert V, Zenobi R. Nanoscale chemical analysis by tip-enhanced Raman spectroscopy. *Chem Phys Lett.* 2000;318(1–3).
173. Zhang W, Yeo BS, Schmid T, Zenobi R. Single molecule tip-enhanced Raman spectroscopy with silver tips. *Journal of Physical Chemistry C.* 2007;111(4).
174. Yeo BS, Mädler S, Schmid T, Zhang W, Zenobi R. Tip-enhanced Raman spectroscopy can see more: The case of cytochrome c. *Journal of Physical Chemistry C.* 2008;112(13).
175. Helbing C, Deckert-Gaudig T, Firkowska-Boden I, Wei G, Deckert V, Jandt KD. Protein Handshake on the Nanoscale: How Albumin and Hemoglobin Self-Assemble into Nanohybrid Fibers. *ACS Nano.* 2018;12(2).
176. Wood BR, Asghari-Khiavi M, Bailo E, McNaughton D, Deckert V. Detection of nano-oxidation sites on the surface of hemoglobin crystals using tip-enhanced Raman scattering. *Nano Lett.* 2012;12(3).
177. Andrecka J, Takagi Y, Mickolajczyk KJ, Lippert LG, Sellers JR, Hancock WO, et al. Interferometric Scattering Microscopy for the Study of Molecular Motors. In: *Methods in Enzymology*. 2016.
178. Taylor RW, Sandoghdar V. Interferometric Scattering Microscopy: Seeing Single Nanoparticles and Molecules via Rayleigh Scattering. *Nano Lett* [Internet]. 2019;19(8):4827–35. Available from: <https://pubs.acs.org/doi/10.1021/acs.nanolett.9b01822>

179. Amos LA, Amos WB. The bending of sliding microtubules imaged by confocal light microscopy and negative stain electron microscopy. In: *Journal of Cell Science*. 1991.
180. Kukura P, Ewers H, Müller C, Renn A, Helenius A, Sandoghdar V. High-speed nanoscopic tracking of the position and orientation of a single virus. *Nat Methods*. 2009;6(12).
181. Vala M, Bujak Ł, García Marín A, Holanová K, Henrichs V, Braun M, et al. Nanoscopic Structural Fluctuations of Disassembling Microtubules Revealed by Label-Free Super-Resolution Microscopy. *Small Methods*. 2021;5(4).
182. De Wit G, Danial JSH, Kukura P, Wallace MI. Dynamic label-free imaging of lipid nanodomains. *Proc Natl Acad Sci U S A*. 2015;112(40).
183. Penwell SB, Ginsberg LDS, Noriega R, Ginsberg NS. Resolving ultrafast exciton migration in organic solids at the nanoscale. *Nat Mater*. 2017;16(11).
184. Taylor RW, Mahmoodabadi RG, Rauschenberger V, Giessl A, Schambony A, Sandoghdar V. Interferometric scattering microscopy reveals microsecond nanoscopic protein motion on a live cell membrane. *Nat Photonics*. 2019;13(7).
185. Piliarik M, Sandoghdar V. Direct optical sensing of single unlabelled proteins and super-resolution imaging of their binding sites. *Nat Commun*. 2014;5.
186. Cole D, Young G, Weigel A, Sebesta A, Kukura P. Label-Free Single-Molecule Imaging with Numerical-Aperture-Shaped Interferometric Scattering Microscopy. *ACS Photonics*. 2017;4(2).
187. Ortega Arroyo J, Andrecka J, Spillane KM, Billington N, Takagi Y, Sellers JR, et al. Label-free, all-optical detection, imaging, and tracking of a single protein. *Nano Lett*. 2014;14(4).
188. Dahmardeh M, Mirzaalian Dastjerdi H, Mazal H, Köstler H, Sandoghdar V. Self-supervised machine learning pushes the sensitivity limit in label-free detection of single proteins below 10 kDa. *Nat Methods*. 2023;20(3).
189. Young G, Hundt N, Cole D, Fineberg A, Andrecka J, Tyler A, et al. Quantitative mass imaging of single biological macromolecules. *Science (1979)*. 2018;360(6387).
190. Wu D, Hwang P, Li T, Piszczek G. Rapid characterization of adeno-associated virus (AAV) gene therapy vectors by mass photometry. *Gene Ther*. 2022;29(12).
191. Young G, Hundt N, Cole D, Fineberg A, Andrecka J, Tyler A, et al. Quantitative mass imaging of single molecules. *Science (1979)*. 2018;360(6387).
192. Wu D, Piszczek G. Measuring the affinity of protein-protein interactions on a single-molecule level by mass photometry. *Anal Biochem*. 2020;592.

193. Kofinova Z, Karunanithy G, Ferreira AS, Struwe WB. Measuring Protein-Protein Interactions and Quantifying Their Dissociation Constants with Mass Photometry. *Curr Protoc.* 2024;4(1).
194. Foley EDB, Kushwah MS, Young G, Kukura P. Mass photometry enables label-free tracking and mass measurement of single proteins on lipid bilayers. *Nat Methods.* 2021;18(10).
195. Kushwah MS, Foley EDB, Asor R, Kukura P. Understanding dynamin polymerization by single-molecule counting and particle-tracking using mass photometry. *Biophys J.* 2022;121(3).
196. Soltermann F, Foley EDB, Pagnoni V, Galpin M, Benesch JLP, Kukura P, et al. Quantifying Protein-Protein Interactions by Molecular Counting with Mass Photometry. *Angewandte Chemie - International Edition.* 2020;59(27).
197. Lusvarghi S, Lohith K, Morin-Leisk J, Ghirlando R, Hinshaw JE, Bewley CA. Binding Site Geometry and Subdomain Valency Control Effects of Neutralizing Lectins on HIV-1 Viral Particles. *ACS Infect Dis.* 2016;2(11).
198. Liebthal M, Kushwah MS, Kukura P, Dietz KJ. Single molecule mass photometry reveals the dynamic oligomerization of human and plant peroxiredoxins. *iScience.* 2021;24(11).
199. Paul SS, Lyons A, Kirchner R, Woodside MT. Quantifying Oligomer Populations in Real Time during Protein Aggregation Using Single-Molecule Mass Photometry. *ACS Nano.* 2022;16(10).
200. Wu D, Piszczek G. Standard protocol for mass photometry experiments. *European Biophysics Journal.* 2021;50(3–4).
201. Li Y, Struwe WB, Kukura P. Single molecule mass photometry of nucleic acids. *Nucleic Acids Res.* 2020;48(17).
202. Ashkin A, Dziedzic JM, Bjorkholm JE, Chu S. Observation of a single-beam gradient force optical trap for dielectric particles. In: *Optical Angular Momentum.* 2016.
203. Ashkin A. Acceleration and Trapping of Particles by Radiation Pressure. *Phys Rev Lett.* 1970;24(4).
204. Grimm R, Weidemüller M, Ovchinnikov YB. Optical Dipole Traps for Neutral Atoms. *Advances in Atomic, Molecular and Optical Physics.* 2000;42(C).
205. Cooper A, Covey JP, Madjarov IS, Porsev SG, Safronova MS, Endres M. Alkaline-Earth Atoms in Optical Tweezers. *Phys Rev X.* 2018;8(4).
206. Chen A, Jing Y, Sang FN, Li SW, Xu JH. Determination of the interaction mechanism of 10 μm oil-in-water emulsion droplets using optical tweezers. *Chem Eng Sci.* 2018;181.

-
207. Chen A, Li SW, Jing D, Xu JH. Interactions between colliding oil drops coated with non-ionic surfactant determined using optical tweezers. *Chem Eng Sci.* 2019;193.
 208. Bennink ML, Schärer OD, Kanaar R, Sakata-Sogawa K, Schins JM, Kanger JS, et al. Single-molecule manipulation of double-stranded DNA using optical tweezers: Interaction studies of DNA with RecA and YOYO-1. *Cytometry.* 1999;36(3).
 209. Zhuang X. Unraveling DNA condensation with optical tweezers. Vol. 305, *Science.* 2004.
 210. Maruyama H, Kotani K, Masuda T, Honda A, Takahata T, Arai F. Nanomanipulation of single influenza virus using dielectrophoretic concentration and optical tweezers for single virus infection to a specific cell on a microfluidic chip. *Microfluid Nanofluidics.* 2011;10(5).
 211. Pang Y, Song H, Kim JH, Hou X, Cheng W. Optical trapping of individual human immunodeficiency viruses in culture fluid reveals heterogeneity with single-molecule resolution. *Nat Nanotechnol.* 2014;9(8).
 212. Min TL, Mears PJ, Chubiz LM, Rao C V., Golding I, Chemla YR. High-resolution, long-term characterization of bacterial motility using optical tweezers. *Nat Methods.* 2009;6(11).
 213. Dao M, Lim CT, Suresh S. Mechanics of the human red blood cell deformed by optical tweezers. In: *Journal of the Mechanics and Physics of Solids.* 2003.
 214. Keloth A, Anderson O, Risbridger D, Paterson L. Single cell isolation using optical tweezers. *Micromachines (Basel).* 2018;9(9).
 215. Rivera M, Mjaavatten A, Smith SB, Baez M, Wilson CAM. Temperature dependent mechanical unfolding and refolding of a protein studied by thermo-regulated optical tweezers. *Biophys J.* 2023;122(3).
 216. Stangner T, Wagner C, Singer D, Angioletti-Uberti S, Gutsche C, Dzubiella J, et al. Determining the specificity of monoclonal antibody hpt-101 to tau-peptides with optical tweezers. *ACS Nano.* 2013;7(12).
 217. Bechtluft P, Van Leeuwen RGH, Tyreman M, Tomkiewicz D, Nouwen N, Tepper HL, et al. Direct observation of chaperone-induced changes in a protein folding pathway. *Science (1979).* 2007;318(5855).
 218. Cecconi C, Shank EA, Dahlquist FW, Marqusee S, Bustamante C. Protein-DNA chimeras for single molecule mechanical folding studies with the optical tweezers. *European Biophysics Journal.* 2008;37(6).

-
219. Cecconi G, Shank EA, Bustamante C, Marqusee S. Biochemistry: Direct observation of the three-state folding of a single protein molecule. *Science* (1979). 2005;309(5743).
 220. Shank EA, Cecconi C, Dill JW, Marqusee S, Bustamante C. The folding cooperativity of a protein is controlled by its chain topology. *Nature*. 2010;465(7298).
 221. Crozier KB. Quo vadis, plasmonic optical tweezers? *Light Sci Appl*. 2019;8(1).
 222. Mora M, Stannard A, Garcia-Manyes S. The nanomechanics of individual proteins. Vol. 49, *Chemical Society Reviews*. 2020.
 223. Frustaci S, Vollmer F. Whispering-gallery mode (WGM) sensors: review of established and WGM-based techniques to study protein conformational dynamics. Vol. 51, *Current Opinion in Chemical Biology*. 2019.
 224. Gorodetsky ML, Savchenkov AA, Ilchenko VS. Ultimate Q of optical microsphere resonators. In: *Proceedings of SPIE - The International Society for Optical Engineering*. 1996.
 225. Kim E, Baaske MD, Vollmer F. Towards next-generation label-free biosensors: recent advances in whispering gallery mode sensors. Vol. 17, *Lab on a Chip*. 2017.
 226. Chao CY, Guo LJ. Biochemical sensors based on polymer microrings with sharp asymmetrical resonance. *Appl Phys Lett*. 2003;83(8).
 227. Tamboli AC, Haberer ED, Sharma R, Lee KH, Nakamura S, Hu EL. Room-temperature continuous-wave lasing in GaNInGaN microdisks. *Nat Photonics*. 2007;1(1).
 228. Garrett CGB, Kaiser W, Bond WL. Stimulated emission into optical whispering modes of spheres. *Physical Review*. 1961;124(6).
 229. Duong Ta V, Chen R, Ma L, Jun Ying Y, Dong Sun H. Whispering gallery mode microlasers and refractive index sensing based on single polymer fiber. *Laser Photon Rev*. 2013;7(1).
 230. Zhang X, Liu L, Xu L. Ultralow sensing limit in optofluidic micro-bottle resonator biosensor by self-referenced differential-mode detection scheme. *Appl Phys Lett*. 2014;104(3).
 231. Berneschi S, Farnesi D, Cosi F, Conti GN, Pelli S, Righini GC, et al. High Q silica microbubble resonators fabricated by arc discharge. *Opt Lett*. 2011;36(17).
 232. Armani D, Min B, Martin A, Vahala KJ. Electrical thermo-optic tuning of ultrahigh-Q microtoroid resonators. *Appl Phys Lett*. 2004;85(22).

-
233. Xavier J, Vincent S, Meder F, Vollmer F. Advances in optoplasmonic sensors - Combining optical nano/microcavities and photonic crystals with plasmonic nanostructures and nanoparticles. Vol. 7, Nanophotonics. 2018.
234. Santiago-Cordoba MA, Boriskina S V., Vollmer F, Demirel MC. Nanoparticle-based protein detection by optical shift of a resonant microcavity. *Appl Phys Lett*. 2011;99(7).
235. Santiago-Cordoba MA, Cetinkaya M, Boriskina S V., Vollmer F, Demirel MC. Ultrasensitive detection of a protein by optical trapping in a photonic-plasmonic microcavity. *J Biophotonics*. 2012;5(8–9).
236. Swaim JD, Knittel J, Bowen WP. Detection limits in whispering gallery biosensors with plasmonic enhancement. *Appl Phys Lett*. 2011;99(24).
237. Vollmer F, Arnold S. Whispering-gallery-mode biosensing: Label-free detection down to single molecules. *Nat Methods*. 2008;5(7).
238. Baaske MD, Foreman MR, Vollmer F. Single-molecule nucleic acid interactions monitored on a label-free microcavity biosensor platform. *Nat Nanotechnol*. 2014;9(11).
239. Vollmer F, Braun D, Libchaber A, Khoshshima M, Teraoka I, Arnold S. Protein detection by optical shift of a resonant microcavity. *Appl Phys Lett*. 2002;80(21).
240. Houghton MC, Kashanian SV, Derrien TL, Masuda K, Vollmer F. Whispering-Gallery Mode Optoplasmonic Microcavities: From Advanced Single-Molecule Sensors and Microlasers to Applications in Synthetic Biology. Vol. 11, *ACS Photonics*. 2024.
241. Toropov NA, Houghton MC, Yu D, Vollmer F. Thermo-optoplasmonic single-molecule sensing on optical microcavities. *bioRxiv*. 2023;2012–23.
242. Kim E, Baaske MD, Schuldes I, Wilsch PS, Vollmer F. Label-free optical detection of single enzyme-reactant reactions and associated conformational changes. *Sci Adv*. 2017;3(3).
243. Swaim JD, Knittel J, Bowen WP. Detection of nanoparticles with a frequency locked whispering gallery mode microresonator. *Appl Phys Lett*. 2013;102(18).
244. Matsko AB, Ilchenko VS. Optical resonators with whispering-gallery modes - Part I: Basics. *IEEE Journal on Selected Topics in Quantum Electronics*. 2006;12(1).
245. Guler U, Turan R. Effect of particle properties and light polarization on the plasmonic resonances in metallic nanoparticles. *Opt Express*. 2010;18(16).

-
246. Rahmani M, Miroshnichenko AE, Lei DY, Luk'Yanchuk B, Tribelsky MI, Kuznetsov AI, et al. Beyond the hybridization effects in plasmonic nanoclusters: Diffraction-induced enhanced absorption and scattering. *Small*. 2014;10(3).
 247. Sun Q, Yu H, Ueno K, Zu S, Matsuo Y, Misawa H. Revealing the plasmon coupling in gold nanochains directly from the near field. *Opto-Electronic Advances*. 2019;2(4).
 248. Zhang H, Govorov AO. Optical generation of hot plasmonic carriers in metal nanocrystals: The effects of shape and field enhancement. *Journal of Physical Chemistry C*. 2014;118(14).
 249. Novotny L, Bian RX, Xie XS. Theory of nanometric optical tweezers. *Phys Rev Lett*. 1997;79(4).
 250. Quidant R, Girard C. Surface-plasmon-based optical manipulation. Vol. 2, *Laser and Photonics Reviews*. 2008.
 251. Okamoto K, Kawata S. Radiation force exerted on subwavelength particles near a nanoaperture. *Phys Rev Lett*. 1999;83(22).
 252. Maragò OM, Jones PH, Gucciardi PG, Volpe G, Ferrari AC. Optical trapping and manipulation of nanostructures. Vol. 8, *Nature Nanotechnology*. 2013.
 253. Al Balushi AA, Kotnala A, Wheaton S, Gelfand RM, Rajashekara Y, Gordon R. Label-free free-solution nanoaperture optical tweezers for single molecule protein studies. Vol. 140, *Analyst*. Royal Society of Chemistry; 2015. p. 4760–78.
 254. Novotny L, Hecht B. *Principles of nano-optics*. Cambridge university press; 2012.
 255. Neumeier L, Quidant R, Chang DE. Self-induced back-action optical trapping in nanophotonic systems. *New J Phys*. 2015;17(12).
 256. Bethe HA. Theory of diffraction by small holes. *Physical Review*. 1944;66(7–8).
 257. Juan ML, Gordon R, Pang Y, Eftekhari F, Quidant R. Self-induced back-action optical trapping of dielectric nanoparticles. *Nat Phys* [Internet]. 2009;5(12):915–9. Available from: <http://www.nature.com/articles/nphys1422>
 258. Kwak ES, Onuta TD, Amarie D, Potyrailo R, Stein B, Jacobson SC, et al. Optical trapping with integrated near-field apertures. *Journal of Physical Chemistry B*. 2004;108(36).
 259. Saleh AAE, Dionne JA. Toward efficient optical trapping of Sub-10-nm particles with coaxial plasmonic apertures. *Nano Lett*. 2012;12(11).

-
260. Yoo D, Gurunatha KL, Choi HK, Mohr DA, Ertsgaard CT, Gordon R, et al. Low-Power Optical Trapping of Nanoparticles and Proteins with Resonant Coaxial Nanoaperture Using 10 nm Gap. *Nano Lett.* 2018;18(6).
261. Jensen RA, Huang IC, Chen O, Choy JT, Bischof TS, Lončar M, et al. Optical Trapping and Two-Photon Excitation of Colloidal Quantum Dots Using Bowtie Apertures. *ACS Photonics.* 2016;3(3).
262. Kotsifaki DG, Truong VG, Chormaic SN. Fano-resonant, asymmetric, metamaterial-assisted tweezers for single nanoparticle trapping. *Nano Lett.* 2020;20(5).
263. Chen C, Juan ML, Li Y, Maes G, Borghs G, Van Dorpe P, et al. Enhanced optical trapping and arrangement of nano-objects in a plasmonic nanocavity. *Nano Lett.* 2012;12(1).
264. Pang Y, Gordon R. Optical Trapping of 12 nm Dielectric Spheres Using Double-Nanoholes in a Gold Film. *Nano Lett* [Internet]. 2011;11(9):3763–7. Available from: <https://pubs.acs.org/doi/10.1021/nl201807z>
265. Al Balushi AA, Gordon R. Label-Free Free-Solution Single-Molecule Protein–Small Molecule Interaction Observed by Double-Nanohole Plasmonic Trapping. *ACS Photonics* [Internet]. 2014;1(5):389–93. Available from: <https://pubs.acs.org/doi/10.1021/ph5000314>
266. Hacoheh N, Ip CJX, Gordon R. Analysis of Egg White Protein Composition with Double Nanohole Optical Tweezers. *ACS Omega* [Internet]. 2018;3(5):5266–72. Available from: <https://pubs.acs.org/doi/10.1021/acsomega.8b00651>
267. Regmi R, Al Balushi AA, Rigneault H, Gordon R, Wenger J. Nanoscale volume confinement and fluorescence enhancement with double nanohole aperture. *Sci Rep.* 2015;5.
268. Ying C, Karakaçi E, Bermúdez-Ureña E, Ianiro A, Foster C, Awasthi S, et al. Watching Single Unmodified Enzymes at Work [Internet]. Available from: arXiv preprint arXiv:2107.06407.
269. Al Balushi AA, Zehtabi-Oskuie A, Gordon R. Observing single protein binding by optical transmission through a double nanohole aperture in a metal film. *Biomed Opt Express.* 2013;4(9).
270. Kochuveedu ST, Kim DH. Surface plasmon resonance mediated photoluminescence properties of nanostructured multicomponent fluorophore systems. Vol. 6, *Nanoscale.* 2014.
271. Anger P, Bharadwaj P, Novotny L. Enhancement and quenching of single-molecule fluorescence. *Phys Rev Lett.* 2006;96(11).

-
272. Kühn S, Håkanson U, Rogobete L, Sandoghdar V. Enhancement of single-molecule fluorescence using a gold nanoparticle as an optical nanoantenna. *Phys Rev Lett*. 2006;97(1).
273. Kinkhabwala A, Yu Z, Fan S, Avlasevich Y, Müllen K, Moerner WE. Large single-molecule fluorescence enhancements produced by a bowtie nanoantenna. *Nat Photonics*. 2009;3(11).
274. Aouani H, Mahboub O, Bonod N, Devaux E, Popov E, Rigneault H, et al. Bright unidirectional fluorescence emission of molecules in a nanoaperture with plasmonic corrugations. *Nano Lett*. 2011;11(2).
275. Ureña EB, Kreuzer MP, Itzhakov S, Rigneault H, Quidant R, Oron D, et al. Excitation enhancement of a quantum dot coupled to a plasmonic antenna. *Advanced Materials*. 2012;24(44).
276. Liu Y, Yang Y, Wang G, Wang D, Shao PL, Tang J, et al. Multiplexed discrimination of SARS-CoV-2 variants via plasmonic-enhanced fluorescence in a portable and automated device. *Nat Biomed Eng*. 2023;7(12).
277. Punj D, Mivelle M, Moparthi SB, Van Zanten TS, Rigneault H, Van Hulst NF, et al. A plasmonic “antenna-in-box” platform for enhanced single-molecule analysis at micromolar concentrations. *Nat Nanotechnol*. 2013;8(7).
278. Belkin M, Chao SH, Jonsson MP, Dekker C, Aksimentiev A. Plasmonic Nanopores for Trapping, Controlling Displacement, and Sequencing of DNA. *ACS Nano*. 2015;9(11).
279. Baranov DG, Zuev DA, Lepeshov SI, Kotov O V, Krasnok AE, Evlyukhin AB, et al. All-dielectric nanophotonics: the quest for better materials and fabrication techniques. *Optica* [Internet]. 2017;4(7):814–25. Available from: <http://opg.optica.org/optica/abstract.cfm?URI=optica-4-7-814>
280. Zhou J, Zhou PL, Shen Q, Ahmed SA, Pan XT, Liu HL, et al. Probing Multidimensional Structural Information of Single Molecules Transporting through a Sub-10 nm Conical Plasmonic Nanopore by SERS. *Anal Chem*. 2021;93(34).
281. Shibayama N. Allosteric transitions in hemoglobin revisited. *Biochim Biophys Acta Gen Subj*. 2020;1864(2).
282. Biswas A, Bayer IS, Biris AS, Wang T, Dervishi E, Faupel F. Advances in top-down and bottom-up surface nanofabrication: Techniques, applications & future prospects. Vol. 170, *Advances in Colloid and Interface Science*. 2012.
283. Yousefi A, Seyyed Ebrahimi SA, Seyfoori A, Mahmoodzadeh Hosseini H. Maghemite Nanorods and Nanospheres: Synthesis and Comparative Physical and Biological Properties. *Bionanoscience*. 2018;8(1).

References

284. Tseng AA, Chen K, Chen CD, Ma KJ. Electron beam lithography in nanoscale fabrication: Recent development. *IEEE Transactions on Electronics Packaging Manufacturing*. 2003;26(2).
285. Kant K, Losic D. Focused Ion Beam (FIB) Technology for Micro- and Nanoscale Fabrications. In 2013.
286. Taguchi A, Nakayama A, Oketani R, Kawata S, Fujita K. Multiphoton-Excited Deep-Ultraviolet Photolithography for 3D Nanofabrication. *ACS Appl Nano Mater*. 2020;3(11).
287. Zhou W, Min G, Zhang J, Liu Y, Wang J, Zhang Y, et al. Nanoimprint lithography: A processing technique for nanofabrication advancement. *Nanomicro Lett*. 2011;3(2).
288. Peng F, Su Y, Zhong Y, Fan C, Lee ST, He Y. Silicon nanomaterials platform for bioimaging, biosensing, and cancer therapy. *Acc Chem Res*. 2014;47(2).
289. Ryabchikov Y V. Unique applications of optical properties of silicon nanostructures. *MM Science Journal*. 2019;2019(December).
290. Bandaru PR, Pichanusakorn P. An outline of the synthesis and properties of silicon nanowires. Vol. 25, *Semiconductor Science and Technology*. 2010.
291. Kunii Y, Tabe M, Kajiyama K. Solid-Phase Epitaxy of CVD Amorphous Si Film on Crystalline Si. *Jpn J Appl Phys*. 1982;21(10).
292. Huff M. Recent advances in reactive ion etching and applications of high-aspect-ratio microfabrication. *Micromachines (Basel)*. 2021;12(8).
293. Juhasz R, Elfström N, Linnros J. Controlled fabrication of silicon nanowires by electron beam lithography and electrochemical size reduction. *Nano Lett*. 2005;5(2).
294. Hegedüs N, Balázs K, Balázs C. Silicon nitride and hydrogenated silicon nitride thin films: A review of fabrication methods and applications. Vol. 14, *Materials*. 2021.
295. Daineka D, Bulkin P, Girard G, Bourée JE, Drévillon B. High density plasma enhanced chemical vapor deposition of optical thin films. *EPJ Applied Physics*. 2004;26(1).
296. Theeten JB, Aspnes DE. Ellipsometry in Thin Film Analysis. *Annual Review of Materials Science*. 1981;11(1).
297. Carr DW, Tiberio RC. Direct-write electron beam lithography: history and state of the art. *Materials Research Society Symposium - Proceedings*. 2000;584.

-
298. Cakirlar C, Galderisi G, Beyer C, Simon M, Mikolajick T, Trommer J. Challenges in Electron Beam Lithography of Silicon Nanostructures. In: Proceedings of the IEEE Conference on Nanotechnology. 2022.
 299. Martinez-Chapa SO, Salazar A, Madou MJ. Chapter 13.2 - Two-Photon Polymerization as a Component of Desktop Integrated Manufacturing Platforms A2 - Baldacchini, Tommaso BT - Three-Dimensional Microfabrication Using Two-photon Polymerization. In: Micro and Nano Technologies. 2016.
 300. Ephrath LM. Reactive Ion Etching for VLSI. IEEE Trans Electron Devices. 1981;28(11).
 301. Rangelow IW. Critical tasks in high aspect ratio silicon dry etching for microelectromechanical systems. Journal of Vacuum Science & Technology A: Vacuum, Surfaces, and Films. 2003;21(4).
 302. Racka-Szmidt K, Stonio B, Żelazko J, Filipiak M, Sochacki M. A review: Inductively coupled plasma reactive ion etching of silicon carbide. Vol. 15, Materials. 2022.
 303. Steglich M, Käsebier T, Zilk M, Pertsch T, Kley EB, Tünnermann A. The structural and optical properties of black silicon by inductively coupled plasma reactive ion etching. J Appl Phys. 2014;116(17).
 304. Giannuzzi LA, Stevie FA. Introduction to focused ion beams: Instrumentation, theory, techniques and practice. Introduction to Focused Ion Beams: Instrumentation, Theory, Techniques and Practice. 2005.
 305. Höflich K, Hobler G, Allen FI, Wirtz T, Rius G, McElwee-White L, et al. Roadmap for focused ion beam technologies. Vol. 10, Applied Physics Reviews. 2023.
 306. Ghorbanzadeh M, Jones S, Moravvej-Farshi MK, Gordon R. Improvement of Sensing and Trapping Efficiency of Double Nanohole Apertures via Enhancing the Wedge Plasmon Polariton Modes with Tapered Cusps. ACS Photonics [Internet]. 2017;4(5):1108–13. Available from: <https://pubs.acs.org/doi/10.1021/acsphotonics.6b00923>
 307. Boparai HK, Comfort SD, Shea PJ, Szecsody JE. Remediating explosive-contaminated groundwater by in situ redox manipulation (ISRM) of aquifer sediments. Chemosphere [Internet]. 2008;71(5):933–41. Available from: <https://linkinghub.elsevier.com/retrieve/pii/S0045653507013689>
 308. Kotnala A, Depaoli D, Gordon R. Sensing nanoparticles using a double nanohole optical trap. Lab Chip. 2013 Oct 21;13(20):4142–6.

References

309. Ying C, Karakaçi E, Bermúdez-Ureña E, Ianiro A, Foster C, Awasthi S, et al. Watching Single Unmodified Enzymes at Work [Internet]. [cited 2022 Dec 28]. Available from: arXiv preprint arXiv:2107.06407.
310. Eggenberger OM, Ying C, Mayer M. Surface coatings for solid-state nanopores. Vol. 11, *Nanoscale*. 2019.
311. Ding H, Zhang D, Chu S, Zhou J, Su X. Screening and structural and functional investigation of a novel ferritin from *Phascolosoma esculenta*. *Protein Science*. 2017 Oct 1;26(10):2039–50.
312. Peng Y, Chang X, Lang M. Iron homeostasis disorder and alzheimer’s disease. Vol. 22, *International Journal of Molecular Sciences*. MDPI; 2021.
313. Theil EC, Takagi H, Small GW, He L, Tipton AR, Danger D. The ferritin iron entry and exit problem. *Inorganica Chim Acta*. 2000 Jan 1;297(1–2):242–51.
314. Theil EC, Liu XS, Tosha T. Gated pores in the ferritin protein nanocage. Vol. 361, *Inorganica Chimica Acta*. Elsevier S.A.; 2008. p. 868–74.
315. Lv C, Zhao G, Lönnerdal B. Bioavailability of iron from plant and animal ferritins. *Journal of Nutritional Biochemistry*. 2015 May 1;26(5):532–40.
316. Huan H, Jiang Q, Wu Y, Qiu X, Lu C, Su C, et al. Structure determination of ferritin from *Dendrorhynchus zhejiangensis*. *Biochem Biophys Res Commun*. 2020 Oct 15;531(2):195–202.
317. Vymazal J, Brooks RA, Bulte JWM, Gordon D, Aisen P. Iron uptake by ferritin: NMR relaxometry studies at low iron loads.
318. Pozzi C, di Pisa F, Lalli D, Rosa C, Theil E, Turano P, et al. Time-lapse anomalous X-ray diffraction shows how Fe²⁺ substrate ions move through ferritin protein nanocages to oxidoreductase sites. *Acta Crystallogr D Biol Crystallogr* [Internet]. 2015 Apr 1;71(4):941–53. Available from: <https://scripts.iucr.org/cgi-bin/paper?S1399004715002333>
319. Koralewski M, Balejíčková L, Mitróová Z, Pochylski M, Baranowski M, Kopčanský P. Morphology and Magnetic Structure of the Ferritin Core during Iron Loading and Release by Magneto-optical and NMR Methods. *ACS Appl Mater Interfaces* [Internet]. 2018 Mar 7;10(9):7777–87. Available from: <https://pubs.acs.org/doi/10.1021/acsami.7b18304>
320. Chua-anusorn W, Webb J. Infrared spectroscopic studies of nanoscale iron oxide deposits isolated from human thalassemic tissues. *J Inorg Biochem* [Internet]. 2000 Apr;79(1–4):303–9. Available from: <https://linkinghub.elsevier.com/retrieve/pii/S0162013499002330>
321. Tosha T, Ng HL, Bhattasali O, Alber T, Theil EC. Moving Metal Ions through Ferritin–Protein Nanocages from Three-Fold Pores to Catalytic Sites. *J Am*

- Chem Soc [Internet]. 2010 Oct 20;132(41):14562–9. Available from: <https://pubs.acs.org/doi/10.1021/ja105583d>
322. Behera RK, Theil EC. Moving Fe²⁺ from ferritin ion channels to catalytic OH centers depends on conserved protein cage carboxylates. Available from: www.pnas.org/lookup/suppl/doi:10.1073/
323. Yin YD, Chen FF, Hu J, Yang L, Song XT, Wu GR, et al. Solid-State Nanopore Distinguishes Ferritin and Apo-Ferritin with Identical Exteriors through Amplified Flexibility at Single-Molecule Level. *Anal Chem*. 2023 Nov 14;95(45):16496–504.
324. Maity B, Li Z, Niwase K, Ganser C, Furuta T, Uchihashi T, et al. Single-molecule level dynamic observation of disassembly of the apo-ferritin cage in solution. *Physical Chemistry Chemical Physics*. 2020;22(33).
325. Kumagai S, Yoshii S, Yamada K, Matsukawa N, Fujiwara I, Iwahori K, et al. Electrostatic placement of single ferritin molecules. *Appl Phys Lett*. 2006;88(15).
326. Houben L, Weissman H, Wolf SG, Rybchinski B. A mechanism of ferritin crystallization revealed by cryo-STEM tomography. *Nature* [Internet]. 2020 Mar 26;579(7800):540–3. Available from: <http://www.nature.com/articles/s41586-020-2104-4>
327. Narayanan S, Shahbazian-Yassar R, Shokuhfar T. In Situ Visualization of Ferritin Biomineralization via Graphene Liquid Cell-Transmission Electron Microscopy. 2020; Available from: <https://dx.doi.org/10.1021/acsbiomaterials.9b01889>
328. Axford DN, Davis JJ. Electron flux through apo-and holoferritin. *Nanotechnology*. 2007 Apr 11;18(14).
329. Mandal SS. Force Spectroscopy on Single Molecules of Life. *ACS Omega* [Internet]. 2020 May 26;5(20):11271–8. Available from: <https://pubs.acs.org/doi/10.1021/acsomega.0c00814>
330. Chasteen ND, Harrison PM. Mineralization in Ferritin: An Efficient Means of Iron Storage [Internet]. 1999. Available from: <http://www.idealibrary.com>
331. Takahashi T, Kuyucak S. Functional Properties of Threefold and Fourfold Channels in Ferritin Deduced from Electrostatic Calculations. Vol. 84, *Biophysical Journal*. 2003.
332. Kruchinin NY, Kucherenko MG. Molecular Dynamics Simulation of Electrically Induced Conformational Changes of Polyampholytic Polypeptides on Gold Nanoparticle Surface. *Colloid Journal*. 2019;81(2):110–9.

References

333. Juan ML, Gordon R, Pang Y, Eftekhari F, Quidant R. Self-induced back-action optical trapping of dielectric nanoparticles. *Nat Phys*. 2009;5(12):915–9.
334. Pang Y, Gordon R. Optical trapping of a single protein. *Nano Lett*. 2012 Jan 11;12(1):402–6.
335. Cai Y, Deng T, Pan Y, Zink JJ. Use of Ferritin Capped Mesoporous Silica Nanoparticles for Redox and pH Triggered Drug Release In Vitro and In Vivo. *Adv Funct Mater*. 2020 Sep 1;30(39).
336. Song N, Zhang J, Zhai J, Hong J, Yuan C, Liang M. Ferritin: A Multifunctional Nanoplatfrom for Biological Detection, Imaging Diagnosis, and Drug Delivery. *Acc Chem Res*. 2021 Sep 7;54(17):3313–25.
337. Khoshnejad M, Parhiz H, Shuvaev V v., Dmochowski IJ, Muzykantov VR. Ferritin-based drug delivery systems: Hybrid nanocarriers for vascular immunotargeting. *Journal of Controlled Release*. 2018 Jul 28;282:13–24.
338. Inoue I, Chiba M, Ito K, Okamatsu Y, Suga Y, Kitahara Y, et al. One-step construction of ferritin encapsulation drugs for cancer chemotherapy. *Nanoscale*. 2021 Jan 21;13(3):1875–83.
339. Zehtabi-Oskuie A, Bergeron JG, Gordon R. Flow-dependent double-nanohole optical trapping of 20 nm polystyrene nanospheres. *Sci Rep*. 2012;2.
340. Pang Y, Gordon R. Optical trapping of 12 nm dielectric spheres using double-nanoholes in a gold film. *Nano Lett*. 2011 Sep 14;11(9):3763–7.
341. Gomes CM, Faísca PFN. SPRINGER BRIEFS IN MOLECULAR SCIENCE PROTEIN FOLDING AND STRUCTURE Protein Folding An Introduction [Internet]. Available from: <http://www.springer.com/series/11958>
342. Bello M, Valderrama B, Serrano-Posada H, Rudiño-Piñera E. Molecular dynamics of a thermostable multicopper oxidase from *Thermus thermophilus* HB27: Structural differences between the apo and holo forms. *PLoS One*. 2012 Jul 10;7(7).
343. Drude P. Zur Elektronentheorie der Metalle. *Ann Phys* [Internet]. 1900;306(3):566–613. Available from: <https://onlinelibrary.wiley.com/doi/10.1002/andp.19003060312>
344. Pan YH, Sader K, Powell JJ, Bleloch A, Gass M, Trinick J, et al. 3D morphology of the human hepatic ferritin mineral core: New evidence for a subunit structure revealed by single particle analysis of HAADF-STEM images. *J Struct Biol*. 2009 Apr;166(1):22–31.
345. Jian N, Dowle M, Horniblow RD, Tselepis C, Palmer RE. Morphology of the ferritin iron core by aberration corrected scanning transmission electron microscopy. *Nanotechnology*. 2016 Oct 13;27(46).

-
346. Bohren CF, Huffman DR. Absorption and scattering of light by small particles. Wiley; 1983. 530 p.
347. Booth LS, Browne E v., Mauranyapin NP, Madsen LS, Barfoot S, Mark A, et al. Modelling of the dynamic polarizability of macromolecules for single-molecule optical biosensing. *Sci Rep.* 2022 Dec 1;12(1).
348. Guler U, Turan R. Effect of particle properties and light polarization on the plasmonic resonances in metallic nanoparticles. *Opt Express.* 2010;18(16).
349. Mestres P, Berthelot J, Acimovic SS, Quidant R. Unraveling the optomechanical nature of plasmonic trapping. *Light Sci Appl.* 2016 Jul 1;5(7).
350. Wheaton S, Gordon R. Molecular weight characterization of single globular proteins using optical nanotweezers. *Analyst.* 2015 Jul 21;140(14):4799–803.
351. Aier I, Varadwaj PK, Raj U. Structural insights into conformational stability of both wild-type and mutant EZH2 receptor. *Sci Rep.* 2016;6.
352. Li Q, Ying YL, Liu SC, Lin Y, Long YT. Detection of Single Proteins with a General Nanopore Sensor. *ACS Sens.* 2019;4(5).
353. Bradley JM, Pullin J, Moore GR, Svistunenko DA, Hemmings AM, le Brun NE. Dalton Transactions PAPER Routes of iron entry into, and exit from, the catalytic ferroxidase sites of the prokaryotic ferritin SynFtn †. *Dalton Transactions.* 2020;49.
354. Weeratunga SK, Lovell S, Yao H, Battaile KP, Fischer CJ, Gee CE, et al. Structural studies of bacterioferritin B from *Pseudomonas aeruginosa* suggest a gating mechanism for iron uptake via the ferroxidase center. *Biochemistry.* 2010 Feb 16;49(6):1160–75.
355. Bakker GR, Boyer RF. Iron incorporation into apoferritin. The role of apoferritin as a ferroxidase. *Journal of Biological Chemistry.* 1986;261(28):13182–5.
356. BONOMI F, PAGANI S. Uptake of iron by apoferritin from a ferric dihydrolipeate complex. *Eur J Biochem.* 1991;199(1):181–6.
357. Aier I, Varadwaj PK, Raj U. Structural insights into conformational stability of both wild-type and mutant EZH2 receptor. *Sci Rep.* 2016 Oct 7;6.
358. Proulx-Curry PM, Chasteen ND. COHDIHAfIOH CHEMISTRY REVIEWS Molecular aspects of iron uptake and storage in ferritin. Vol. 144, *Coordination Chemistry Reviews.* 1995.
359. Liu X, Theil EC. Ferritins: Dynamic management of biological iron and oxygen chemistry. *Acc Chem Res.* 2005;38(3).

-
360. Ferritin crystals in the gut caeca of *stegocephaloides christianiensis* boeck and other *stegocephalidae* (amphipoda *gammaridea*): a functional interpretation . *Philosophical Transactions of the Royal Society of London B, Biological Sciences*. 1984;306(1127).
361. Gonciarz RL, Collisson EA, Renslo AR. Ferrous Iron-Dependent Pharmacology. Vol. 42, *Trends in Pharmacological Sciences*. 2021.
362. Bresgen N, Eckl PM. Oxidative stress and the homeodynamics of iron metabolism. Vol. 5, *Biomolecules*. 2015.
363. Sana B, Johnson E, Lim S. The unique self-assembly/disassembly property of *Archaeoglobus fulgidus* ferritin and its implications on molecular release from the protein cage. *Biochim Biophys Acta Gen Subj*. 2015;1850(12).
364. Bridges KR, Hoffman KE. The effects of ascorbic acid on the intracellular metabolism of iron and ferritin. *Journal of Biological Chemistry*. 1986;261(30).
365. Brissot P, Deugnier Y, Le Trent A, Regnouard F, Simon M, Bourel M. Ascorbic acid status in idiopathic hemochromatosis. *Digestion*. 1978;17(6).
366. Zhang P, Omaye ST. β -Carotene and protein oxidation: Effects of ascorbic acid and α -tocopherol. *Toxicology*. 2000;146(1).
367. Kim M, Rho Y, Jin KS, Ahn B, Jung S, Kim H, et al. PH-dependent structures of ferritin and apoferritin in solution: Disassembly and reassembly. *Biomacromolecules*. 2011;12(5).
368. Valero E, Fiorini S, Tambalo S, Busquier H, Callejas-Fernández J, Marzola P, et al. In vivo long-term magnetic resonance imaging activity of ferritin-based magnetic nanoparticles versus a standard contrast agent. *J Med Chem*. 2014;57(13).
369. Fan K, Gao L, Yan X. Human ferritin for tumor detection and therapy. *Wiley Interdiscip Rev Nanomed Nanobiotechnol*. 2013;5(4).
370. Smith-Johannsen H, Drysdale JW. Reversible dissociation of ferritin and its subunits in vitro. *BBA - Protein Structure*. 1969;194(1).
371. Stefanini S, Vecchini P, Chiancone E. On the Mechanism of Horse Spleen Apoferritin Assembly: A Sedimentation Velocity and Circular Dichroism Study. *Biochemistry*. 1987;26(7).
372. Harrison PM, Gregory DW. Reassembly of apoferritin molecules from subunits. *Nature*. 1968;220(5167).
373. Benni I, Trabuco MC, Di Stasio E, Arcovito A, Boffi A, Malatesta F, et al. Excimer based fluorescent pyrene-ferritin conjugate for protein oligomerization studies and imaging in living cells. *RSC Adv*. 2018;8(23).

References

374. Platnich CM, Rizzuto FJ, Cosa G, Sleiman HF. Single-molecule methods in structural DNA nanotechnology. Vol. 49, *Chemical Society Reviews*. 2020.
375. Adcock SA, McCammon JA. Molecular dynamics: Survey of methods for simulating the activity of proteins. Vol. 106, *Chemical Reviews*. 2006.
376. Timoshnikov VA, Kobzeva T V., Polyakov NE, Kontoghiorghes GJ. Redox interactions of vitamin c and iron: Inhibition of the pro-oxidant activity by deferiprone. *Int J Mol Sci*. 2020;21(11).
377. Boyer RF, J. McCleary C. Superoxide ion as a primary reductant in ascorbate-mediated ferretin iron release. *Free Radic Biol Med*. 1987;3(6).
378. Badu-Boateng C, Naftalin RJ. Ascorbate and ferritin interactions: Consequences for iron release in vitro and in vivo and implications for inflammation. Vol. 133, *Free Radical Biology and Medicine*. 2019.
379. Jones T, Spencer R, Walsh C, Jone T, Spencer R, Walsh C. Mechanism and Kinetics of Iron Release from Ferritin by Dihydroflavins and Dihydroflavin Analogues†. *Biochemistry*. 1978;17(19).
380. Badu-Boateng C, Pardalaki S, Wolf C, Lajnef S, Peyrot F, Naftalin RJ. Labile iron potentiates ascorbate-dependent reduction and mobilization of ferritin iron. *Free Radic Biol Med*. 2017 Jul 1;108:94–109.
381. Takeda S, Yamaki M, Ebina S, Nagayama K. Site-specific reactivities of cysteine residues in horse L-apoferritin. *J Biochem*. 1995;117(2).
382. Yoshizawa K, Mishima Y, Park SY, Heddle JG, Tame JRH, Iwahori K, et al. Effect of N-terminal residues on the structural stability of recombinant horse L-chain apoferritin in an acidic environment. *J Biochem*. 2007;142(6).
383. Li Z, Maity B, Hishikawa Y, Ueno T, Lu D. Importance of the Subunit–Subunit Interface in Ferritin Disassembly: A Molecular Dynamics Study. *Langmuir* [Internet]. 2022;38(3):1106–13. Available from: <https://doi.org/10.1021/acs.langmuir.1c02753>
384. Watt GD, Frankel RB, Papaefthymiou GC. Reduction of mammalian ferritin. *Proc Natl Acad Sci U S A*. 1985;82(11).
385. Theil EC, Liu XS, Tosha T. Gated pores in the ferritin protein nanocage. *Inorganica Chim Acta* [Internet]. 2008;361(4):868–74. Available from: <https://linkinghub.elsevier.com/retrieve/pii/S0020169307005178>
386. Wheaton S, Gordon R. Molecular weight characterization of single globular proteins using optical nanotweezers. *Analyst* [Internet]. 2015;140(14):4799–803. Available from: <http://xlink.rsc.org/?DOI=C5AN00026B>
387. Quinten M. *Optical Properties of Nanoparticle Systems: Mie and beyond*. 2011.

-
388. Vedula LS, Brannigan G, Economou NJ, Xi J, Hall MA, Liu R, et al. A unitary anesthetic binding site at high resolution. *Journal of Biological Chemistry*. 2009;284(36).
389. Lawson DM, Artymiuk PJ, Yewdall SJ, Smith JMA, Livingstone JC, Treffry A, et al. Solving the structure of human H ferritin by genetically engineering intermolecular crystal contacts. *Nature*. 1991;349(6309).
390. Mohanty A, Mithra K, Jena SS, Behera RK. Kinetics of Ferritin Self-Assembly by Laser Light Scattering: Impact of Subunit Concentration, pH, and Ionic Strength. *Biomacromolecules*. 2021;22(4).
391. Sato D, Ohtomo H, Yamada Y, Hikima T, Kurobe A, Fujiwara K, et al. Ferritin Assembly Revisited: A Time-Resolved Small-Angle X-ray Scattering Study. *Biochemistry*. 2016;55(2).
392. Krausova K, Charousova M, Kratochvil Z, Takacsova P, Tesarova B, Sivak L, et al. Toward understanding the kinetics of disassembly of ferritins of varying origin and subunit composition. *Appl Mater Today*. 2022;28.
393. Hilser VJ, Dowdy D, Oas TG, Freire E. The structural distribution of cooperative interactions in proteins: Analysis of the native state ensemble. *Proceedings of the National Academy of Sciences [Internet]*. 1998 Aug 18;95(17):9903–8. Available from: <https://doi.org/10.1073/pnas.95.17.9903>
394. King NP, Sheffler W, Sawaya MR, Vollmar BS, Sumida JP, André I, et al. Computational design of self-assembling protein nanomaterials with atomic level accuracy. *Science (1979)*. 2012;336(6085).
395. Chen H, Zhang S, Xu C, Zhao G. Engineering protein interfaces yields ferritin disassembly and reassembly under benign experimental conditions. *Chemical Communications*. 2016;52(46).
396. Nirmalraj PN, Rossell MD, Dachraoui W, Thompson D, Mayer M. In Situ Observation of Chemically Induced Protein Denaturation at Solvated Interfaces. *ACS Appl Mater Interfaces*. 2023 Oct 18;
397. Thompson SA, Paterson S, Azab MMM, Wark AW, de la Rica R. Light-Triggered Inactivation of Enzymes with Photothermal Nanoheaters. *Small*. 2017;13(15).
398. Mahmoudi M, Lohse SE, Murphy CJ, Fathizadeh A, Montazeri A, Suslick KS. Variation of protein corona composition of gold nanoparticles following plasmonic heating. *Nano Lett*. 2014;14(1).
399. Yang Y, Zheng N, Zhao X, Yang J, Zhang Y, Han R, et al. Changes in bovine milk fat globule membrane proteins caused by heat procedures using a label-free proteomic approach. *Food Research International*. 2018;113.

-
400. Zhan W, Gao K, Zhu C, Song W. Optical trapping using all silicon nanoantennas with ultra-high electric field enhancement. *Appl Phys Lett*. 2020;117(24).
 401. Xu Z, Crozier KB. All-dielectric nanotweezers for trapping and observation of a single quantum dot. *Opt Express*. 2019;27(4).
 402. Brunetti G, Sasanelli N, Armenise MN, Ciminelli C. Nanoscale Optical Trapping by Means of Dielectric Bowtie. *Photonics*. 2022;9(6).
 403. Deng YH, Yang ZJ, He J. Plasmonic nanoantenna-dielectric nanocavity hybrids for ultrahigh local electric field enhancement. *Opt Express*. 2018;26(24).